DISSERTATION

PLASMA MODIFICATION OF METAL OXIDES AND TEXTILES: TAILORING SURFACE PROPERTIES FOR IMPROVED GAS SENSOR AND PROTECTIVE CLOTHING APPLICATIONS

Submitted by

Kimberly A. M. Hiyoto

Department of Chemistry

In partial fulfillment of the requirements

For the Degree of Doctor of Philosophy

Colorado State University

Fort Collins, Colorado

Fall 2021

Doctoral Committee:

Advisor: Ellen R. Fisher

Carmen S. Menoni
Anthony K. Rappe
Joseph C. von Fischer

ABSTRACT

PLASMA MODIFICATION OF METAL OXIDES AND TEXTILES: TAILORING SURFACE PROPERTIES FOR IMPROVED GAS SENSOR AND PROTECTIVE CLOTHING APPLICATIONS

This dissertation focuses on utilizing inductively coupled plasma processing to modify various materials for applications in gas sensing and protective clothing. By relating changes in the plasma gas-phase during treatment, resulting material characteristics, and application-based performance, insights into how these materials work can be gained. Ultimately, this knowledge allows for a targeted approach to optimizing the material's surface properties for a specific behavior.

The first part of this work concentrates on the plasma modification of semiconducting metal oxides (SMO) to create gas sensors that are more responsive to a target gas at lower operating temperatures. First, SnO_2 nanoparticles (NP) supported by a traditional substrate (ZrO_2 wafer) were treated with a CO or CO_2 plasma as a function of applied plasma power (P). X-ray photoelectron spectroscopy (XPS) analysis of the NP after plasma exposure demonstrates that the CO plasma deposits an amorphous carbon film, whereas the CO_2 plasma results in the etching of the SnO_2 lattice. Optical emission spectroscopy (OES) studies were used to identify key excited-state species in the plasma gas-phase to explain the depositing and etching nature of these two systems. Gas sensing performance studies demonstrate that the deposition of a film on the SnO_2 blocked analyte-sensor interactions, resulting in a negative effect on the response of the

sensor. The CO_2 plasma treated sensors, however, displayed an increased response to benzene and CO at lower operating temperatures when compared to the untreated (UT) material.

The adaptation of the SnO_2 sensor and plasma treatments to becompatible with a paper-based sensor (PGS) provided positive indicators for future studies. Indeed, an Ar/O_2 plasma was used to treat SnO_2 NP PGS at $P = 15 – 60$ W. Similar to the CO_2 plasma, this system has also been shown to etch the SnO_2 lattice resulting in improved device performance. The PGS treated at 15 and 60 W showed an increased response to ethanol and CO at operating temperatures ≤50 °C. These studies indicate that the selectivity of the sensor can be tuned with plasma *P*. Additionally, these sensors showed some response and recovery behavior to ethanol, indicating that these devices are robust enough to be used multiple times. Preliminary work expanding the SMO used to make these PGS is also included to demonstrate the applicability of this device fabrication and plasma modification methods for other materials and SMO morphologies. These gas sensor studies highlight the importance of understanding the relationship between surface properties and device performance. By obtaining a better understanding of the gas detection process, a targeted approach to fabricating improved gas sensors can be established.

The final section of this work examines the effect of fabric hydrophobicity on NP attachment and resuspension. These studies employed C_3F_8 and $H_2O_{(v)}$ plasmas to treat four common lab coat materials. XPS and water contact angle goniometry confirm that the C_3F_8 plasma treatment increases the hydrophobicity of the fabrics and the $H_2O_{(v)}$ plasma increases the wettability of most materials. Hydrophobic recovery studies of the $H_2O_{(v)}$ treated samples suggest that there are minimal aging effects on the Tyvek® and 100% cotton fabrics, but further work is needed to optimize the plasma parameters for the 80/20 polyester/cotton and 100% polypropylene samples.

The attachment and release behavior of Al_2O_3 NP, carbon black, and carbon nanotubes with the UT and treated materials are also discussed. Ideally, personal protective clothing should either repel (preventing initial NP attachment and fabric contamination) or hold on to (limiting the potential for secondary exposure from contaminated clothes) NP. In general, it is thought that the tightness of the fabric weave is the only factor that influences NP attachment and resuspension. Scanning electron microscopy images of the contaminated and shaken fabrics reveal that the surface chemistry of the material cannot be excluded as the attachment and release of the nanomaterials differed between the C_3F_8, $H_2O_{(v)}$, and UT fabrics. Through these studies, fabric characteristics that influence the interaction with nanomaterials are explored and can be used to inform better safety recommendations when working with these materials.

ACKNOWLEDGMENTS

This time in graduate school would not have been as successful without the mentorship and support from many people. I would like to start by thanking Dr. Ellen Fisher for her encouragement and advice over the years. Through the many opportunities (both academic and social) that I have had the pleasure of experiencing as a part of this research group, I have learned to be a better scientist, communicator, and person who can appreciate the finer things in life. I would also like to thank past and present Fisher Group members. I am forever grateful for all of the training and helpful discussions. I am especially thankful for the feedback on presentations, abstracts, and manuscripts and for being there to bounce ideas or talk through problems with. In addition, thank you to all of the ARC team, shops, and admin for the assistance with both my research and the confusing world that is graduate school requirements and paperwork.

For the friends I have made at CSU, I will never forget the laughs, baking nights, pickling days, trips, knitting parties, and other random adventures. Since most of you have moved on to better and bigger things in life, I can confidently say Fort Collins is not the same place I have come to love living without all of you in it.

Finally, I would like to thank my friends and family. I know for a fact that I would not have made it through this program without all of you in my life. In particular, I would like to thank my parents and stepparents. Our FaceTime calls and the flat rate boxes full of things I miss from home make being so far away not feel as lonely. I am so grateful that all of you have shown me unlimited love and support and have helped me become the person I am today.

TABLE OF CONTENTS

ABSTRACT ii

ACKNOWLEDGMENTS v

LIST OF TABLES ix

LIST OF FIGURES x

CHAPTER 1. Introduction 1

1.1 Motivation and Background of Gas Sensor Studies 1

1.2 Plasma Processing and Need for Improved Fabrics for Protective Clothing 4

1.3 Overview of Research 7

REFERENCES 10

CHAPTER 2. Experimental Methods 12

2.1 Gas Sensor Fabrication 12

2.2 Fabric Preparation 15

2.3 Plasma Reactor and Treatments 15

2.4 Material and Plasma Characterization 17

2.5 Gas Sensor Performance Studies 20

2.6 ENP Attachment and Characterization 21

REFERENCES 23

CHAPTER 3. Comparison of CO and CO_2 rf Plasma Treatment of SnO_2 Nanoparticles for Gas Sensing Materials 24

3.1 Introduction 24

3.2 Results and Discussion 27

3.3 Summary 50

REFERENCES 52

CHAPTER 4. Utilizing Plasma Modified SnO_2 Paper Gas Sensors to Better Understand Gas-Surface Interactions at Low Temperatures 55

4.1 Introduction 55

4.2 Results and Discussion 58

4.3 Summary 78

REFERENCES 80

CHAPTER 5. Effects of Surface Hydrophobicity of Common Lab Coat Fabrics on Nanoparticle Attachment and Resuspension 82

5.1 Introduction 82

5.2 Results and Discussion 84

5.3 Summary 114

REFERENCES 116

CHAPTER 6. Exploration of Other Nano- and Micro-Sized Materials for Sensor and Energy Storage Applications 118

6.1. Introduction 118

6.2. Results and Discussion 123

6.3.Summary 143

REFERENCES 145

CHAPTER 7. Research Summary and Future Directions 147

7.1 Research Summary 147

7.2 Future Directions 150

REFERENCES 153

APPENDIX A. Independent Research Proposal 155

A.1 Overview, Research Summary..... 155

A.2 Background and Motivation 156

A.3 Project Description.....159

A.4 Proposed Work.....162

A.5 Potential Challenges..... 171

REFERENCES 173

LIST OF ABBREVIATIONS..... 175

LIST OF TABLES

3.1 Select relative species densities of CO and CO_2 plasma systems 33
3.2 XPS atomic composition and ratio of O binding environments 35

4.1 Elemental composition (percent C, Sn, and O) and ratio of lattice to adsorbed oxygen of UT and 60 W treated (new and aged) PGS 63

5.1 XPS atomic composition of the UT and plasma treated fabric samples 86
5.2 WCA for UT and FC plasma treated fabrics 93
5.3 WCA for fresh and aged $H_2O_{(v)}$ plasma treated fabrics 97
5.4 Raw counts of carbon black agglomerates on UT and plasma treated fabrics 103
5.5 Raw counts of Al_2O_3 agglomerates on UT and plasma treated fabrics 107
5.6 Total number of bundles and individual CNT on UT and plasma treated fabrics 109

LIST OF FIGURES

2.1 Photograph of scintillation vial used for SnO_2 TF growth on a paper substrate with printed electrodes 14
2.2 Schematic of plasma reactor showing samples placements and fabric holder 16

3.1 Full wavelength range of raw OES spectra of CO and CO_2 plasmas (p = 150 mTorr, P = 25 W) with and without SnO_2 NP 28
3.2 Select regions of raw OES spectra of the CO and CO_2 plasma systems (p = 150 mTorr, P = 25 W) 30
3.3 Calculated relative species densities as a function of P 31
3.4 High resolution XPS spectra of SnO_2 NP treated with a CO plasma at P = 25 & 100 W 34
3.5 Representative FT-IR spectra of KBr pellet before and after CO plasma exposure 37
3.6 Representative survey XPS spectra of CO plasma treated SnO_2 NP 38
3.7 High-resolution XPS spectra of SnO_2 NP treated with a CO_2 plasma at P = 25 – 75 W 41
3.8 High-resolution XPS spectra of 100 W CO_2 plasma treated SnO_2 NP 42
3.9 UT SnO_2 sensor response to ethanol, CO, and benzene and benzene response and recovery behavior 44
3.10 Representative raw resistance of CO_2 and CO treated SnO_2 sensors 46
3.11 Response to ethanol, CO, and benzene of CO_2 treated sensors 48
3.12 Response and recovery behavior of CO_2 treated to ethanol (T_S = 250 °C) 49

4.1 SEM and EDS elemental composition maps of UT SnO_2 PGS 59
4.2 SEM images of paper substrate, UT SnO_2 PGS, and SnO_2 PGS after 60 W Ar/O_2 plasma treatment 60
4.3 High-resolution XPS spectra of UT and 60 W plasma treated PGS 62
4.4 Representative raw OES spectra of Ar/O_2 plasma with and without PGS and calculated relative species densities 65
4.5 Temperature dependent response of UT SnO_2 sensor to EtOH, CO, and benzene 67
4.6 Temperature dependent response of Ar/O_2 plasma treated PGS sensors (P = 15 – 60 W, p = 140 mTorr) to EtOH, CO, and benzene 68
4.7 Response and recovery behavior of plasma treated PGS to benzene and CO at select T_S 70
4.8 Response and recovery behavior of UT traditional and plasma treated PGS to EtOH 71
4.9 Temperature dependent response of Ar/O_2 plasma treated PGS sensors (P = 60 W, p = 50 – 100 mTorr) to EtOH, CO, and benzene 75
4.10 Resistance in air of Ar/O_2 plasma treated PGS (P = 15 – 60 W, p = 140 mTorr) 76

5.1 High-resolution C_{1s} spectra of UT fabrics 87
5.2 High-resolution C_{1s} spectra of FC plasma treated fabrics (P = 50 W, p = 30 mTorr) 89
5.3 High-resolution C_{1s} spectra of FC plasma treated glass slide (P = 50 W, p = 30 mTorr) 90
5.4 High-resolution C_{1s} spectra of $H_2O_{(v)}$ plasma treated fabrics (P = 30 W, p = 15 mTorr) 92
5.5 SEM images and photographs of UT fabrics 95
5.6 SEM images of UT and plasma modified fabrics 99
5.7 Carbon black agglomerate counts on Tyvek® and cotton 101

5.8 Carbon black agglomerate counts on blend and PP 102
5.9 Al_2O_3 agglomerate counts on Tyvek® and cotton 105
5.10 Al_2O_3 agglomerate counts on blend and PP 106
5.11 Same spot SEM images of UT PP contaminated with ENP 111
5.12 Same spot SEM images of FC PP contaminated with carbon black and CNT 112
5.13 Number of carbon black and CNT agglomerates before and after shaking 113

6.1 Simplified schematic of possible SMO and MO/VGN constructs 120
6.2 SEM and EDS elemental composition maps of UT ZnO NP PGS 122
6.3 Temperature dependent response of UT ZnO NP sensors to EtOH and CO 124
6.4 Temperature dependent CO response of UT ZnO and Ar/O_2 plasma treated ZnO PGS 125
6.5 XRD pattern of SnO_2 TF grown on paper 127
6.6 Representative XPS survey and high-resolution spectra of SnO_2 TF grown on paper 128
6.7 Resistance in air of SnO_2 TF PGS 130
6.8 XRD pattern and SEM image of ZnO μrods grown on paper 132
6.9 Temperature dependent CO response of UT ZnO NP and μrod sensors 134
6.10 Photographs of VGN samples and Cu holders used during growth 136
6.11 SEM images of butter P50 samples (grown with smaller holder) 138
6.12 SEM images of UT coconut on Ni foam, coconut P50, and MO/coconut P50 samples 140
6.13 SEM images of upstream and downstream butter P50 samples 141

A.1 Conceptual framework of goals in the independent proposal 161
A.2 Schematic of proposed MO/VGN synthesis procedure 163
A.3 SEM images of VGN grown on Cu tape 164
A.4 Photographs of water drops interacting with the bare and coconut oil covered Ni foam 166
A.5 Representative CV of bare and coconut oil covered Ni foam 169

CHAPTER 1

INTRODUCTION

This chapter discusses the motivation and background of the work presented in this dissertation as an introductory chapter. Plasma modification of nanomaterials in the context of two applications is included to demonstrate the relationship between surface properties and material function/behavior. The first part of this chapter focuses on the use of plasma modification to improve the performance of semiconducting metal oxide (SMO) gas sensors compared to other, more commonly used methods. The second part discusses plasma functionalization and thin film deposition of fabrics as a route to improve protective clothing materials by limiting secondary exposure of nanomaterials. The chapter concludes with an overview of the research within the entire dissertation.

1.1 Motivation and Background of Gas Sensor Research

Monitoring of air quality is an ongoing effort, especially with concerns about global warming and health effects with long-term exposure to pollutants. Traditionally, this is done using permanent monitoring stations that track species like CO, O_3, NO_2, and volatile organic compounds.[1] To supplement these measurements, agencies and programs utilize citizen science projects to monitor areas where having permanent sites is not a feasible option. To successfully implement these initiatives, reliable, affordable, and portable gas sensors are needed.

A more detailed explanation of how SMO sensors detect gases is discussed in Chapters 3 and 4. Briefly, when SMO gas sensors are exposed to the atmosphere, O_2 will preferentially

adsorb onto oxygen vacancies on the SMO lattice.[2-5] The adsorbed oxygen can then extract electrons from the material in an oxidizing interaction, resulting in an increase in sensor resistance. Target gases can then interact with this layer and release electrons back into the material in a reducing interaction, and the resistance decreases. The reactivity of the oxygen layer depends on the speciation, which is controlled by the temperature of the material. From this sensing process, two challenges with using this type of material are apparent. In addition to increasing the power consumption of a device, a high operating temperature (T_S) will also decrease the lifetime of the sensors. Because these sensors detect gases through reducing or oxidizing interactions, cross sensitivity (or signal changes from interfering species) is often a concern with these types of materials.

The most common strategies to improve these qualities rely on doping or using a combination of SMO. Zhang *et al.* prepared Ce-doped SnO_2 sensors for enhanced 2-butanone detection.[6] Although all sensors (both the pure and doped SnO_2) had an optimal T_S of 175 °C, the doped samples had a 2.9 times increase in response to 20 ppm 2-butanone and a higher selectivity when tested against gases like acetone, toluene, and methanol. Another report looked at SnO_2-In_2O_3 nanocomposites and found the combination decreased the T_S from 160 to 140 °C and increased the response to 50 ppm n-butanol by ~ 2.2 times.[7] This sensor, however, also had a comparable response to ethanol, indicating further work improving the selectivity of this material is required. Although both strategies did improve aspects of sensor performance, changing in the bulk material can introduce new challenges. In some cases, the addition of dopants can cause crystal structure instability and lead to decomposition of the material at much lower temperatures than that of the undoped counterpart.[8] Doped or composite materials can

also increase the complexity and cost of synthesis and unpredictable synergistic effects obscure the sensing process, leading to a lack of understanding of how these materials work.

Low-temperature plasma (LTP) processing is a desirable method to modify SMO gas sensors as it can alter the surface of the material without changing bulk properties. Plasmas are partially ionized gases made of a variety of species (free electrons, ions, radicals, neutral species, etc.) in both ground and excited states. In general, plasmas can be used to etch, deposit a film, or functionalize the surface of the material.[9] This makes plasmas useful to modify materials for a variety of applications due to the large parameter space that allows for tunable treatments. For all of the work presented in this dissertation, a radio frequency inductively-coupled plasma was used, and treatments were performed as a function of either applied plasma power (P), precursor pressure (p), or precursor identity.

One of the earliest reports of plasma modification of SnO_2 gas sensors monitored their sensitivity to 100 ppm propanol as a function of exposure time to an O_2 plasma.[10] They found that the longest treatment time (15 minutes) resulted in sensors with the largest response to propanol at room temperature [whereas the untreated (UT) sensor had an optimal T_S at 300 °C]. The authors attribute this to a decrease in material resistance resulting from an increase in lattice O vacancies, and thus a change in the amount of adsorbed gas on the plasma treated sensors. Later studies support and expand upon this work by using alternate etching systems to create lattice vacancies to promote low T_S sensing.[11-14] Previous work in our lab demonstrated that using O_2/Ar and hydrogen containing plasma systems to treat SnO_2 nanoparticles (NP) and nanowires on a ZrO_2 wafer increased the response to CO and benzene at a lower T_S when compared to the UT sensors.[11, 15-16] The first part of this dissertation focuses on continuing these studies and demonstrating the complex nature of plasma-material interactions by using two

systems (CO and CO_2 plasmas) that have competing etching and film deposition processes and how these impact the gas sensing performance of SnO_2 NP. Later chapters apply these studies to adapting the traditional gas sensors (supported by a ZrO_2 wafer and $T_S \leq 300$ °C) to a paper-based device with several SMO where $T_S \leq 100$ °C.

Using plasmas also allows for characterization of the plasma gas-phase during the modification process. In particular, optical emission spectroscopy (OES) is a powerful diagnostic tool as it can be used to measure species densities and plasma energetics and kinetics without perturbing the system.[9] By comparing the plasma with and without the presence of a substrate, changes in the gas-phase can be correlated to changes in the material to better understand the modification process and the effect of plasma exposure on the substrate. This, coupled with gas sensing studies, can help elucidate the relationship between the material surface chemistry and improved sensor performance. Ultimately, this knowledge can help to select and design effective sensors that can be used reliably in applications like monitoring air quality using citizen science projects.

1.2 Plasma Processing and the Need for Improved Fabrics for Protective Clothing

In addition to gas sensors, nanomaterials are also commonly used in fields such as health care, energy storage, and catalysis.[17-18] For people using or making these materials, personal protective equipment (PPE) is required to prevent exposure and resulting adverse health effects. Although there are general guidelines[19] from the National Institute for Occupational Safety and Health for handling these materials, little work has been done to study the potential for contaminated PPE to cause secondary exposure. Previous studies found that 3 – 10 μm silica attachment and release from fabrics was only dependent on weave pattern and not chemical

composition.[20-21] Because of the types of fabrics used, however, a direct comparison between all of the materials is difficult, so the impact of fabric composition cannot be disregarded. Further details of these studies and their limitations are discussed later in Chapter 5.

Similar to the sensor projects, LTP modification can alter the surface of the fabrics while maintaining bulk structure and properties. This allows for the effect of surface composition to be isolated from the weave pattern and a better understanding of the interaction between the nanomaterial and fabrics can be achieved. In addition to the previously discussed benefits, LTP are ideal for the modification of polymers and other soft materials when compared to thermal plasmas due to their nonequilibrium properties.[9, 22] The high energy electrons in the plasma are able to dissociate and ionize the precursor to form reactive radicals and ions with the gas temperature typically as low as ~300 K.[9] Also, using plasmas allows for the deposition of a conformal coating on structurally complex substrates that cannot uniformly and easily be achieved with traditional wet chemical methods.[23]

Typically, most plasma treatments focus on altering the hydrophobicity of a fabric to better suit a chosen application or increase the efficacy of a manufacturing process (e.g., dyeing and printing in clothing production).[22] For example, wrinkle-resistant cotton has become a popular clothing fabric due to convenient and easy upkeep. Making this material wrinkle-resistant, however, decreases the comfort of the wearer due to the reduction in the fabric's moisture wicking and absorption. Lao *et al*. report the use of a combination of an O_2 plasma treatment (to add -COOH and -CO functional groups) and coating of charged silica NP (to prevent hydrophobic recovery) to decrease the water contact angle (WCA) from 139° to ~0° (water droplet completely absorbed by material).[24] Both the increased hydrophilicity and wrinkle resistant behavior were maintained even after aging and multiple laundering and

abrasion cycles. Another method to increase the hydrophilicity of a material is by depositing a hydrophilic coating with plasma polymerization. Previous work in the Fisher lab used a pulsed plasma to deposit a poly(allyl alcohol) film on silk, wool, and cotton.[25] X-ray photoelectron spectroscopy (XPS) studies demonstrated that all three fabrics were uniformly coated and all were ~90% C and ~10% O regardless of the fabric type. Although WCA data were not collected directly on the poly(allyl alcohol) coated fabrics, the coated Si wafers all had WCA < 72°, indicating the presence of a more hydrophilic surface. On the other end of the spectrum, the most common method to increase the hydrophobicity of textiles is the deposition of a fluorocarbon thin film.[22, 26] In one report, cotton and silk fabrics were coated using a C_3F_6 plasma under a variety of *P*, *p*, and treatment times.[27] For all conditions explored, the WCA increased to 121 - 123° when compared to the 0° observed with the UT fabrics. Thus, the large parameter space means that the hydrophobicity of a treated material can be tuned, further increasing the applicability of this method over other modification strategies.

The final part of the dissertation focuses on the interaction of NP with UT and plasma treated fabrics. Similar to the SMO sensor work, plasma modification was used to probe the relationship between material surface chemistry, bulk properties, and performance in a given application (preventing or limiting secondary exposure to nanomaterials). This work used either a C_3F_8 or $H_2O_{(v)}$ plasma to tune the wettability of woven and nonwoven fabrics and monitored the contamination and rerelease behavior of these samples with three types of nanomaterials. This knowledge is not only important for designing better PPE but can be used in other applications as well. For example, nanomaterial functionalized fabrics are used as gas sensors,[28] self-cleaning materials,[29] and fire protection/warning.[30] Here, understanding of what properties

increase the attachment of nanomaterials to fabrics improves the efficiency of making these materials and allows for widespread use.

1.3 Overview of Research

The major theme throughout this dissertation is utilizing LTP to optimize a material's surface properties to achieve a specific behavior. This approach of studying and relating changes in the material, plasma, and application-based performance aims to deconvolute complex systems/processes in an effort toward improving gas sensor materials and PPE. Chapter 2 provides experimental details, materials, and data fitting procedures used in Chapters 3 – 6.

Chapter 3 expands on previous work to improve the gas sensing performance of SnO_2 NP on ZrO_2 wafers. Here, sensors were treated with either an etching (CO_2) or depositing (CO) plasma as possible methods to improve sensor performance (i.e. increase response or selectivity to CO, ethanol, or benzene, decrease T_S, or improve response/recovery behavior). These sensing results were then combined with XPS characterization and OES studies to determine how the SnO_2 NP changed with plasma exposure and the impact of these changes on device performance. Additionally, the presence of both etching and film deposition species in the CO_2 plasma highlights the complex nature of these systems and the need for understanding how different parameters affect which process dominates within the system.

Efforts toward fabricating an inexpensive sensor with a low T_S, as described in Section 1.1, is presented in Chapter 4. These sensors used screen-printed electrodes on a paper substrate as the supporting material for a SnO_2 NP sensor. O_2/Ar plasma treatments (P = 15 – 60 W) were successfully used to lower the $T_S \leq 50$ °C to several target gases. These paper-based devices also demonstrated some response and recovery behavior when detecting ethanol, indicating that

plasma modification also allows for these sensors to be used more than once. OES and material studies were used to understand the modification process and how that related to the improved sensor properties.

Chapter 5 includes work completed in collaboration with Dr. Candace Tsai's research group (CSU and University of California, Los Angeles) and Dr. Ron Reifenberger (Purdue University). Here, $H_2O_{(v)}$ and C_3F_8 plasmas were used to treat four common lab coat materials (100% polypropylene, 100% cotton, 80/20 polyester cotton blend, and Tyvek®). Characterization of the fabrics before and after plasma modification was done using XPS and WCA in conjunction with nanomaterial contamination studies (quantified using scanning electron microscopy images). Comparisons of the UT, hydrophobic, and hydrophilic versions of the materials allowed for the determination of the individual effects of surface chemistry and material weave pattern on the attachment and release of Al_2O_3 NP, carbon black, and carbon nanotubes.

Chapter 6 contains preliminary results on work describing the fabrication and characterization of various nano- and micro-sized SMO as potential sensor materials. Sensor performance studies (with ZrO_2 and paper-based sensors) are included to demonstrate the applicability of these materials to be used as a traditional and paper-based sensors. Additionally, attempts at optimizing the growth of vertical graphene nanosheets (VGN) and composite SMO/VGN as well as possible explanations for challenges in the fabrication process are discussed. Possible next steps for further developing these materials into effective nanoparticle-based gas sensors are also explored.

Finally, Chapter 7 is a summary of all the work presented in this dissertation. This chapter also includes short and long-term future studies to build on the knowledge gained through these projects and address remaining hypotheses and needed optimizations.

REFERENCES

1. Enviornmental Protection Agency Air Quality Index (AQI) Basics. https://www.airnow.gov/aqi/aqi-basics/ (accessed June 2021).
2. Barsan, N.; Koziej, D.; Weimar, U., Metal Oxide-Based Gas Sensor Research: how to? *Sens. Actuators B* **2007,** *121* (1), 18-35.
3. Gardon, M.; Guilemany, J. M., A Review on Fabrication, Sensing Mechanisms and Performance of Metal Oxide Gas Sensors. *J. Mater. Sci.: Mater. Electron.* **2013,** *24* (5), 1410-1421.
4. Liu, X.; Cheng, S. T.; Liu, H., et al., A Survey on Gas Sensing Technology. *Sensors* **2012,** *12* (7), 9635-9665.
5. Ihokura, K.; Watson, J., *The Stannic Oxide Gas Sensor: principles and applications*. CRC Press, Inc.: Florida, 1994.
6. Zhang, Y.; Wang, C.; Zhao, L., et al., Preparation of Ce-Doped SnO_2 Cuboids with Enhanced 2-Butanone Sensing Performance. *Sens. Actuators B* **2021,** *341*, 130039.
7. An, D.; Liu, N.; Zhang, H., et al., Enhanced n-Butanol Sensing Performance Of SnO2-Based Gas Sensors By Doping In2O3 Via Co-Precipitation Method. *Sens. Actuators B* **2021,** *340*, 129944.
8. Stanoiu, A.; Simion, C. E.; Calderon-Moreno, J. M., et al., Sensors Based on Mesoporous SnO_2-$CuWO_4$ with High Selective Sensitivity to H_2S at Low Operating Temperature. *J. Hazard. Mater.* **2017,** *331*, 150-160.
9. Grill, A., *Cold Plasma in Materials Fabrication: from fundamentals to applications*. IEEE: New York, 1994.
10. Srivastava, R.; Dwivedi, R.; Srivastava, S. K., Development of High Sensitivity Tin Oxide Based Sensors for Gas/Odour Detection at Room Temperature. *Sens. Actuators B* **1998,** *50* (3), 175-180.
11. Stuckert, E. P.; Fisher, E. R., Ar/O_2 And H_2O Plasma Surface Modification of SnO_2 Nanomaterials to Increase Surface Oxidation. *Sens. Actuators B* **2015,** *208*, 379-388.
12. Chaturvedi, A.; Mishra, V. N.; Dwivedi, R., et al., Selectivity And Sensitivity Studies on Plasma Treated Thick Film Tin Oxide Gas Sensors. *Microelectron. J.* **2000,** *31* (4), 283-290.
13. Du, H.-Y.; Wang, J.; Yu, P., et al., Investigation of Gas Sensing Materials Tin Oxide Nanofibers Treated by Oxygen Plasma. *J. Nanopart. Res.* **2014,** *16* (2), 2216.
14. Pan, J.; Ganesan, R.; Shen, H., et al., Plasma-Modified SnO_2 Nanowires for Enhanced Gas Sensing. *J. Phys. Chem. C* **2010,** *114* (18), 8245-8250.
15. Stuckert, E. P.; Miller, C. J.; Fisher, E. R., Gas-Phase Diagnostics During H_2 And H_2O Plasma Treatment of SnO_2 Nanomaterials: implications for surface modification. *J. Vac. Sci. Technol., B* **2017,** *35* (2), 021802.
16. Stuckert, E. P.; Miller, C. J.; Fisher, E. R., The Effect of Ar/O_2 and H_2O Plasma Treatment of SnO_2 Nanoparticles and Nanowires on Carbon Monoxide and Benzene Detection. *ACS Appl. Mater. Interfaces* **2017,** *9* (18), 15733-15743.
17. Singh, A. K., Chapter 1 - Introduction to Nanoparticles and Nanotoxicology. In *Engineered Nanoparticles*, Singh, A. K., Ed. Academic Press: Boston, 2016; pp 1-18.
18. Jose Varghese, R.; Sakho, E. h. M.; Parani, S., et al., Chapter 3 - Introduction to Nanomaterials: synthesis and applications. In *Nanomaterials for Solar Cell Applications*, Thomas, S.; Sakho, E. H. M.; Kalarikkal, N.; Oluwafemi, S. O.; Wu, J., Eds. Elsevier: 2019; pp 75-95.

19. General Safe Practices for Working with Engineered Nanomaterials in Research Laboratories. National Insitute for Occupational Safey and Health: 2012.
20. McDonagh, A.; Byrne, M. A., A Study of The Size Distribution of Aerosol Particles Resuspended From Clothing Surfaces. *J. Aerosol Sci* **2014,** *75*, 94-103.
21. McDonagh, A.; Byrne, M. A., The Influence of Human Physical Activity and Contaminated Clothing Type on Particle Resuspension. *J. Environ. Radioact* **2014,** *127*, 119-126.
22. Morent, R.; De Geyter, N.; Verschuren, J., et al., Non-Thermal Plasma Treatment of Textiles. *Surf. Coat. Technol.* **2008,** *202* (14), 3427-3449.
23. Hawker, M. J.; Pegalajar-Jurado, A.; Fisher, E. R., Conformal Encapsulation of Three-Dimensional, Bioresorbable Polymeric Scaffolds Using Plasma-Enhanced Chemical Vapor Deposition. *Langmuir* **2014,** *30* (41), 12328-12336.
24. Lao, L.; Fu, L.; Qi, G., et al., Superhydrophilic Wrinkle-Free Cotton Fabrics via Plasma and Nanofluid Treatment. *ACS Appl. Mater. Interfaces* **2017,** *9* (43), 38109-38116.
25. Malkov, G. S.; Fisher, E. R., Pulsed Plasma Enhanced Chemical Vapor Deposition of Poly(allyl alcohol) onto Natural Fibers. *Plasma Process. Polym.* **2010,** *7* (8), 695-707.
26. Zille, A.; Oliveira, F. R.; Souto, A. P., Plasma Treatment in Textile Industry. *Plasma Process. Polym.* **2015,** *12* (2), 98-131.
27. Li, S.; Jinjin, D., Improvement of Hydrophobic Properties of Silk and Cotton by Hexafluoropropene Plasma Treatment. *Appl. Surf. Sci.* **2007,** *253* (11), 5051-5055.
28. Subbiah, D. K.; Babu, K. J.; Das, A., et al., NiOx Nanoflower Modified Cotton Fabric for UV Filter and Gas Sensing Applications. *ACS Appl. Mater. Interfaces* **2019,** *11* (22), 20045-20055.
29. Abidi, N.; Cabrales, L.; Hequet, E., Functionalization of a Cotton Fabric Surface with Titania Nanosols: Applications for Self-Cleaning and UV-Protection Properties. *ACS Appl. Mater. Interfaces* **2009,** *1* (10), 2141-2146.
30. Wang, B.; Lai, X.; Li, H., et al., Multifunctional MXene/Chitosan-Coated Cotton Fabric for Intelligent Fire Protection. *ACS Appl. Mater. Interfaces* **2021,** *13* (19), 23020-23029.

CHAPTER 2

EXPERIMENTAL METHODS

This chapter contains information on the materials, experimental details, and data fitting procedures used in the following chapters. This section comprises six parts: gas sensor fabrication (2.1), fabric preparation (2.2), plasma reactor and treatments (2.3), material and plasma characterization (2.4), gas sensor performance studies (2.5), and ENP attachment characterization (2.6). Ms. Sadia Sorna (Tsai Research Group) and Dr. Ronald Reifenberger (Purdue University) performed all of the ENP contamination studies (Section 2.6 and Chapter 5), and Dr. Rebecca C. Miller (CSU Analytical Resources Core) imaged these samples. I would also like to thank members of the CSU Analytical Resources Core for their assistance and expertise in collecting and analyzing the work presented herein. This research was funded by the National Science Foundation (NSF CBET-1803067) and the Department of Health and Human Services, Center for Disease Control and Prevention (R21OH011507-01).

2.1 Gas Sensor Fabrication

Traditional SnO_2 substrates were prepared similarly to previously published methods;[1] SnO_2 nanoparticles (NP) (diameter <100 nm, Aldrich) were mixed with methanol (ACS certified, Fisher Scientific) to form a slurry that was spread onto ZrO_2 wafers (50 nm ZrO_2 on *n*-type 100 Si wafer, BioStar). The substrates were dried under ambient laboratory conditions for at least 4 hr prior to use, to allow the methanol to evaporate completely. Electrodes for gas sensing

studies were made by attaching two ~1 cm Ag wires (0.25 mm diameter, 99% Sigma-Aldrich) using Ag conductive paste (Sigma-Aldrich) and curing for 1 hr at 120 °C.

For paper-based sensors, carbon paste electrodes were screen printed using a laser cut transparency stencil (pattern created using Corel Draw X4 and a 30 W Epilog Zing Laser Cutter) and a 3:7 ratio of graphite powder (diameter <20 μm, Sigma-Aldrich, St. Louis, MO) to Ercon Carbon Ink (Wareham, MA) on Whatman Grade 1 chromatography paper.[2-3] SnO_2 NP were added to the paper substrate by slowly drop-casting ~300 μL of a suspension of 0.01 g of commercially purchased SnO_2 NP (diameter <100 nm, Aldrich) in 1 mL of ultrapure water.[4-5] Although the NP did not cover the entire device, the suspension was drop cast onto the center of the electrodes to ensure NP coverage over the interdigitated part of the substrate.

SnO_2 thin film (TF) growth on a paper substrate was adapted from the sonochemical method published by Zhou *et al*.[6] Approximately 0.46 g of $SnCl_2 \cdot 2\ H_2O$ (Alfa Aesar, 98%) was added to 20 mL of ethanol (EtOH) (PHARMCO-AAPER, absolute anhydrous, ACS grade) in a beaker and stirred for 3 hr at room temperature. After stirring, 15 mL of ultra-pure water (reverse osmosis purified, ≥18 MΩ) was added to the beaker, and the solution was stirred for an additional 15 min. The Whatman paper was cut into ~0.3 g squares (~16.7 mm x ~16.7 mm), added to the solution, and bath sonicated for 4 – 6 hr. Samples were washed with EtOH and left to dry in the fume hood overnight. SnO_2 TF was also grown on the paper substrates with the carbon paste electrodes. The precursor was prepared using the same procedure; however, after the final 15 min of stirring, the solution was halved into two 30 mL glass scintillation vials. The vials had modified caps that allowed for an alligator clip that suspended the paper substrate so that it was only partially submerged in the precursor solution (Fig. 2.1).

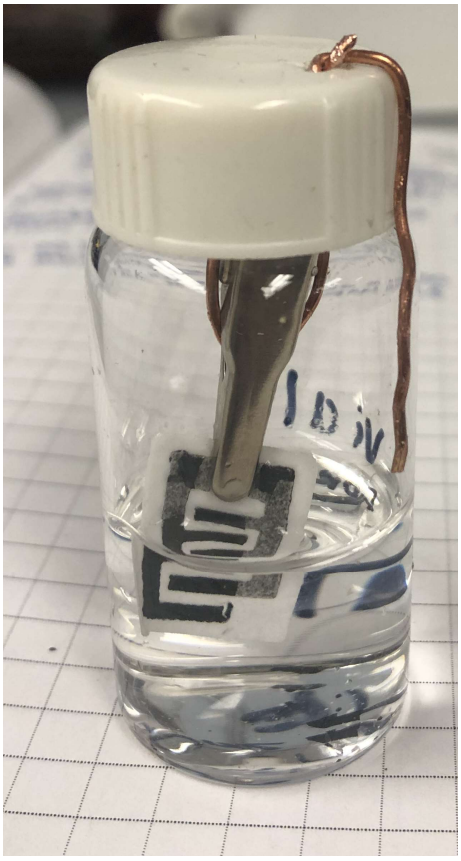

Figure 2.1. Photograph of modified glass scintillation vial used for SnO_2 TF growth on a paper substrate with printed electrodes.

ZnO microwires were grown directly on the paper and ZrO_2 substrates by adapting a synthesis from literature.[7] To a beaker, a ~0.3 g square (~16.7 mm x ~16.7 mm) of the chromatography paper and 100 mL of 0.1 M $Zn(NO_3)_2 \cdot 6\ H_2O$ (Alfa Aesar, 99%) and 0.1 M $C_6H_{12}N_4$ (Alfa Aesar, 99+%) solutions were added. A large watch glass covered the beaker, and the solution was heated to 95 °C on a hotplate for 6 hr. After growth, the substrate was rinsed with ultra-pure water and left to dry in ambient conditions overnight.

2.2 Fabric Preparation

Two woven and two nonwoven lab coats were selected for the study in Chapter 5 and were all purchased through Global Industrial: 100% cotton (Fashion Seal men's lab coat), polyester/cotton blend (80% polyester 20% cotton, Red Kap® women's button closure lab coat), Tyvek® (Dupont), and 100% polypropylene (Keystone HD polypropylene lab coat). Before use, all fabrics were cut into circular fabric samples (1.375 inch diameter) by using a punch-out cutter, enabling homogenous sample sizes for all plasma studies.

2.3 Plasma Reactor and Treatments

All plasma surface modification processes were performed in a home-built glass barrel style reactor, shown in Figure 2.2a. Briefly, discharges were ignited by supplying radio frequency (rf) power (P) through a 13.56 MHz power supply via a matching network to a Ni-plated copper induction coil. Vacuum was maintained with a mechanical pump and pressure (p) was monitored by a Baratron® capacitance monometer. The reactor stabilized at base pressure (<1 mTorr) before introduction of plasma precursors. All gaseous precursors were introduced into the reactor with a mass flow controller. After the introduction of gaseous or high vapor

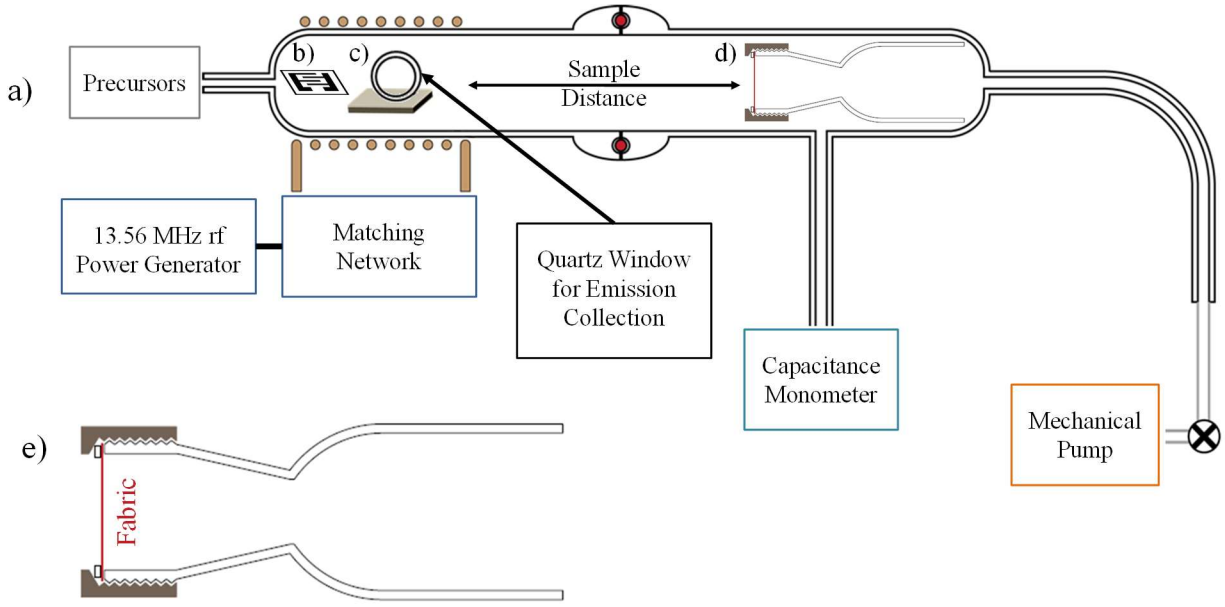

Figure 2.2. Schematic of (a) glass tubular reactor and (e) holder constructed to mount fabrics perpendicular to gas flow. Sample placement within the reactor for the (b) PGS, (c) ZrO_2 sensor, and (d) fabric holder is shown. Sample distance for fabric treatments is measured from the end of the coil to the top of the holder.

pressure liquid precursors, the pressure stabilized at the p indicated for at least 5 min before plasma ignition and for at least 5 min after plasma treatment to quench surface active sites. For all treatments, sensors were placed on a glass slide so the samples sat in the center of the reactor, and a cylindrical glass substrate holder (1.5 inch diameter) was used to orient the fabric perpendicular to the gas flow with the outside of the lab coat facing toward the coil, shown in Figure 2.2e. Sample placement within the reactor for the paper gas sensors (PGS), traditional ZrO_2 sensors, and fabric samples are shown in Figure 2.2b – d, respectively.

Studies presented in Chapter 3 used CO (≥99.0%, Sigma-Aldrich) or CO_2 (98.00%, General Air) with p = 150 mTorr and P = 25 – 100 W. Treatments using an O_2/Ar plasma, a mixture of Ar (Airgas, >99.999%) and O_2 (Airgas, >99%) was used (3:11 ratio and total p of 50 – 140 mTorr) with a P range of 15 – 60 W. For fluorocarbon (FC) plasma treatments (p = 30 mTorr, P = 50 W) C_3F_8 (Advanced Specialty Gases, >95 %) was used as received. An O_2 (Airgas, 99.9%) plasma (p = 100 mTorr, P = 100 W) was used between C_3F_8 treatments to remove potential FC film growth on the plasma reactor walls. Prior to use, ultra-pure H_2O (reverse osmosis purified, ≥ 18 MΩ) in a side arm vacuum flask was freeze-pump-thawed at least four times and during $H_2O_{(v)}$ plasma treatment (p = 15 mTorr, P = 30 W), water vapor was flowed into the reactor via a needle metering valve.

2.4 Material and Plasma Characterization

Scanning electron microscopy (SEM). Samples were imaged on a JEOL JSM-6500F with a field emission source, accelerating voltage of 3.0 – 15.0 kV; ~10 mm working distance and tandem energy-dispersive X-ray spectroscopy (EDS) (15 kV accelerating voltage). Prior to imaging, fabric pieces were cut into ~2 cm x 2 cm pieces from the center of the circular samples

and coated with 25 – 50 nm of Au. All contaminated fabrics were imaged ~36 hr after plasma treatment. Vertical graphene nanosheets were also sputter coated with ~20 nm of Au before SEM imaging.

X-ray photoelectron spectroscopy (XPS). All samples were analyzed within 24 h of plasma treatment (unless otherwise labeled) with a PHI-5800 ESCA system with a monochromatic Al Kα X-ray source (1486.6 eV photons), and spectra were fit with CasaXPS v2.3 software. For the high-resolution (HRes) XPS spectra, individual binding environments used a Gaussian-Lorentzian (30:70) fit, and the FWHM were constrained to ≤2.0 eV. Peak positions were charge corrected by setting the higher energy Sn3d peak to 486.6 eV or the C-C/C-H component to 284.8 eV. A Shirley background was used for all HRes spectra except for Sn_{3d}, which used a Tougaard background. All reported values represent the average and standard deviation from 2 – 3 sampling areas on 3 samples (i.e. n≥6). Atomic ratio percentages for the CO P = 25 W samples were calculated by omitting the Na_{KLL} contributions from the O_{1s} and Sn_{3d} peaks when present.

Fourier-transform infrared (FTIR) spectroscopy. FTIR measurements were collected on a Thermo Scientific Nicolet 6700 FTIR spectrometer (Madison, WI). KBr pellets were made with ~0.3 g of FTIR grade KBr (≥99% trace metals basis, Sigma Aldrich) and analysis of the CO plasma treated samples were done immediately after plasma modification. The instrument was purged with N_2 gas for >4 hr before analysis, and the baseline was corrected using the included software (Omnic v8.2).

Water contact angle (WCA) measurements. Experiments were performed using a Krüss DSA30 goniometer to quantify the wettability of the samples. Substrates did not require further sample preparation for WCA analysis; all data were collected under ambient laboratory

conditions at 22 ± 2 °C and <25% relative humidity. The probe liquid parameters (density 0.9970 g/mL, viscosity = 0.010 P, surface tension = 72.16 mN/m) were programmed into the onboard software and employed for all WCA fitting. Static and dynamic (i.e., time-resolved) WCA data were collected depending on the nature of substrate (i.e., hydrophilic or hydrophobic). Static WCA measurements were collected with a 2 μL drop of ultra-pure H_2O (Millipore, ≥18 MΩ); 4 μL drops were used in dynamic WCA measurements. Generally, the circle method was employed to fit hydrophilic surfaces and the tangent-1 algorithm was used to fit hydrophobic surfaces. Water adsorption rates were determined via video analysis, $t = 0$ s is defined as when the water droplet first contacts the material surface. An adsorption rate was calculated by dividing the drop volume by the time it took for the drop to be completely absorbed by the material. WCA measurements were performed <1 hr after plasma treatment for the fresh samples and after 48 hr and 28 days for the aged samples (2-day and 1-month, respectively). Aged samples were stored in ambient laboratory conditions with minimal exposure to light. All WCA data are averages of at least 3 spots on 3 samples.

Optical emission spectroscopy (OES) measurements. For OES measurements, the precursor pressure was lowered to allow for the addition of 10% Ar to the system. A fused quartz window was installed on the reactor (Fig. 2.2a). An Avantes AVASPEC-3648-USB2-RM multichannel spectrometer and accompanying software were used to collect spectra both with and without a substrate using a 50.00 ms integration time and 600 averages, described previously.[8] Relative species densities (denoted as [X], where X is the excited state species) were calculated by averaging the actinometric intensity ratio using the 750.3 nm excited state Ar line as the actinometer. [O], [H], and [CO] were determined using the 844.7 nm, 656.5 nm, and 483.5 nm emission lines, respectively. All calculated values represent values after 2.5 min of

plasma exposure; however, spectra were collected every 30 s during the 5 min plasma on time and were consistent throughout the entire plasma on time.

2.5 Gas Sensor Performance Studies

Gas sensing performance studies utilized a home-built sensing apparatus, described previously,[9] with the addition of mass flow controllers to allow for the use of various analyte gases in a time-resolved manner. The relative humidity inside the sensing chamber was ~15 – 20% and a flow rate of 25 sccm for each gas was used in all the studies presented herein. For EtOH vapor exposure, air (Airgas, breathing quality) was bubbled through EtOH (PHARMCO-AAPER, absolute anhydrous, ACS grade) and allowed to flow into the sensing chamber. The other two gases used were CO (Matheson, 99.8 ppm, air balance) and benzene (Matheson, 94.3 ppm, air balance). Static resistance measurements were collected as a function of T_S by flowing a single gas over the sensor for approximately 10 min at each T_S, starting at 25 °C and increasing to 100 or 300 °C, then decreasing back down to 25 °C. The temperature dependent response to a target gas is defined as:

$$\text{Response} = \frac{R_{air}}{R_{gas}}$$

where R_{air} and R_{gas} are the weighted average (n = 3 per gas) of the resistance in air and target gas, respectively. All response plots have error bars representing the weighted, propagated error for these calculated responses.

For dynamic response and recovery studies, a target gas on/off time of 5/10 min was used. At the start of each "off time" a higher flow rate (~50 sccm) of only air was used for ~2 min as a brief flushing step to ensure removal of the target gas, then reduced to 25 sccm for the remaining ~8 min of the "off time". This flushing step was added to allow for quick removal of

the analyte gas as the sensing chamber does not have the aid of a fan or pump. Recovery times were calculated by measuring the time it took for the sensor to reach 90% of the maximum resistance during each individual "off time" following the EtOH exposure and averaging those values over the three cycles for each sensor trial. As discussed in the results/discussion section in Chapter 4, because the resistance of the PGS did not stabilize during EtOH exposure, we do not report response times using this method. Instead, we present an alternate method for estimating the responsiveness of our sensors. For this value, we calculated response rates by determining the slope of the decay between the on point and off point of each EtOH exposure using a linear regression.

2.6 ENP Attachment and Characterization

For all contamination studies, four samples of each type of fabric (UT, FC, and $H_2O_{(v)}$) were prepared at a time and within 48 hr of plasma treatment. Fabrics contaminated with Al_2O_3 and carbon black were prepared in a home-built glovebox, and a steel wire mesh was used to evenly distribute ~0.20 g of Al_2O_3 or ~0.14 g of carbon black onto the 12 fabric swatches. Excess ENPs were then removed by gently tilting the fabric patch. Fabrics were contaminated with CNT in an enclosed hood in a class 100 cleanroom using a Powder Dispersion Generator RBG 1000 (operated at $p =$ 2 bar and 10 mm/hr feeding rate for 10 min) to limit CNT agglomeration. After patch contamination, the air was purged/cleaned inside the enclosure. Two of the four patches were then shaken manually for two min each to release the ENPs from the fabrics.

For the ENP counting analysis, the SEM images were uploaded into the software Fiji, and a line tool was used to measure the longest side of the agglomerates, and the measurements were

exported into Excel. Due to the different shapes of the CNT compared to the spherical ENPs, the number of CNT clusters and individual fibers was counted instead of agglomerates as a function of size. Counts reported in Tables 5.4 – 6 and Figures 5.7 – 10 represent the total number of agglomerates or individual CNT over several spots on two contaminated and two shaken samples. For analysis of same spot images, a counting grid was placed over the SEM images, and individual NP were outlined in circles. The circles were then sorted by size and counted, and a histogram was generated for each type of fabric and ENP combination.

REFERENCES

1. Stuckert, E. P.; Fisher, E. R., Ar/O_2 and H_2O Plasma Surface Modification of SnO_2 Nanomaterials to Increase Surface Oxidation. *Sens. Actuators B* **2015,** *208*, 379-388.
2. Martín-Yerga, D.; Álvarez-Martos, I.; Blanco-López, M. C., et al., Point-of-need Simultaneous Electrochemical Detection of Lead and Cadmium Using Low-Cost Stencil-printed Transparency Electrodes. *Anal. Chim. Acta* **2017,** *981*, 24-33.
3. Berg, K. E.; Adkins, J. A.; Boyle, S. E., et al., Manganese Detection Using Stencil-printed Carbon Ink Electrodes on Transparency Film. *Electroanalysis* **2016,** *28* (4), 679-684.
4. Gimenez, A. J.; Yáñez-Limón, J. M.; Seminario, J. M., ZnO−Paper Based Photoconductive UV Sensor. *J. Phys. Chem. C* **2011,** *115* (1), 282-287.
5. Gimenez, A. J.; Luna-Bárcenenas, G.; Sanchez, I. C., et al., Paper-Based ZnO Oxygen Sensor. *IEEE Sens. J.* **2015,** *15* (2), 1246-1251.
6. Zhou, X.; Huang, B.; Zou, Y., et al., Cotton-Templated Fabrication of Hierarchical SnO_2 Mesoporous Microtubes as the Anode Material of Lithium Ion Battery. *Mater. Lett.* **2014,** *120*, 279-282.
7. Vayssieres, L.; Keis, K.; Lindquist, S.-E., et al., Purpose-Built Anisotropic Metal Oxide Material: 3D Highly Oriented Microrod Array of ZnO. *J. Phys. Chem. B* **2001,** *105* (17), 3350-3352.
8. Stuckert, E. P.; Miller, C. J.; Fisher, E. R., Gas-phase Diagnostics During H_2 and H_2O Plasma Treatment of SnO_2 Nanomaterials: Implications for Surface Modification. *J. Vac. Sci. Technol., B* **2017,** *35* (2), 021802.
9. Stuckert, E. P.; Miller, C. J.; Fisher, E. R., The Effect of Ar/O_2 and H_2O Plasma Treatment of SnO_2 Nanoparticles and Nanowires on Carbon Monoxide and Benzene Detection. *ACS Appl. Mater. Interfaces* **2017,** *9* (18), 15733-15743.

CHAPTER 3

COMPARISON OF CO AND CO_2 RF PLASMA TREATMENT OF SNO_2 NANOPARTICLES FOR GAS SENSING MATERIALS[1]

This work focuses on using CO and CO_2 plasmas to modify SnO_2 nanoparticles (NP) to understand the role of key gas-phase species and to explore a potential route for improving these materials as solid-state gas sensors. Spectroscopic studies reveal that in the CO_2 plasma, CO_2 decomposes to CO and O, leading to etching of the SnO_2 lattice. Conversely, in the CO plasma, very little O is formed, leading to the deposition of a carbonaceous film on the SnO_2 NP. Finally, sensors fabricated with the CO_2 modified SnO_2 NP demonstrate a higher response to CO, benzene, and ethanol and improved response and recovery behavior when compared to untreated devices. CO plasma modification, however, had a detrimental effect on the gas sensing performance of this material. This work was funded by the National Science Foundation (NSF CBET-1803067).

3.1 Introduction

Their tunable nature and large parameter space make plasmas a useful material modification tool for a variety of applications (e.g. gas sensing, energy storage, biomedical devices, etc.).[1-4] In general, plasmas can functionalize, etch, or deposit a film on the surface of a material, modifying only the outer few layers of the overall substrate. Although plasma parameters also play a role, the plasma precursor often has the largest effect on determining which of these processes (or combination thereof) the plasma exhibits. The impact of precursor

[1] Reproduced from the manuscript submitted and under review to the *Journal of Vacuum Science and Technology A* by K. A. M. Hiyoto, E. P. Stuckert, and E. R. Fisher

is especially evident in systems where competing processes occur simultaneously. For example, in fluorocarbon plasmas, precursors decompose into species that contribute primarily to film deposition (CF_x radicals) and ones that primarily etch (F atoms). Depending on the precursor gas (and ultimately the dominating species), plasmas like C_3F_8 and hexafluoropropylene oxide deposit amorphous fluorocarbon films, whereas CF_4 and C_2F_6 plasmas result in etching of the material, presumably as a result of the differences in precursor F/C ratios.[5-6]

Another example of these competing processes is found in CO_2 plasmas. Upon plasma ignition, the CO_2 can decompose into CO (contributes to film deposition) and O atoms (an etchant in many systems).[7] Exploring CO_2 plasmas and the balance between competing processes affords the opportunity to expand our understanding of the underlying chemistry and its impact on the dominant process(es). In particular, in this system the etching process can be suppressed by employing CO as the precursor gas. CO undergoes minimal decomposition and the likelihood of two CO molecules forming CO_2 (+ O) that can then be decomposed again is low.[7-8] CO is often used as a precursor gas in plasma enhanced chemical vapor deposition (PE-CVD) systems to deposit diamond-like carbon films on a variety of substrates.[8-12] Although there have been extensive studies on both CO and CO_2 plasmas individually, studies directly comparing these systems are limited. Kwon et al. examined the effect of additions of CO or CO_2 on the etching rate of tungsten and SiO_2 in a CF_4/O_2 plasma. The etch rate and selectivity of tungsten increased with the addition of either CO or CO_2; however, this increased rate was only seen with additions of up to 1 and 5 sccm of CO and CO_2, respectively.[13] The authors state that addition of small amounts of CO results in a significant decrease in CF_x radicals in the system, leading to enhanced etching. When more than 1 sccm of CO is added, however, the etch rate decreased when compared to the system without CO and the surface of the tungsten film had

more carbon-containing residues. With the $CF_4/O_2/CO_2$ system, the addition of CO_2 allowed for the formation of more O and F atoms and more efficient etching of the substrate. Although these results support the opposing roles of CO and O in a plasma, the CO and CO_2 were additives to a multi-gas etching system. Thus, elucidating the specific effects of these species on materials in the plasma is complicated, and a comparison of plasmas wherein CO and CO_2 are the major components of the precursor gas could provide valuable insight.

One place where understanding this etching/deposition balance is critically important is the application of CO or CO_2 plasmas in the context of surface modification of materials needed for high-end applications (e.g. sensors). Metal oxide gas sensors are highly sensitive to changes in surface chemistry and morphology as the sensing mechanism relies on gases interacting with the surface of the material to cause changes in bulk resistance. For n-type semiconductors like SnO_2, O_2 will adsorb onto the surface in an oxidizing interaction upon exposure to the atmosphere. This results in an observed increase in material resistance.[14-15] Conversely, reducing gases (like CO, ethanol, and benzene) interact with this adsorbed layer of oxygen and desorb, decreasing the material resistance. Moreover, the reactivity of the adsorbed oxygen is highly dependent on the sensor operating temperature (T_S), making most SnO_2 sensors only effective at 300 °C or higher.[14-15] Clearly any changes to the surface chemistry or morphology through either etching or deposition could significantly affect how a target gas might interact with the metal oxide substrate as well as potentially lowering the effective T_S.

Previous work in our laboratory modified SnO_2 nanoparticle sensors with a variety of plasma systems (Ar/O_2, H_2, and $H_2O_{(v)}$)[16-19] to improve sensor performance and elucidate the effects of plasma treatment on the material and the resulting sensing behavior. After O_2/Ar plasma modification, sensors (supported both via a traditional ZrO_2 wafer substrate and a novel

complex paper substrate) had an increase in adsorbed oxygen (O_{ads}) and demonstrated larger responses to select gases when compared to the untreated (UT) material.[16-18] SnO_2 treated with H_2 and $H_2O_{(v)}$ plasmas, however, resulted in the SnO_2 being completely reduced to metallic Sn.[18-19] Interestingly, although these systems etched the material similar to the O_2/Ar plasma, this modification resulted in changes that detrimentally impacted gas sensing behavior. Thus, in addition to understanding the etching/deposition competition in CO and CO_2 plasmas, the present work also aims to demonstrate their utilization to improve the gas detection performance of SnO_2 nanoparticle sensors.

6.2 Results and Discussion

During plasma modification of the SnO_2 NP, excited state species were monitored using OES. Representative raw spectra of the four systems (CO and CO_2 plasmas, with and without SnO_2) at P = 25 W can be seen in Figure 3.1, for the entire spectral range studied. Peaks from the CO Ångström (450 – 560 nm) and 3rd positive (283 – 330 nm) bands clearly dominate all four spectra, along with Ar lines (695 – 911 nm) from inclusion of ~10% Ar to the system. Although the CO_2 plasma was generated from a feedgas mixture containing only CO_2 and Ar, the most intense peaks in the spectra are attributed to excited state CO. It is well understood that CO_2 decomposes via Eq. (1)[7, 20-23]

$$CO_2 \rightarrow CO + \frac{1}{2}O_2 \qquad (1)$$

As seen in Figure 3.2, other studies have demonstrated that the CO molecule in both CO_2 and CO plasmas does not efficiently decompose further into atomic C and O.[7-8, 22, 24] From Figure 3.2, which contains expanded views of key spectral areas for the four systems, the main

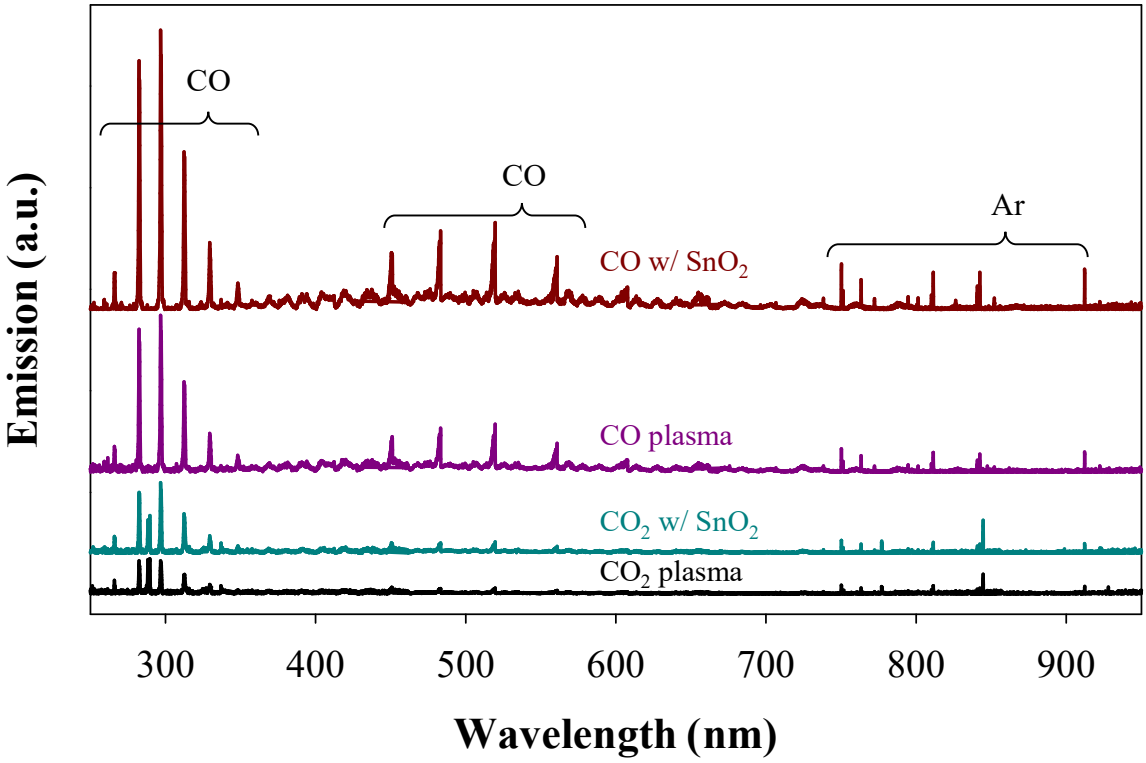

Figure 3.1. Raw OES spectra of the four plasma systems investigated at p = 150 mTorr and P = 25 W across the entire spectral range studied. Labels correspond to major peaks common to all systems.

difference between the excited state gas-phase species within these two plasmas is the presence of atomic O (777 and 844 nm). In addition, the CO_2^+ emission band can also be seen only in the spectrum of the CO_2 plasma (Fig. 3.2a), a feature found in most CO_2 discharges resulting from the $A^2\Sigma^+ - X^2\Pi$ transition of CO_2^+.[25]

Using rare gas actinometry, relative species densities were calculated for CO and O (Fig. 3.3). At all powers investigated, [CO] was higher in both CO plasma systems when compared to the CO_2 systems. Under most conditions, the relative species densities with and without a SnO_2 NP substrate are within error of each other, indicating the types of gas-phase species present are not strongly influenced by the SnO_2 NP material in the plasma and the majority of the excited state species are products of the plasma feed gas. One exception is the [CO] in the CO plasma at 50 and 75 W where the presence of SnO_2 in the plasma lead to more excited state CO in the gas phase. The [O] was also monitored as a function of *P* and, as similarly seen in the study by Kwon et al., the [O] in the CO_2 plasma is significantly larger than in the CO plasma where [O] $\leq$0.10.[13] As previously noted, atomic O arises primarily from decomposition of CO_2 via Eq. (1), but in the CO plasma the O mainly comes from decomposition of CO to C and O. Similarly, Yasuaki et al. identified small amounts of atomic O in their CO emission spectra, but these lines were barely distinguishable from spectral noise.[8] It is also possible that some of the O could be generated from etching the SnO_2 NP or the glass reactor walls. As with the [CO], however, the SnO_2 is likely not contributing because in both the CO_2 and CO plasmas the [O] is the same within error) with and without the NP. The numerical values of all relative species densities can be found in Table 3.1. Note that under some conditions, small amounts of Sn were observed in (the gas phase, an additional indicator of some etching of the NP. This was also seen in previous studies from our laboratory, wherein SnO_2 NP were treated in a H_2 plasma at 100 and 150 W and

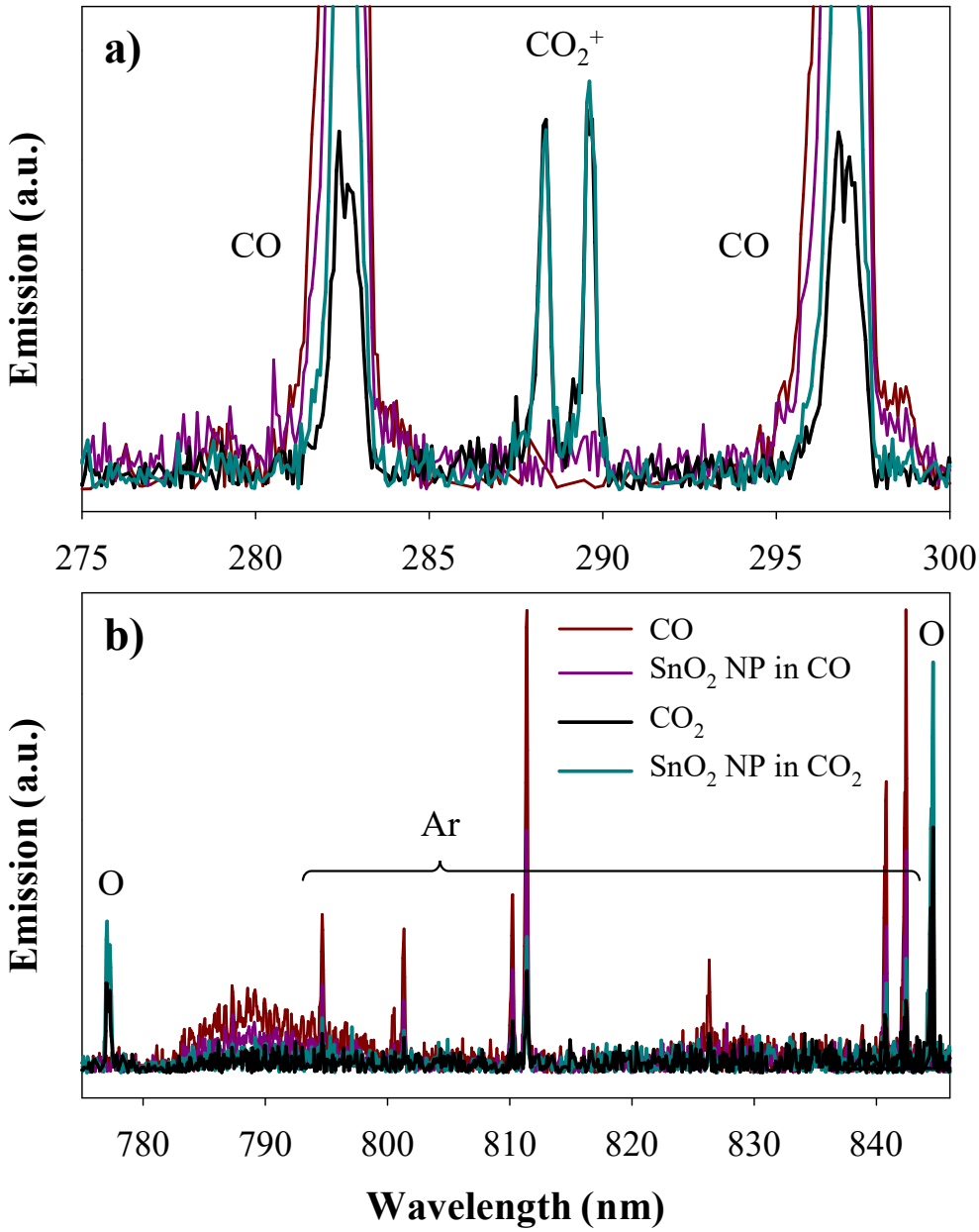

Figure 3.2. Raw OES spectra of the four plasma systems investigated at p = 150 mTorr and P = 25 W. Two spectral regions are expanded to highlight peaks of interest in the (a) 275 – 300 nm and (b) 775 – 846 nm regions. Inset labels correspond to the peak identities.

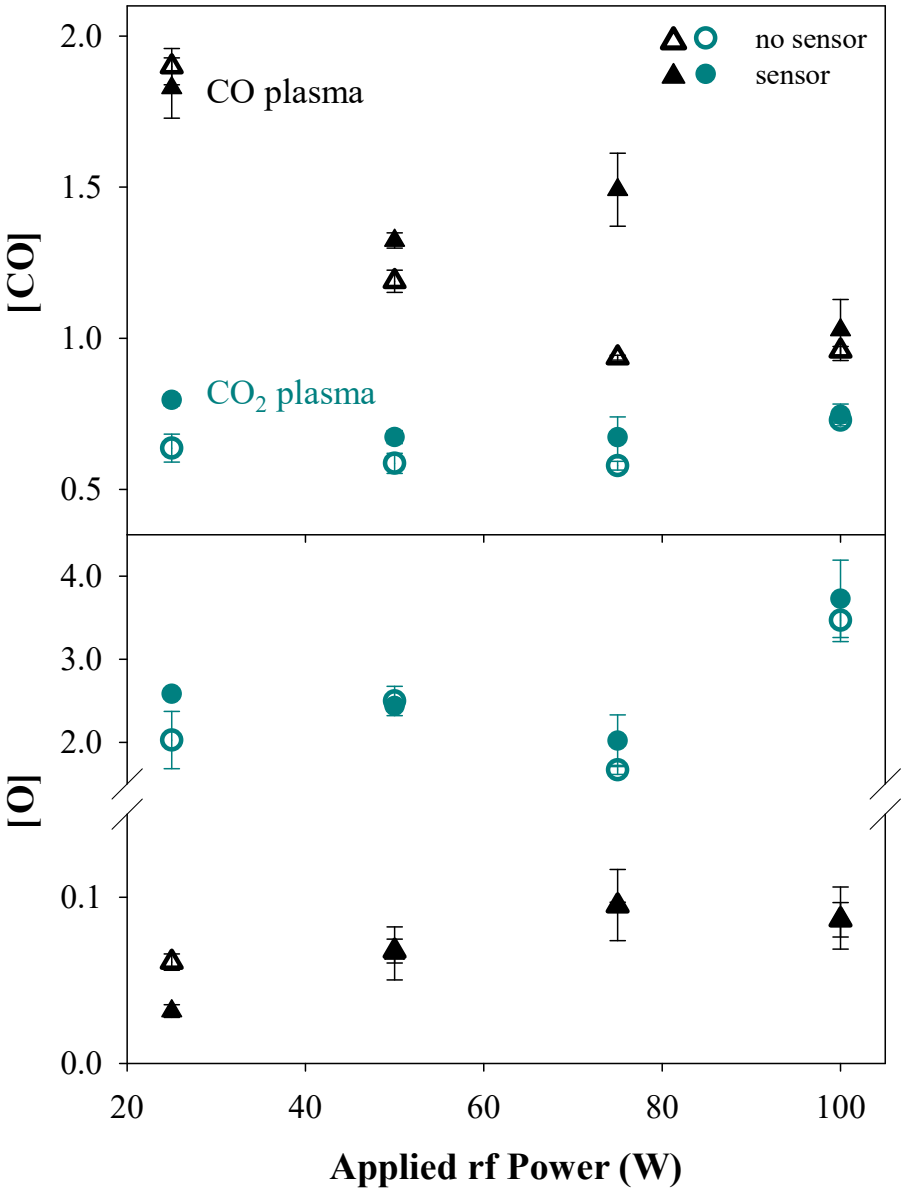

Figure 3.3. Relative species densities in CO (black triangles) and CO_2 plasmas, (blue circles), with (open) and without (closed) SnO_2 NP. Densities represent values after 2.5 min of plasma exposure at each *P*.

p = 80 mTorr.[19] Similar to the CO_2 system, the H_2 plasma etches the SnO_2 lattice, leading to the generation of excited state Sn and O-containing products observed with OES.

After plasma exposure, NP substrates were analyzed using XPS to understand the impact of plasma treatments on the surface chemistry of these materials. Figure 3.4 shows a representative HRes spectra of the CO treated SnO_2 (p = 150 mTorr, P = 25 and 100 W); the calculated XPS atomic compositions for all plasma treated SnO_2 can be found in Table 3.2, along with previously published results for the UT material.[17] After CO plasma treatment at P = 25 W, there is clear evidence of carbon film deposition on the surface, resulting in the increase from ~8.6 to ~70.7% C. This is accompanied by a drastic decrease in the percent Sn and O at the surface. The resulting film from this treatment primarily consists of sp^3 carbon, but there are also some oxygen functional groups on the surface. Centered at ~533 eV, the O-C peak is ~50% of the O composition.

Yasuoka, et al. examined diamond-like carbon films grown on Si using a CO rf plasma (p = 2.6 – 80 Pa, P = 25 – 200 W).[8] Both FT-IR spectra and Rutherford backscattering with elastic recoil detection analysis (RBS/ERDA) reveal the films deposited from CO plasmas were a mixture of C and O (~76% and ~20%, respectively from RBS/ERDA results), very similar in composition to the films grown in this study. Yasuoka, et al. did detect ~4% H incorporation in their films; however, they attributed this to contamination in the reaction chamber as they also analyzed films deposited from C_2H_2 plasmas using the same reactor. Another study deposited compositionally similar films using an atmospheric dielectric barrier discharge CO plasma.[26] Gravimetric analysis of the deposited films showed the samples comprised C (41%), O (51%), and H (3%). Geiger et al. determined that their hydrogen contamination was the result of atmospheric water absorbing and reacting with the freshly grown film during the scraping

Table 3.1. Select relative species densities of all plasma systems investigated.

Plasma	*p* (mTorr)	*P* (W)	[CO]	[O]	[Sn]
With SnO_2 NP					
CO	150 mTorr	25	1.83 (0.10)	0.03 (0.00_4)	--
		50	1.32 (0.03)	0.07 (0.02)	--
		75	1.49 (0.12)	0.10 (0.02)	--
		100	1.03 (0.10)	0.09 (0.02)	--
CO_2	150 mTorr	25	0.80 (0.02)	2.58 (0.05)	0.11 (0.19)
		50	0.67 (0.02)	2.44 (0.04)	--
		75	0.67 (0.07)	2.02 (0.31)	--
		100	0.75 (0.04)	3.73 (0.47)	--
Plasma Only (no substrate)					
CO	150 mTorr	25	1.90 (0.06)	0.06 (0.00_5)	--
		50	1.19 (0.04)	0.07 (0.01)	--
		75	0.94 (0.01)	0.09 (0.00_2)	--
		100	0.96 (0.01)	0.09 (0.01)	--
CO_2	150 mTorr	25	0.64 (0.05)	2.03 (0.34)	--
		50	0.59 (0.03)	2.50 (0.18)	--
		75	0.58 (0.01)	1.67 (0.05)	--
		100	0.73 (0.01)	3.47 (0.26)	--

Means and standard deviation (represented by numbers in parenthesis) represent an n≥3 trials.

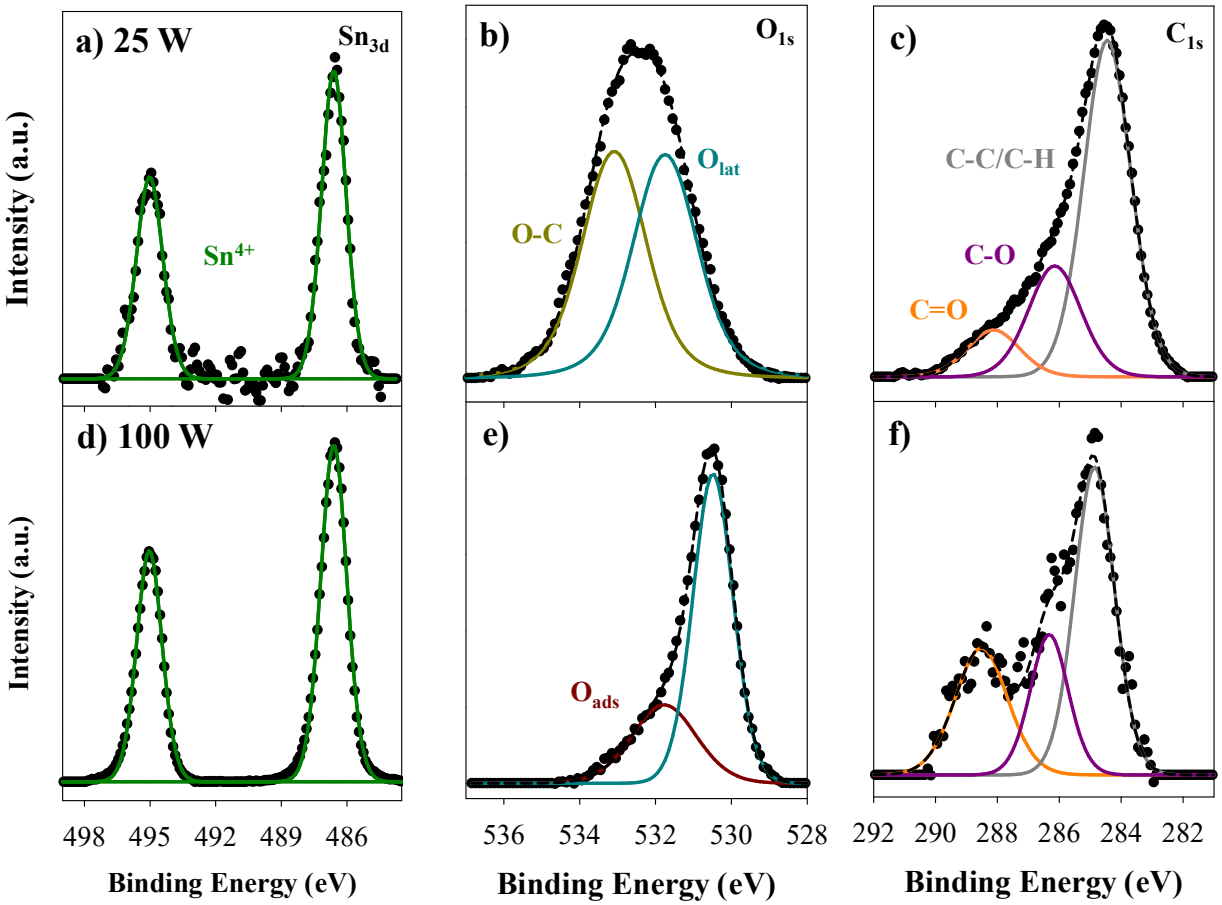

Figure 3.4. High resolution (a, d) Sn_{3d}, (b, e) O_{1s}, and (c, f) C_{1s} XPS spectra of SnO_2 modified with a CO plasma at (a – c) 25 and (d – f) 100 W. Labels represent fitted binding environments.

Table 3.2. XPS Atomic Composition and Ratio of O Binding Environments

	rf Power (W)	C (%)	Sn (%)	O (%)	O_{ads} / O_{lat}*	Na (%)
	0	8.6 (3.5)	35.6 (7.3)	55.8 (4.2)	0.254 (0.073)	--
CO_2	25	--	42.3 (0.4)	57.7 (0.36)	0.492 (0.045)	--
	50	--	41.3 (0.9)	58.7 (0.9)	0.331 (0.077)	--
	75	--	42.1 (1.1)	57.9 (1.0)	0.362 (0.019)	--
	100	--	42.5 (0.5)	57.4 (0.5)	0.566 (0.079)	--
CO	25	70.7 (5.1)	1.0 (0.4)	26.3 (3.2)	--	1.7 (1.3)
	100	10.3 (3.7)	35.6 (4.4)	54.1 (3.2)	0.411 (0.027)	--

Means and error (represented by numbers in parenthesis) represent an $n \geq 9$ sample.
*For all but UT samples (0 W), ratio reported is the weighted average with associated error. Values for UT samples represent the mean and one standard deviation.

films cannot be explicitly determined with XPS, we did try to limit post-deposition contamination. Specifically, all samples were allowed 5 min of CO gas flow following plasma exposure to quench any remaining active sites on the material with only the precursor gas. The success of this step is difficult to determine from these XPS studies alone as both CO plasmas deposited films had most of the C bound as C-C/C-H, so it is possible that our films also have some undetected hydrogen incorporation. Preliminary FTIR studies (Fig. 3.5), indicate that both the UT and 25 W CO plasma treated KBr pellets have similar spectra, making it difficult to definitively determine if our films have some hydrogen incorporation.

As the O-C and SnO_2 lattice O (O_{lat}) peaks overlap, it is difficult to discern if the O_{ads} peak is also present in these CO plasma-treated samples, but this is unlikely because film deposition covers the vast majority of the SnO_2. In some of the 25 W treated samples, the spectra reveal a small amount of Na (1.7%) and corresponding contributions from the Na Auger peaks can be seen in the HRes Sn_{3d} and O_{1s} spectra. It is unlikely that this results from sample handling contamination as Cl was not detected in the survey scans (Fig. 3.6). Instead, we believe the Na arises from the walls of the plasma reactor, which primarily consist of Si, O, and Na, and becomes incorporated into the carbon films during plasma exposure. A similar situation was previously reported in our lab with Si contamination of O_2 plasma-treated TiO_2 NP (p = 200 mTorr, P = 75 – 220 W).[27] The Si in these samples ranged from ~4 to 21% and although the NP were on a F:SnO_2 glass substrate, it was determined that the Si was coming from the reactor walls and was dispersed throughout the top 100 nm of the TiO_2 films.

From a compositional perspective, the CO 100 W plasma-treated samples, however, look very similar to the UT material with no increase in percent C on the surface. This result is somewhat unexpected given the depositing behavior usually observed in CO rf plasmas and the

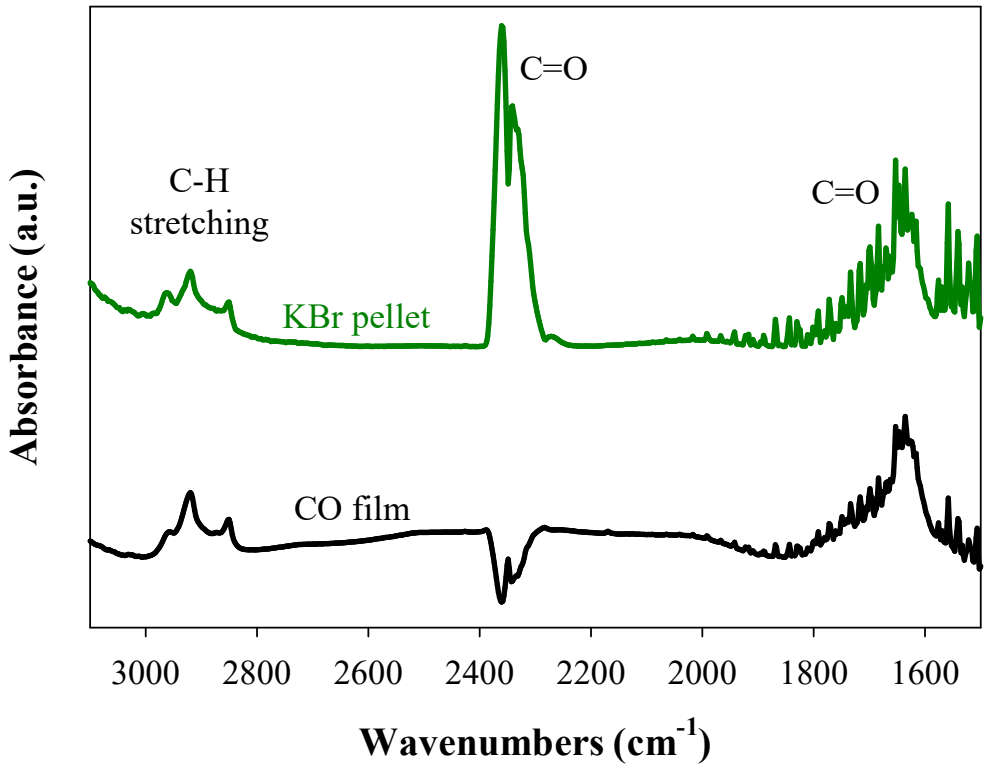

Figure 3.5. FTIR spectra of the UT (top, green) and the 25 W CO plasma treated (bottom, black) KBr pellet.

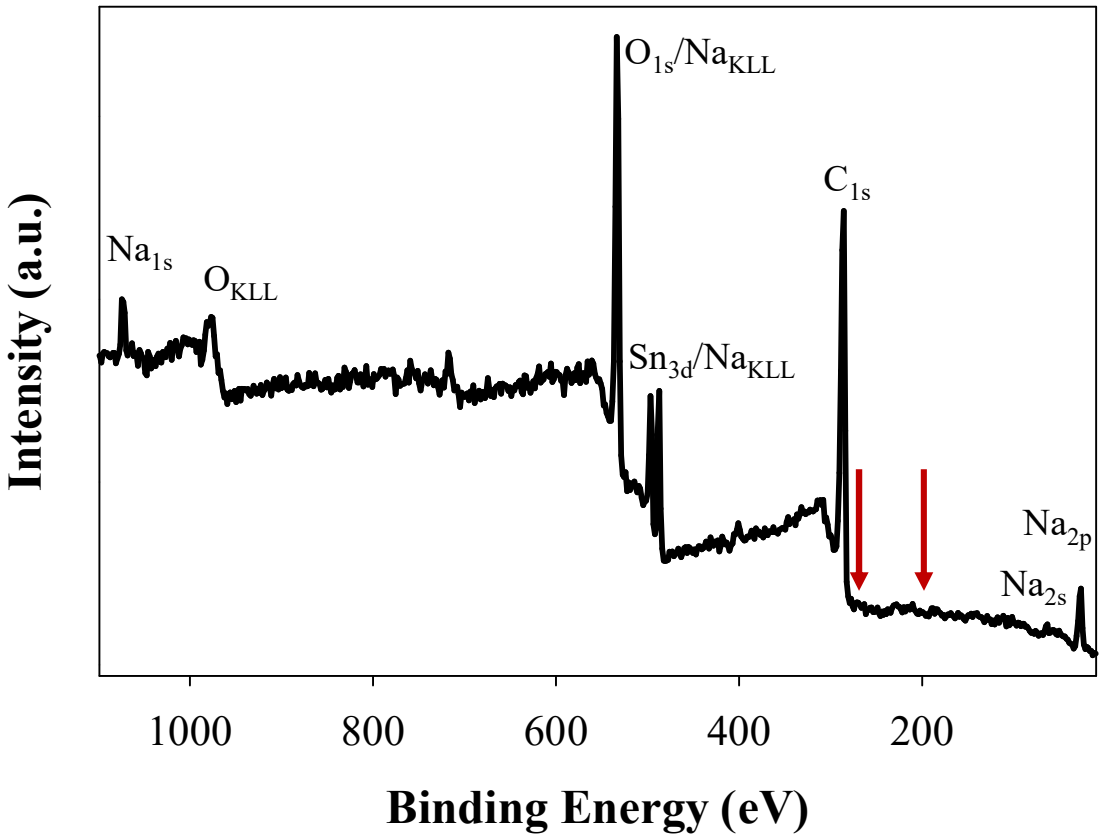

Figure 3.6. Representative survey spectrum of CO treated (P = 25 W) SnO_2 NP. Inset labels denote indicated regions and red arrows denote where the Cl_{2s} and Cl_{2p} regions should be.

analysis of the 25 W CO plasma treated NP.[8, 12, 26] Examining the excited-state gas-phase data (Fig. 3.3), the lack of film deposition aligns with the observed [O] and [CO] trends. As discussed in the Introduction, the CO molecule is believed to be the main species involved in carbon film deposition, whereas atomic O is an etchant. When both species are present, the system could clearly have competing etching and deposition processes, with the overall behavior relying on the dominating species. In the 25 W CO plasma, [CO] is the highest of all conditions investigated and [O] is the lowest, Fig. 3.3. Thus, deposition is the dominant process under these conditions. At the higher powers, [CO] generally decreases and [O] increases, indicating that the CO plasma transitions from film deposition to an etching dominated system. There is still some deposition occurring in the 100 W CO system as the C_{1s} spectra on these samples display an increased amount of C-O and C=O when compared to the spectrum of adventitious carbon on the UT material, which primarily consists of aliphatic carbon (i.e. C-C/C-H binding environment). Although the overall amount of carbon did not increase, the HRes spectra indicate that the surface carbon is slightly compositionally different than the adventitious carbon. Rather, it is likely a thin carbonaceous film deposited by the CO plasma that was not fully etched away by the oxygen in the system. From the O_{1s} spectra, there are two regions corresponding to O_{ads} and O_{lat}, similar to the untreated NP.[17] As stated previously, the amount of O_{ads} is thought to be important for the gas sensing performance of these materials; thus, the O_{ads}/O_{lat} ratio was calculated for these samples. For the 100 W treated samples, the O_{ads}/O_{lat} increased from ~0.254 to 0.411 when compared to the UT SnO_2, suggesting a significant increase in O_{ads}.

After CO_2 plasma modification, the SnO_2 NP HRes spectra for the 25 – 75 W plasma treated samples (Fig. 3.7) look very similar to the CO 100 W treated and UT samples. For these conditions, the XPS atomic compositions of Sn and O are within experimental error of the UT

SnO_2 NP; however, the O_{ads}/O_{lat} increased after CO_2 plasma exposure. This suggests that O within the lattice of the material was etched and then during post-plasma gas flow or exposure to the atmosphere, more O adsorbed to these vacant sites. Note that for some spots on the 100 W CO_2 treated materials, an additional CO_x functionality was observed in both the Sn_{3d} and O_{1s} HRes spectra. This additional region is likely an indication that along with etching the SnO_2 lattice, the CO_2 plasma resulted in some irregular functionalization of the surface.

Although CO_2 plasmas are not commonly used to modify metal oxides, they are often used for functionalization of polymer membranes for wastewater treatment.[28-31] Compared to an O_2 plasma, CO_2 modification allows for the implantation of O-containing functional groups with less morphological damage and longer treatment stability. In one study,[30] XPS analysis revealed that post plasma treatment, polypropylene, polycarbonate, and polysulfone membranes all had increased oxygen content resulting from additional carbonyl and carboxylic acid groups. Water contact angle measurements also indicated O-functionalization and a more hydrophilic surface, with either a significant decrease in contact angle or complete absorption of the water drop during analysis. Clearly, CO_2 plasma exposure readily incorporated oxygen into these soft, polymeric materials. In this work, however, functionalization of SnO_2 was observed only sporadically and under the harshest condition (i.e. highest P and p), as seen in Figure 3.8. One consideration regarding these differences in functionalization comes from consideration of the energy needs in each case. Functionalization of the polymeric membranes first requires chain scission, which is easiest at aliphatic C sites (bond energies of C-C and C-H are ~360 and ~410 kJ/mol, respectively)[32]. In contrast, with the SnO_2 NP substrates, scission of an Sn-O bond requires a substantially higher amount of energy (bond energy of 548 kJ/mol[32]). Thus, only at $P =$ 100 W does the plasma have enough energy to allow for some functionalization similar to

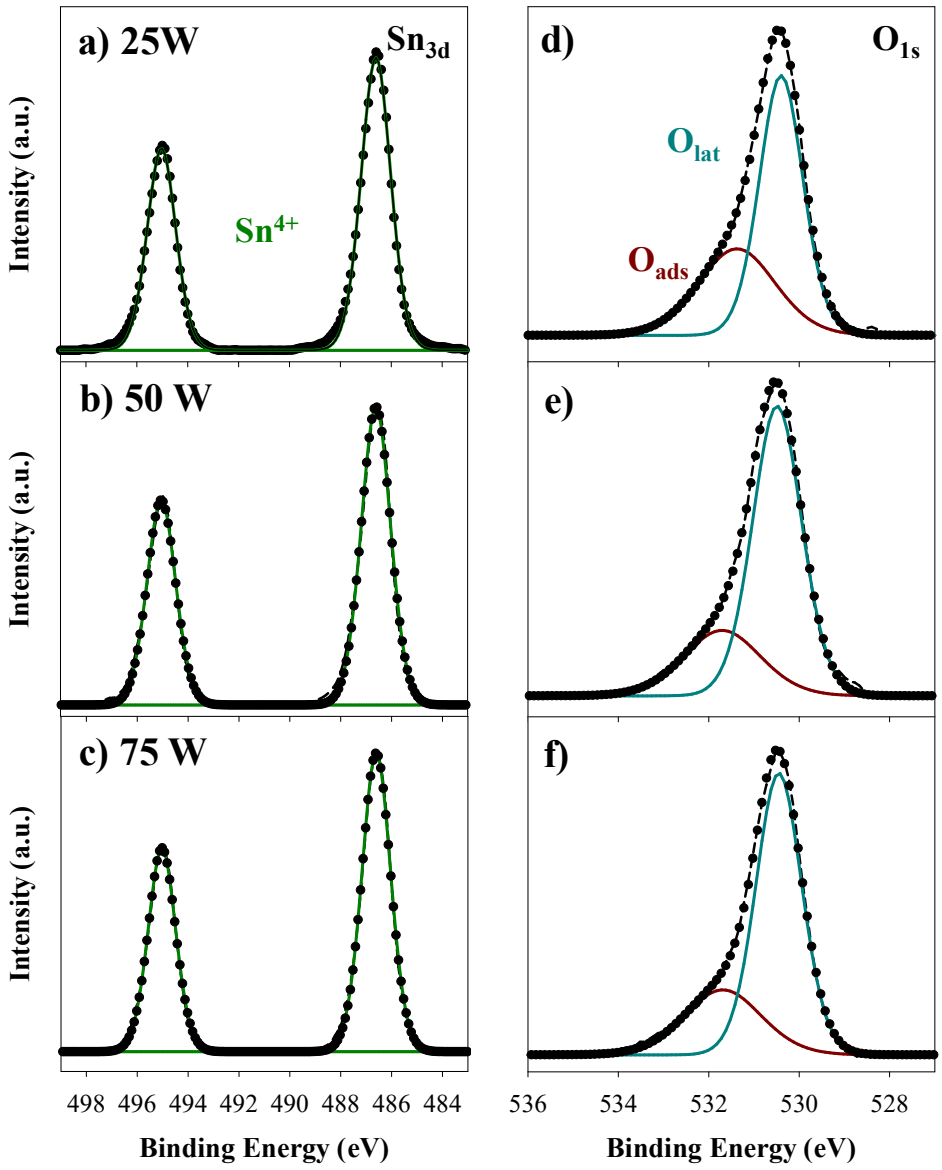

Figure 3.7. High resolution (a – c) Sn_{3d} and (d – f) O_{1s} XPS spectra of SnO_2 modified with a CO_2 plasma at (a, d) 25, (b, e) 50, and (c, f) 75 W.

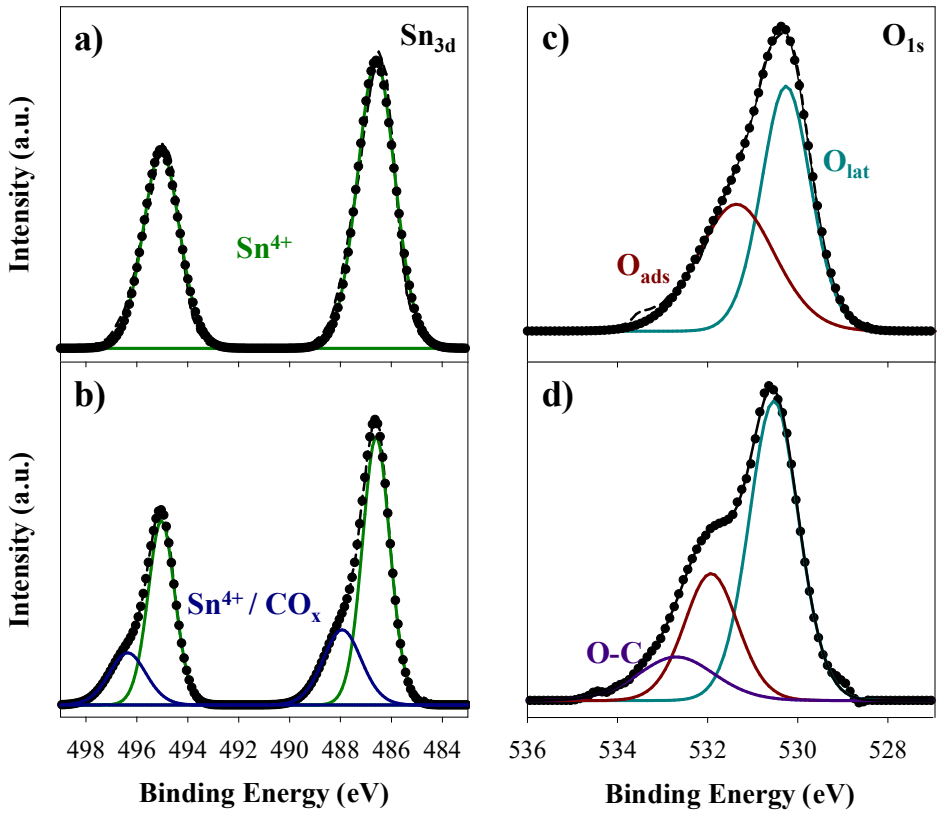

Figure 3.8. Representative (a – b) Sn_{3d} and (c – d) O_{1s} XPS high resolution spectra of SnO_2 modified with a CO_2 plasma (P = 100 W), depicting the resulting non-functionalized (a,c) and functionalized (b,d) surface. The O_{ads}/O_{lat} for all 100 W sensors is 0.57 (0.08).

that observed with the CO_2 plasma-treated polymers.

Again, the trends observed in the material characterization studies are reflected in the gas-phase OES data. At $P \leq 75$ W, the [CO] and [O] are fairly independent of P, with a much larger [O] than [CO]. Thus, even with some CO radicals present to participate in film deposition, the etching behavior of the atomic oxygen dominates enough to not only clean adventitious carbon from the SnO_2, but to also remove any plasma deposited film. Only at $P = 25$ W did the presence of an SnO_2 substrate increase [O], indicating that some of the oxygen from the material lattice was removed, becoming excited-state $O_{(g)}$ in the plasma. In addition, this was the only condition wherein Sn was detected by OES, indicating the plasma was not selectively etching O from the lattice, but rather removing both Sn and O simultaneously. Thus, the 25 W CO_2 plasma treated sensors had one of the largest increases in O_{ads}/O_{lat} compared to the UT NP. The slight increase of this ratio with the 50 W and 75 W treated sensors can be attributed to the cleaning of carbon from the SnO_2 rather than etching of the lattice. Finally, in the 100 W system, the [O] was the largest of all the parameters studied and etched the SnO_2 drastically enough such that additional functional groups could be incorporated into the material or adsorbed onto the surface post plasma exposure. Either of these processes increased the amount of O_{ads}, resulting in the largest increase of O_{ads}/O_{lat}.

For this study, the plasma modified SnO_2 substrates were tested as gas sensors to determine the effect of these treatments on device performance, as gas detection with these materials relies heavily on surface chemistry and morphology. The response of the UT SnO_2 to CO, ethanol, and benzene are shown in Figure 3.9a at a variety of T_S. As the UT sensors have the largest response to benzene at $T_S = 200$ °C, these were the conditions selected for further response and recovery studies (Fig. 3.9b). In these dynamic studies, the UT sensor showed no

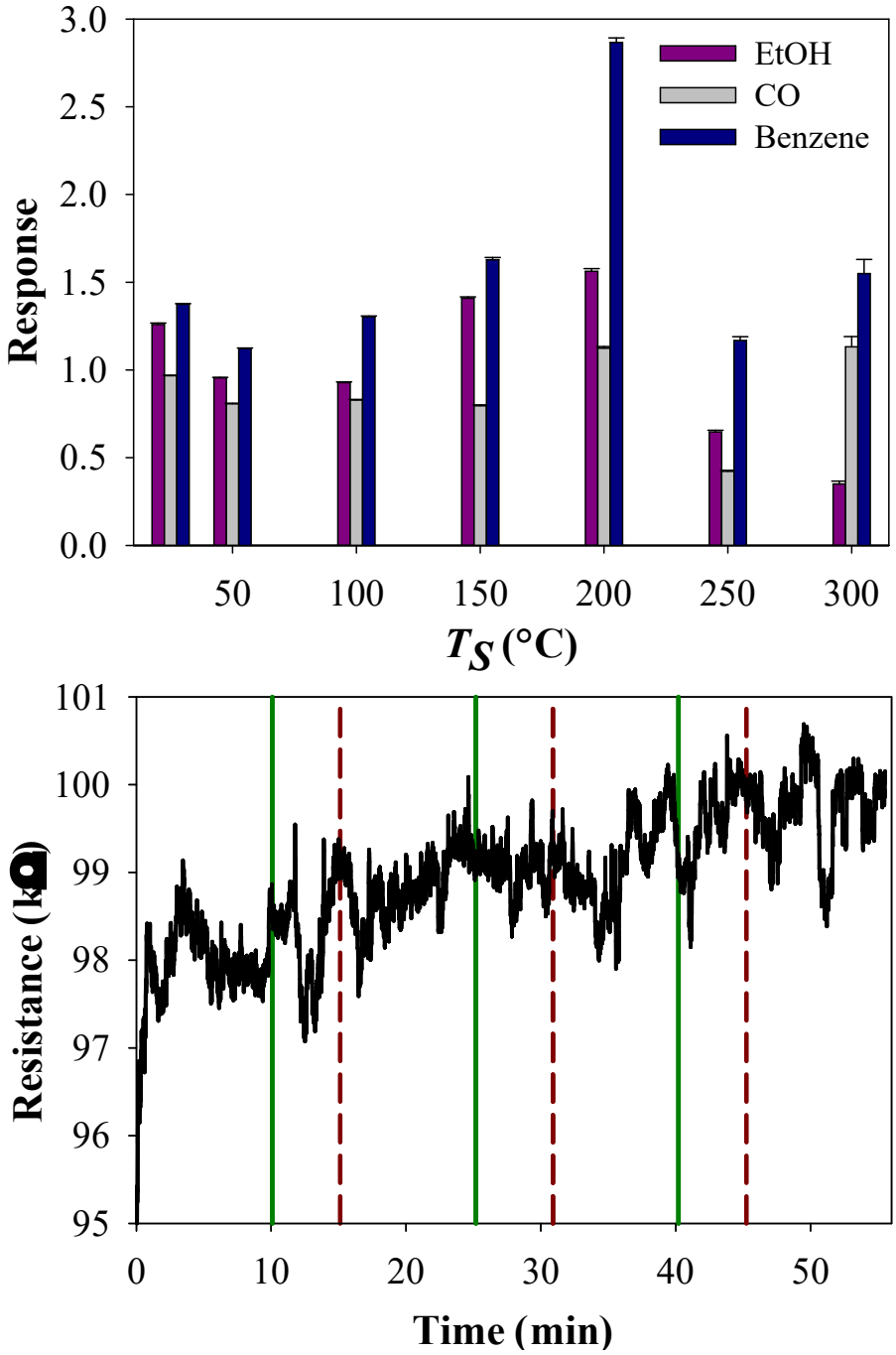

Figure 3.9. (a) Static response to ethanol, CO, and benzene and (b) benzene response and recovery behavior of the UT SnO_2 NP sensor. Response and recovery performed at T_S = 200 °C, where green solid lines and red dashed lines represent benzene flow on and off, respectively.

response when benzene gas flow was turned on (indicated by the green solid lines) or recovery behavior when benzene flow was turned off (indicated by the red dashed lines). A similar lack of response or recovery behavior of these UT sensors was also seen with the other analytes. This is consistent with previous results from our laboratory for Ar/O_2 plasma-treated SnO_2 NP sensors,[16] demonstrating that as constructed here, these UT materials are not ideal gas sensors.

Representative raw resistance plots of the CO_2 and CO plasma-treated materials are shown in Figure 3.10. With the CO_2 sensors, we observe small fluctuations in the resistance even when T_S is held constant, typical of these sensors.[18] In Figure 3.10a, the sensor clearly demonstrates the expected behavior, where the resistance decreases as T_S is increased from 25 to 300 °C in the first half of the gas exposure (from time 0 – ~93 min). As T_S is decreased back to 25 °C, the resistance returns approximately to 175 kΩ. This pattern is also seen with the other CO_2 plasma-treated sensors in air, CO, and ethanol. The CO plasma treated sensors, however, do not follow this expected behavior. For example, from ~13 to 31 min (when T_S = 50 °C) the sensor resistance increases from ~249 to ~300 kΩ, whereas typical fluctuation is ~10 kΩ. In addition, the final resistance (when T_S returns to 25 °C) is at least half that of the resistance at the start of the experiment. Both behaviors persist with the other CO modified sensors and with the other gases used in these sensing studies. These data align with XPS data that suggest surface carbon arises from a plasma deposited film, and this film prevents interactions of the analyte gas with the metal oxide surface during gas sensing experiments. Although film formation from CO plasma exposure was detrimental with SnO_2 gas sensors, this is not the case for all plasma treatments. For example, an O_2 rf plasma was used to graft polyaniline onto polyester fabric, creating a successful room temperature NH_3 gas sensor.[33] These sensors achieved a sensitivity

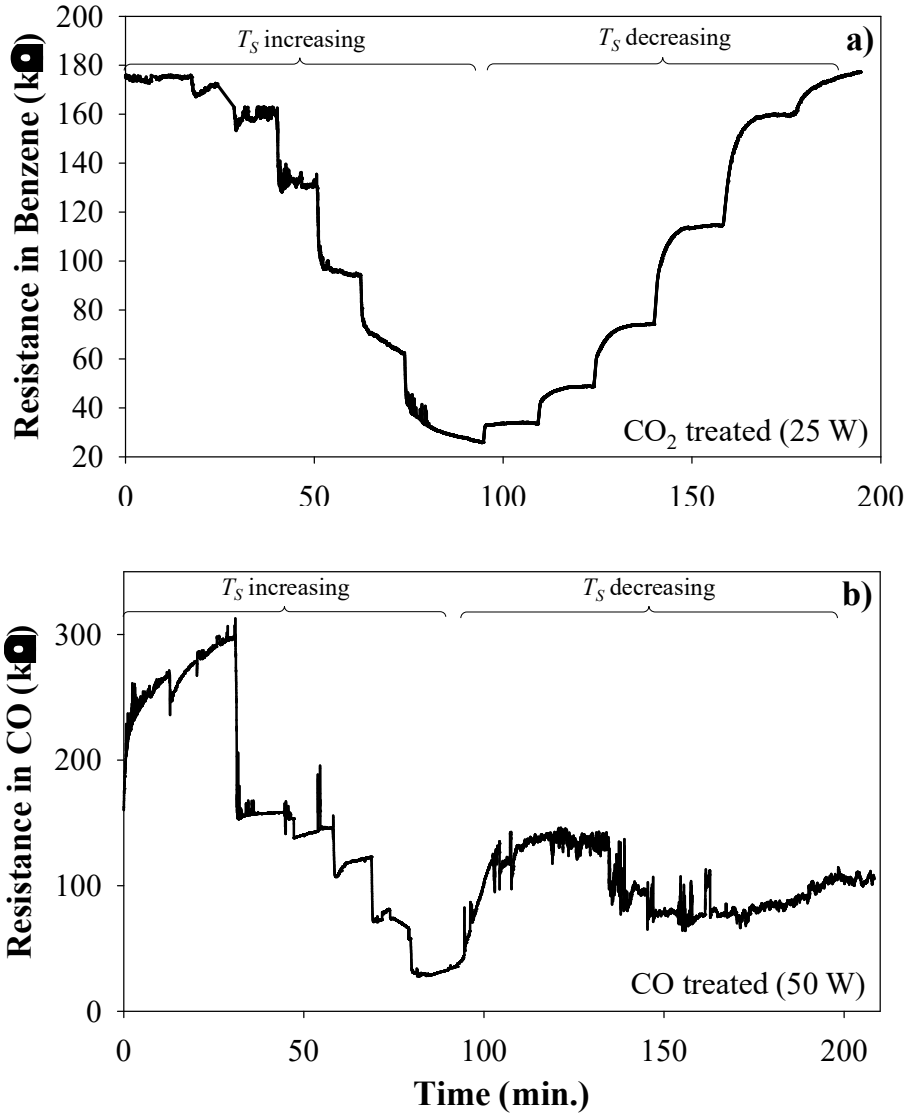

Figure 3.10. Raw resistance of (a) CO_2 (P = 25 W) and (b) CO (P = 50 W) plasma treated SnO_2 NP sensor in benzene and CO, respectively. Sensor temperature was ramped from 25 °C to 300 °C and then back to 25 °C, while the indicated gas was continually flowed over the sensor.

[(R_{gas} - R_{air})/R_{air}] of 2.49 to 40 ppm NH_3 with response and recovery times of ~126 and ~162 s, respectively.

The unstable sensor resistance in all the gases (air, CO, benzene, and ethanol) did not allow for calculation of response values for the CO plasma-treated sensors, so only the CO_2 plasma-treated sensor response values are reported (Fig. 3.11). The sensors treated with lower power plasmas (P = 25 – 75 W) demonstrated an increase in response to benzene and CO when compared to the UT sensors. The 25 W CO_2 treated sensor had the largest response to benzene of ~35 at T_S = 250 °C, followed by the 75 W treated sensor (CO response ~16 at T_S = 150 °C), and finally the 50 W treated sensor (benzene response ~6 at T_S = 150 °C). From the XPS analysis, the 25 W sensors also had the largest O_{ads}/O_{lat}, followed by the 75 W and finally 50 W sensors. These results highlight the importance of O_{ads} during gas detection and the relationship between the material surface and observed device performance. The response of the 100 W treated sensors to all the analytes is much smaller than that for the UT sensors. This indicates that the partial functionalization of this material changed the type of interaction of the analyte gas with the SnO_2 surface. Instead of all these gases interacting with the O_{ads} on the SnO_2, the gases may be adsorbing directly onto the surface of the metal oxide in an oxidizing interaction. This would result in the target gases causing a decrease in material resistance and ultimately a sensor response <1 to these gases. The switching of sensor behavior to CO and benzene was seen in previous work in our lab studying O_2/Ar and $H_2O_{(v)}$ treated SnO_2 gas sensors.[18]

Figure 3.12 shows the ethanol response and recovery behavior of a P = 25 W CO_2 plasma-treated sensor. T_S = 250 °C was used for these experiments as the static studies revealed the sensor demonstrated the largest response to ethanol and benzene at this temperature. After the first exposure, the sensor exhibits a distinct decrease in resistance; however, this decrease in

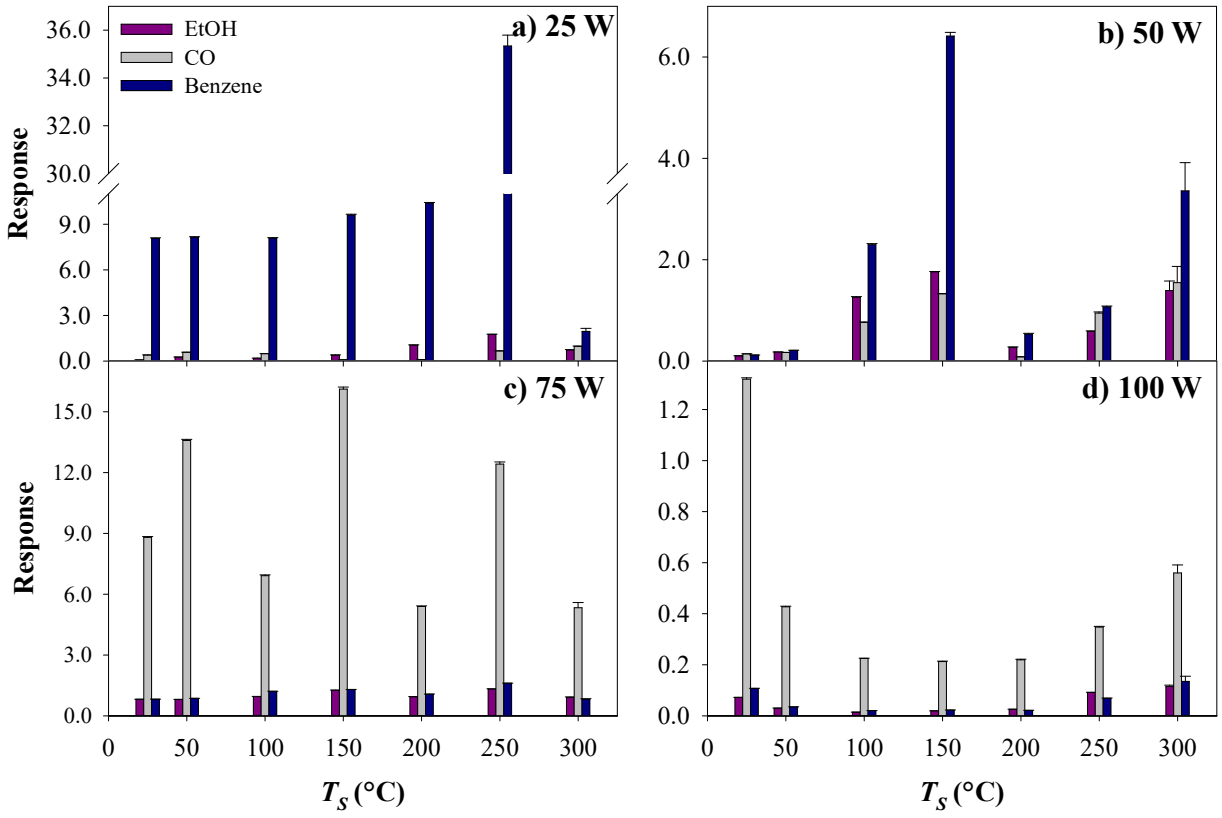

Figure 3.11. Static temperature dependent response to EtOH, CO, and benzene of SnO_2 sensors treated with a CO_2 plasma at (a) 25, (b) 50, (c) 75, and (d) 100 W. Data shown represent the weighted average response with corresponding weighted error of n = 3 samples per gas.

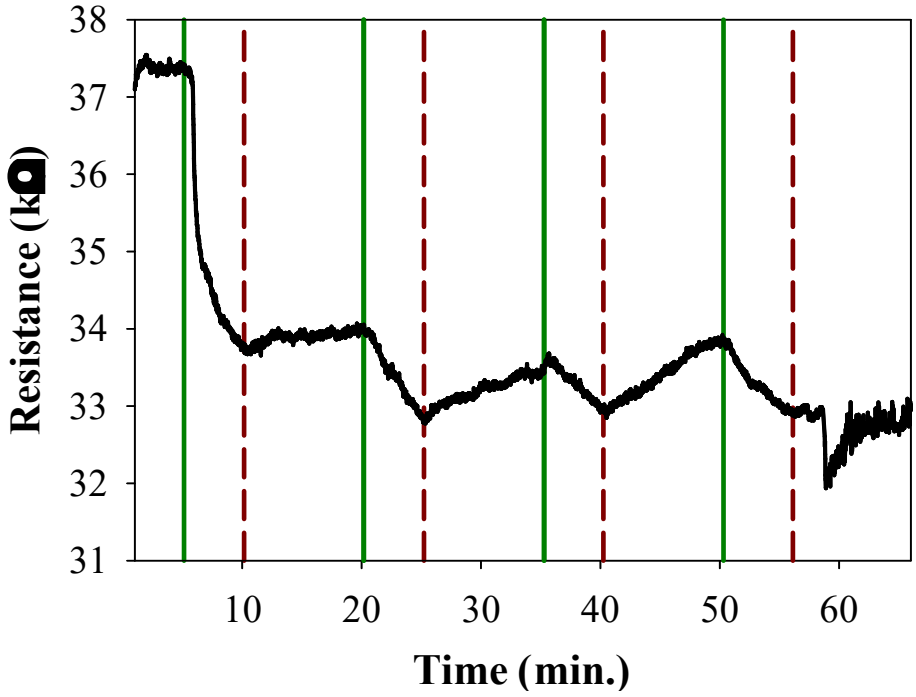

Figure 3.12. Response and recovery behavior of CO_2 plasma treated sensors (P = 25 W, T_S = 250 °C) to ethanol. Solid green and dashed red lines represent EtOH gas flow on and off, respectively.

signal gets smaller with subsequent exposures. In addition, there seems to be very little signal recovery once the ethanol flow is turned off. Note, however, that the resistance stabilizes after the first exposure, indicating that the sensor could be reused once. Subsequent ethanol exposures demonstrate that repeated use after that may result in false readings due to the instability of the sensor resistance. Recent work by Hu et al. examined the H_2 sensing performance of Ar plasma treated ZnO-SnO_2 nanofibers.[34] Similar to our work, the authors sought to improve sensor performance by etching the lattice of the metal oxides to form vacancies and ultimately increase O_{ads}. With Ar plasma treatment, they increased the response to 100 ppm H_2 from 10 to 18, lowered the T_S by 30 °C, and decreased the response time from 69 to 24 s. Also, their plasma treated sensors demonstrated good repeatability after four 500 ppm H_2 exposures. The authors do note that increasing the treatment time has an adverse effect on sensor repeatability.

Even if a direct comparison between this work and the ZnO-SnO_2 sensors cannot be made, both sensors had similar response values to their target gases. The CO_2 plasma treated sensors studied here, however, were able to achieve these results at a lower T_s than the 300 and 330 °C used with the ZnO-SnO_2 sensors. Although a 50 to 150 °C decrease in operating temperature is relatively small considering other sensors can operate at or near room temperature, this is a promising indication that CO_2 plasma modification can be used to improve the gas sensing performance of SnO_2 NP.

3.3 Summary

Plasma systems with competing deposition and etching processes are important tools for surface modification of a range of high-performance materials. Here CO and CO_2 plasma treatment of SnO_2 NP sensors were compared and evaluated as a modification strategy to improve the gas sensing performance of these devices. From OES measurements, excited state

species in both systems were similar, but additional signals from CO_2^+ and O were detected in the CO_2 plasma. Calculated relative species densities show that in general, the CO_2 plasmas have higher [O] and the CO plasmas have larger [CO], suggesting etching dominates in the former, whereas deposition dominates in the latter. From the XPS analysis of the NP, the CO plasma indeed deposited an amorphous carbon film, whereas the CO_2 plasma primarily etched the SnO_2 lattice and increased the amount of O_{ads}.

When utilizing these treated materials as a gas sensor, the film deposited on the CO modified sensors proved to be detrimental to the gas sensing process by impeding analyte-SnO_2 interaction and not allowing for calculation of sensor response to any of the selected gases. CO_2 plasma modified sensors treated at P = 25 – 75 W had much higher responses to benzene and CO compared to the UT sensors and the 25 W treated sensor demonstrated response and some recovery behavior during dynamic gas sensing studies. It should be noted, however, the 100 W CO_2 treatment resulted in nonuniform functionalization of the NP, greatly decreasing the response of these sensors compared to the UT ones. Further work with higher P CO_2 plasma treatments is needed to determine if addition of CO_x groups to the SnO_2 lattice directly results in producing oxidizing interactions with these reducing gases and a sensor response <1. Ultimately, this work identified that the etching vs deposition processes in the CO and CO_2 systems primarily depends on the behavior of the dominating species (i.e. CO or O). Perhaps more importantly, these data demonstrate that for gas sensing applications, the etching behavior of the CO_2 plasma is more desirable.

REFERENCES

1. Adamovich, I.; Baalrud, S. D.; Bogaerts, A.; Bruggeman, P. J.; Cappelli, M.; Colombo, V.; Czarnetzki, U.; Ebert, U.; Eden, J. G.; Favia, P.; Graves, D. B.; Hamaguchi, S.; Hieftje, G.; Hori, M.; Kaganovich, I. D.; Kortshagen, U.; Kushner, M. J.; Mason, N. J.; Mazouffre, S.; Thagard, S. M.; Metelmann, H. R.; Mizuno, A.; Moreau, E.; Murphy, A. B.; Niemira, B. A.; Oehrlein, G. S.; Petrovic, Z. L.; Pitchford, L. C.; Pu, Y. K.; Rauf, S.; Sakai, O.; Samukawa, S.; Starikovskaia, S.; Tennyson, J.; Terashima, K.; Turner, M. M.; van de Sanden, M. C. M.; Vardelle, A., The 2017 Plasma Roadmap: Low Temperature Plasma Science and Technology. *J. Phys. D: Appl. Phys.* **2017,** *50* (32), 323001.
2. Sahoo, G.; Polaki, S. R.; Ghosh, S.; Krishna, N. G.; Kamruddin, M.; Ostrikov, K., Plasma-Tuneable Oxygen Functionalization of Vertical Graphenes Enhance Electrochemical Capacitor Performance. *Energy Storage Mater.* **2018,** *14*, 297-305.
3. Zhao, W.; Fam, D. W. H.; Yin, Z.; Sun, T.; Tan, H. T.; Liu, W.; Tok, A. I. Y.; Boey, Y. C. F.; Zhang, H.; Hng, H. H.; Yan, Q., A Carbon Monoxide Gas Sensor Using Oxygen Plasma Modified Carbon Nanotubes. *Nanotechnology* **2012,** *23* (42), 425502.
4. Mann, M. N.; Fisher, E. R., Investigation of Antibacterial 1,8-Cineole-Derived Thin Films Formed via Plasma-Enhanced Chemical Vapor Deposition. *ACS Appl. Mater. Interfaces* **2017,** *9* (42), 36548-36560.
5. d'Agostino, R.; Cramarossa, F.; Fracassi, F.; Illuzzi, F., 2 - Plasma Polymerization of Fluorocarbons. In *Plasma Deposition, Treatment, and Etching of Polymers*, d'Agostino, R., Ed. Academic Press: San Diego, 1990; pp 95-162.
6. Hawker, M. J.; Pegalajar-Jurado, A.; Fisher, E. R., Conformal Encapsulation of Three-Dimensional, Bioresorbable Polymeric Scaffolds Using Plasma-Enhanced Chemical Vapor Deposition. *Langmuir* **2014,** *30* (41), 12328-12336.
7. Huczko, A., Plasma Decomposition of Carbon Dioxide. *AlChE J.* **1984,** *30* (5), 811-815.
8. Yasuoka, Y.; Harigai, T.; Oh, J.-S.; Furuta, H.; Hatta, A.; Suzuki, T.; Saitoh, H., Diamond-Like Carbon Films from CO Source Gas by RF Plasma CVD Method. *Jpn. J. Appl. Phys.* **2014,** *54* (1S), 01AD04.
9. Kazuomi, I.; Toshimichi, I.; Ikuo, H., Diamond Synthesis by the Microwave Plasma CVD Method Using a Mixture of Carbon Monoxide and Hydrogen Gas (I). *Chem. Lett.* **1988,** *17* (4), 589-592.
10. Mamun, M. A. A.; Furuta, H.; Hatta, A., Pulsed DC Plasma CVD System for The Deposition of DLC Films. *Mater. Today Commun.* **2018,** *14*, 40-46.
11. Hofer, L. J. E.; Sterling, E.; McCartney, J. T., Structure of Carbon Deposited from Carbon Monoxide on Iron, Cobalt and Nickel. *J. Phys. Chem.* **1955,** *59* (11), 1153-1155.
12. Liang, X.; Wang, L.; Yang, D., The Structural Evolution of Nanocrystalline Diamond Films Synthesized by r.f. PECVD. *Mater. Lett.* **2006,** *60* (6), 730-733.
13. Kwon, S. K.; Kim, K. N.; Nam, C. W.; Woo, S. I., Effect of CO and CO_2 Addition to the CF_4/O_2 Gas System on the Etching of A Low-Pressure Chemical Vapor Deposition Tungsten Film. *J. Vac. Sci. Technol., B* **1995,** *13* (3), 914-917.
14. Dey, A., Semiconductor Metal Oxide Gas Sensors: A Review. *Mater. Sci. Eng., B* **2018,** *229*, 206-217.
15. Ihokura, K.; Watson, J., *The Stannic Oxide Gas Sensor: Principles and Applications*. CRC Press: Boca Raton, 1994.

16. Hiyoto, K. A. M.; Fisher, E. R., Utilizing Plasma Modified SnO_2 Paper Gas Sensors to Better Understand Gas-Surface Interactions at Low Temperatures. *J. Vac. Sci. Technol., A* **2020,** *38* (4), 043202.
17. Stuckert, E. P.; Fisher, E. R., Ar/O_2 and H_2O Plasma Surface Modification of SnO_2 Nanomaterials to Increase Surface Oxidation. *Sens. Actuators B* **2015,** *208*, 379-388.
18. Stuckert, E. P.; Miller, C. J.; Fisher, E. R., The Effect of Ar/O_2 and H_2O Plasma Treatment of SnO_2 Nanoparticles and Nanowires on Carbon Monoxide and Benzene Detection. *ACS Appl. Mater. Interfaces* **2017,** *9* (18), 15733-15743.
19. Stuckert, E. P.; Miller, C. J.; Fisher, E. R., Gas-phase diagnostics during H_2 and H_2O plasma treatment of SnO_2 nanomaterials: Implications for surface modification. *J. Vac. Sci. Technol., B* **2017,** *35* (2), 021802.
20. Spencer, L. F.; Gallimore, A. D., Efficiency of CO_2 Dissociation in a Radio-Frequency Discharge. *Plasma Chem. Plasma Process.* **2011,** *31* (1), 79-89.
21. George, A.; Shen, B.; Craven, M.; Wang, Y.; Kang, D.; Wu, C.; Tu, X., A Review of Non-Thermal Plasma Technology: A Novel Solution for CO_2 Conversion and Utilization. *Renew. Sustain. Energy Rev.* **2021,** *135*, 109702.
22. Morillo-Candas, A. S.; Guerra, V.; Guaitella, O., Time Evolution of the Dissociation Fraction in RF CO_2 Plasmas: Impact and Nature of Back-Reaction Mechanisms. *J. Phys. Chem. C* **2020,** *124* (32), 17459-17475.
23. Reyes, P. G.; Mendez, E. F.; Osorio-Gonzalez, D.; Castillo, F.; Martínez, H., Optical emission spectroscopy of CO_2 glow discharge at low pressure. *Phys. Status Solidi C* **2008,** *5* (4), 907-910.
24. Huang, Q.; Zhang, D.; Wang, D.; Liu, K.; Kleyn, A. W., Carbon Dioxide Dissociation in Non-Thermal Radiofrequency and Microwave Plasma. *J. Phys. D: Appl. Phys.* **2017,** *50* (29), 294001.
25. Pearse, R. W. B.; Gaydon, A. G., *Identification of Molecular Spectra*. Chapman and Hall: 1976.
26. Geiger, R.; Staack, D., Analysis of Solid Products Formed in Atmospheric Non-Thermal Carbon Monoxide Plasma. *J. Phys. D: Appl. Phys.* **2011,** *44* (27), 274005.
27. Pulsipher, D. J. V.; Fisher, E. R., O_2 Plasma Treatment of Mesoporous And Compact TiO_2 Photovoltaic Films: Revealing and Eliminating Effects Of Si Incorporation. *Surf. Coat. Technol.* **2009,** *203* (16), 2236-2242.
28. Yu, H.-Y.; Xie, Y.-J.; Hu, M.-X.; Wang, J.-L.; Wang, S.-Y.; Xu, Z.-K., Surface Modification of Polypropylene Microporous Membrane to Improve Its Antifouling Property in MBR: CO_2 Plasma Treatment. *J. Membr. Sci.* **2005,** *254* (1), 219-227.
29. Wavhal, D. S.; Fisher, E. R., Modification of Polysulfone Ultrafiltration Membranes By CO_2 Plasma Treatments. *Desalination* **2005,** *172* (2), 189-205.
30. Tompkins, B. D.; Dennison, J. M.; Fisher, E. R., Etching and Post-Treatment Surface Stability of Track-Etched Polycarbonate Membranes by Plasma Processing Using Various Related Oxidizing Plasma Systems. *Plasma Process. Polym.* **2014,** *11* (9), 850-863.
31. Gancarz, I.; Poźniak, G.; Bryjak, M., Modification of Polysulfone Membranes 1. CO_2 Plasma Treatment. *Eur. Polym. J.* **1999,** *35* (8), 1419-1428.
32. *Lange's Handbook of Chemistry*. 15th ed.; McGraw-Hill Education: New York, 1999.
33. Nimbekar, A. A.; Deshmukh, R. R., Plasma-Induced Grafting of Polyaniline on Polyester Fabric for Gas Sensing Application. *J. Mater. Sci.: Mater. Electron.* **2021,** *32* (1), 59-72.

34. Hu, K.; Wang, F.; Shen, Z.; Liu, H.; Zeng, W.; Wang, Y., Ar Plasma Treatment on ZnO–SnO_2 Heterojunction Nanofibers and Its Enhancement Mechanism of Hydrogen Gas Sensing. *Ceram. Int.* **2020,** *46* (13), 21439-21447.

CHAPTER 4

UTILIZING PLASMA MODIFIED SNO_2 PAPER GAS SENSORS TO BETTER UNDERSTAND GAS-SURFACE INTERACTIONS AT LOW TEMPERATURES[1]

This chapter describes the gas sensing performance of O_2/Ar plasma modified SnO_2 NP paper gas sensors. In addition, the adaptation of the existing sensing chamber to do real-time response and recovery gas sensing and analysis of these data were established in this work. This work was financially supported by the National Science Foundation (NSF CBET – 1803067) and I would like to thank Dr. Erin Stuckert, Dr. Charles Henry, and Dr. Alyssa Kava for helpful discussions as well as the staff of the CSU Central Instrument Facility for assistance with the materials characterization data.

4.1 Introduction

To obtain a more complete understanding of the air quality in a variety of places, people are turning toward a larger number of cheaper portable gas sensors to compliment traditional air quality monitoring stations.[1-3] Projects like "CitiSense" utilize several small electrochemical sensors interfaced to a cellphone to collect real-time levels of carbon monoxide, nitric oxide, and ozone.[4] Although electrochemical sensors are widely used in commercial devices, semiconducting metal oxides (SMO) are a more desirable choice because they are generally lower cost, have a higher sensitivity, and shorter response time.[5-6] This increased sensing

[1] [1]Reproduced from K. A. M. Hiyoto and E. R. Fisher, *J. Vac. Sci. Technol., A.* **38,** 043202 (2020), with the permission of AIP Publishing.

performance largely results from the sensing mechanism that these materials employ to detect gases. Upon exposure to atmosphere, oxygen adsorbs onto the surface of the SMO (reaction 1) and then forms an oxygen anion layer via reactions 2 or 3:[7-8]

$$O_{2(g)} \rightleftharpoons O_{2(ads)} \quad (1)$$

$$O_{2(ads)} + e^- \rightleftharpoons O_2^-{}_{(ads)} \quad (2)$$

$$O_{2(ads)} + 2e^- \rightleftharpoons 2O^-_{(ads)} \quad (3)$$

The speciation of the adsorbed oxygen is dependent on SMO temperature. For example, with SnO_2, reactions 2 and 3 occur at ≥150 and ≥300 °C, respectively.[9-10] The formation of this ionosorbed layer also creates a corresponding depletion layer within the material, resulting in an increase in resistance. Along with this oxidizing interaction, gases can also have a reducing interaction with the SMO by reacting with the adsorbed oxygen, releasing the electrons back into the material, thus decreasing the resistance. These changes in resistance (either oxidizing or reducing) can be used to determine not only the type of gas being detected but can also be correlated to analyte concentration. Therefore, the speciation (and ultimately reactivity) of the ionosorbed layer plays a crucial role in effectively detecting gases, which is why SMO devices require a sensor operating temperature (T_s) ≥300 °C to have a large sensitivity to many gases. This, however, results in practical challenges that outweigh the performance benefits of using SMO. Thus, at-or-near room temperature gas sensing is a required element of expanding the types of materials available for portable gas sensors.

When optimizing device design for portable sensors, often changing the supporting substrate within the device is ignored in favor of improving material characteristics. An inexpensive alternative (paper) to traditional substrates (ceramic or metal oxide wafers) decreases the device production cost dramatically. Furthermore, the naturally porous

morphology has the added benefit of increasing the amount of accessible SMO when compared to a flat substrate. One such sensor used ZnO nanoparticles (NP) with pencil-drawn electrodes on paper.[11-12] Although this study focused on proof-of-concept, it did assess preliminary performance by exploring O_2 sensing with pulsed or continuous UV light stimulus. As the use of a pulsed UV stimulus to improve sensing performance was the primary goal of that study, characteristics such as O_2 response and recovery behavior as well as sensitivity to other gases were not reported. As discussed above, when considering practical characteristics of a device, a paper-based gas sensor (PGS) will require the T_S of the SMO to be drastically lowered to <140 °C.

Low-temperature inductively coupled plasma (LT-ICP) processing offers a desirable strategy to potentially improving the performance of SMO gas sensors by altering the surface of the material to promote target gas-SMO interactions.[13-14] The large parameter space of LT-ICP modification results in high flexibility during plasma treatment. Our laboratory has demonstrated the ability to modify the entire device (substrate and SMO)[15-16] or only the SMO,[17] further expanding the tunability of this process. Note that combining the morphologically complex PGS and plasma modification also requires the ability to modify the SMO throughout the substrate matrix. We have effectively treated a range of complex 3D substrates, such as polymer membranes[18-19] and scaffolds,[20] utilizing both functional group implantation and thin film deposition throughout the porous substrate. Thus, LTP-ICP treatment can create uniformly modified materials, regardless of the morphological complexity of the substrate. This strategy also provides the unique opportunity to maintain bulk characteristics of the SMO while altering the surface chemistry. Thus, these devices can then be tested to elucidate the relationship between surface chemistry and gas-SMO interactions. Understanding both how the plasma

changes the SMO and the underlying mechanism of gas detection ultimately allow for a targeted approach to optimizing the surface modification process and ultimately creating better gas sensors.

4.2 Results and Discussion

The effectiveness of the fabrication method was first assessed using EDS and SEM. Representative elemental maps, Fig. 4.1b – d, confirm the expected presence of Sn, O, and C. In Fig. 4.1a, the edge of the dropcast solutions can be seen in the lower left corner and the absence of Sn in Fig. 4.1b in the same spot indicates that the only source of Sn is from the NP solution. It should also be noted that the Sn appears to be uniformly distributed on both the electrodes and the paper substrate. Additionally, Cl was also detected on some samples and mostly concentrated on the electrodes, indicating that it is likely from the carbon ink in the electrodes and not a contaminate from the process of applying the NP to the PGSs. Even after plasma treatment at the harshest condition investigated (p = 140 mTorr, P = 60 W), Fig. 4.2e – f, the substrate and NP attachment to the substrate appear to be unchanged from the images shown in Fig. 4.2a – b and c – d, respectively. Thus, although simple, this process of drop casting NP and then plasma treating the PGS is an effective method to fabricating these devices.

XPS elemental composition data for the UT and plasma treated (p = 140 mTorr, P = 60 W) PGS are provided in Table 4.1 and do not change appreciably from sensor to sensor, with significant contributions coming from Sn, O, and C, as expected. Sample spots were carefully selected so that they were located between the carbon paste electrodes as the modification of the SnO_2 NP was the focus of this study. This also helps to avoid detection of Cl arising from the carbon paste during analysis. Figure 4.3 shows representative high resolution XPS spectra for an UT and newly treated PGS along with those for an aged, treated PGS. The aged PGS was

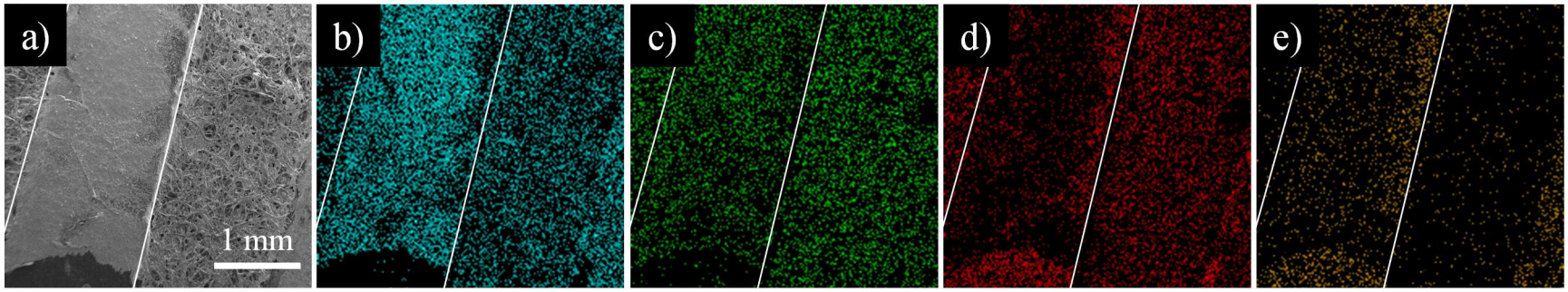

Figure 4.1. SEM (a) and EDS elemental composition maps of Sn (b), O (c), C (d), and Cl (e) of untreated PGS at x25 magnification. The white diagonal lines denote the edges of the electrode.

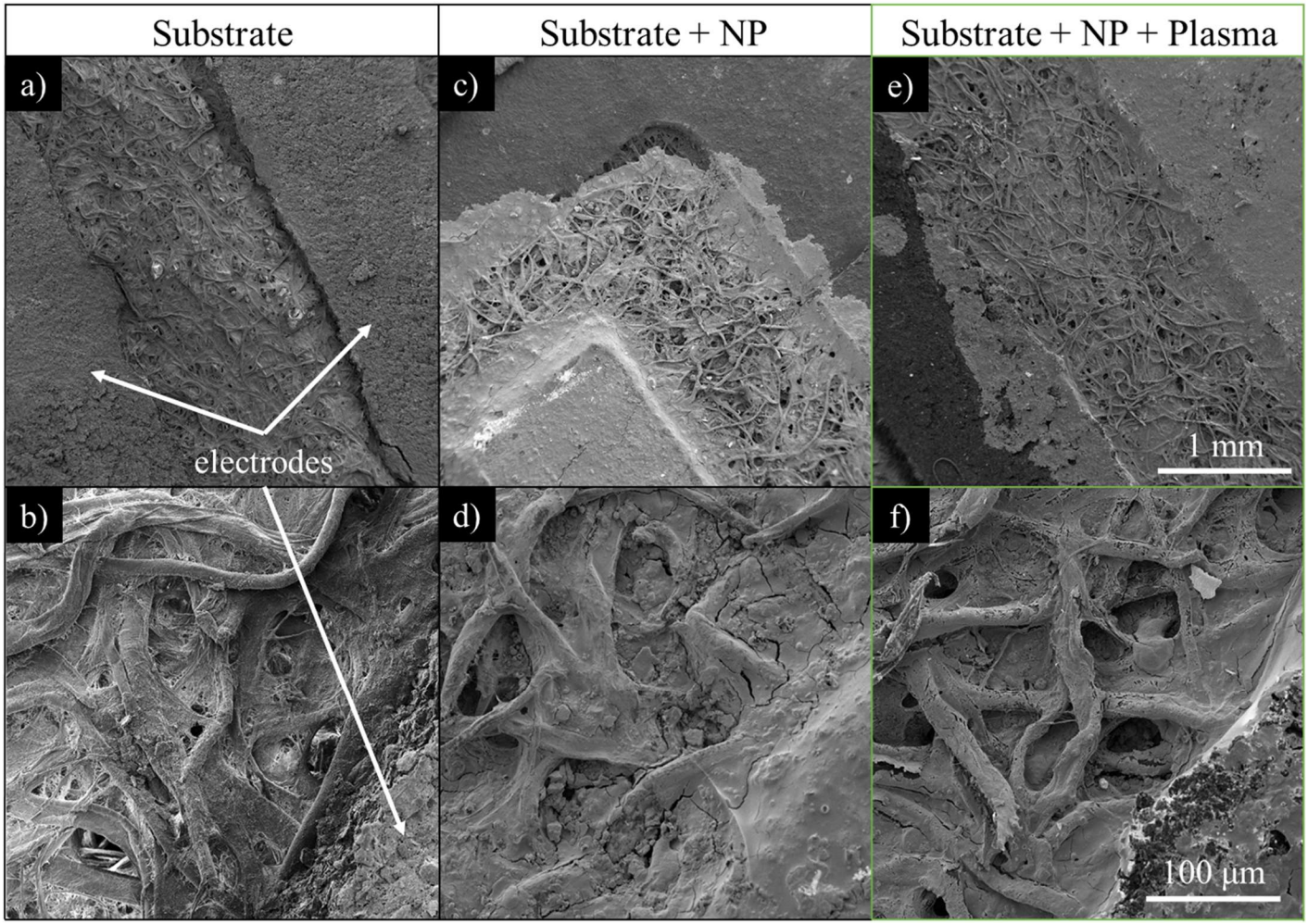

Figure 4.2. SEM images of hybrid sensors at various steps in the fabrication process: (a, b) carbon paste electrodes on paper substrate; (c, d) with NP drop cast onto the electrode/paper substrate (untreated); and (e, f) after plasma treatment (p = 140 mTorr, P = 60 W) of NP/paper sensors. Magnifications are x25 (a, c, e) and x250 (b, d, f)

analyzed immediately after performing dynamic response/recovery experiments to ensure that the gas sensing performance of the device was similar to that of the freshly treated PGS, indicating that the efficacy of the treatment was not lost. For all three types of sensors, the Sn_{3d} high resolution spectra look virtually identical, displaying two peaks attributable to the expected spin-orbit splitting for Sn^{4+}.

The Table 4.1 elemental composition data show the carbon content is virtually the same before and after plasma treatment, primarily because the largest source of carbon is the paper substrate used in the PGS devices. The C_{1s} high resolution spectra for the three devices, however, reveal significant differences in the carbon binding environments, Fig. 4.3b. Each material contains the same three binding environments attributable to -C-C/C-H (284.8 eV), -C-O (~286.2 eV) and O-C-O (~ 288.9eV).[21] The relative concentrations of these binding environments, however, change dramatically between the three sensor types. Notably, the primary difference is that the amount of carbon in the O-C-O binding environment in the freshly treated sensor (~36%) is more than double that in both the UT PGS (~13%) and the aged PGS (~13%). Similarly, the O_{1s} spectra display perhaps the most significant changes in that the amount of adsorbed oxygen (~532.2 eV, O_{ads}) relative to lattice oxygen (~531.3 eV, O_{lat}) changes dramatically between the UT PGSs and newly treated PGS.[16, 22-23] Specifically, the plasma treated PGS has more adsorbed oxygen than the UT PGS, indicated by a lower ratio of percent lattice to percent adsorbed oxygen. This is consistent with other reports of plasma modified SMOs.[13-14, 16] This increase is typically attributed to the plasma etching the surface of the material lattice, generating oxygen vacancies and ultimately promoting oxygen adsorption, which is a vital step during gas sensing. Overall, the XPS high resolution spectra clearly indicate

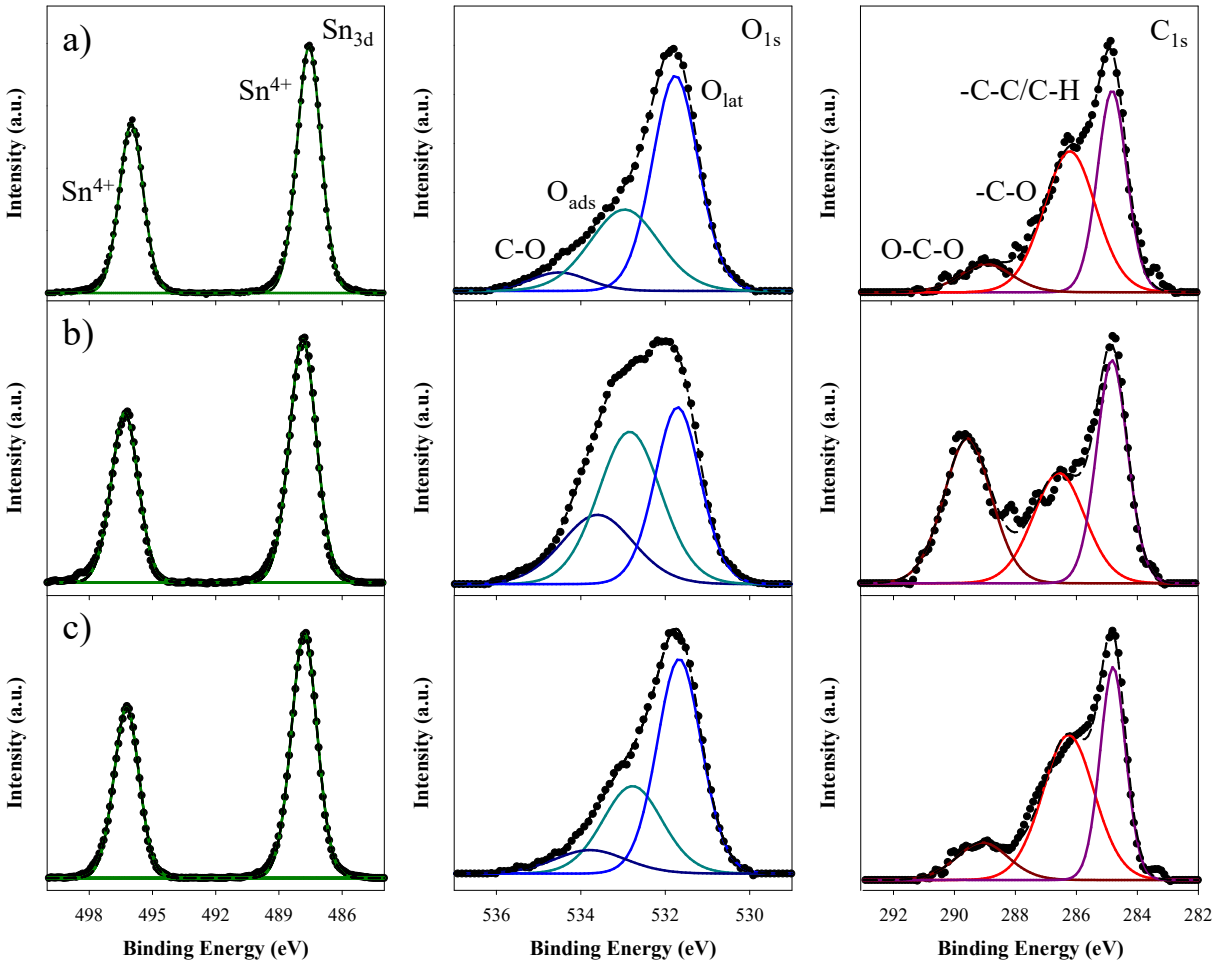

Figure 4.3. High resolution Sn_{3d} (left), O_{1s} (middle), and C_{1s} (right) XPS spectra of the (a) UT and (b-c) plasma treated PGS (p = 140 mTorr, P = 60 W). The plasma treated sensors were analyzed (b) 1 day and (c) 9 months after treatment. Individual peak labels correspond to fitted binding environments.

Table 4.1. Elemental composition (percent C, Sn, and O) and ratio of lattice to adsorbed oxygen of UT and 60 W treated (new and aged) PGS[a]

		C (%)	Sn (%)	O (%)	O_{lat}/O_{ads}[b]
UT		24.6 (8.6)	30.1 (4.2)	45.3 (4.4)	3.17 (1.97)
60 W Treated PGS	New	26.9 (8.7)	23.8 (5.7)	49.3 (3.0)	1.33 (0.34)
	Aged	20.7 (7.4)	32.3 (4.1)	48.0 (3.3)	2.64 (1.29)

[a]Values in parenthesis represent the calculated standard deviation from the mean of n≥3. For the treated PGS, data shown are for both a newly treated device and one that had been aged 9 months.

[b]Ratio of the relative percentages of oxygen attributed to lattice oxygen (O_{lat}) relative to that attributed to adsorbed oxygen (O_{ads}) in the O_{1s} envelope.

the plasma treatment oxidizes the surface of the substrate, but that over time some of this surface oxidation degrades.

To better understand the mechanism of plasma modification of the PGSs, we utilized OES both with and without the sensor in the plasma. Representative raw spectra (p = 140 mTorr, P = 60 W) are shown in Fig. 4.4a. As expected from the precursor gas, peaks associated with excited state oxygen and argon can be seen in all spectra collected (p = 140 mTorr, P = 15 – 60 W). With the addition of a PGS to the plasma, peaks from excited state hydrogen emerge. Using rare gas actinometry,[24-25] the relative species densities of H_α and $O(^3P)$ can be seen in Fig. 4.4b – c. The presence of H_α and the increase in species density with P, indicates that the paper substrate is being etched during plasma treatment, as the paper is the only source of hydrogen in the system. In Fig. 4.4c, the addition of a PGS to the plasma also resulted in an increased amount of excited state oxygen. Because of the multiple sources of oxygen (i.e. the paper, NP, and the feed gas), less can be directly known about how the plasma is interacting with the PGSs. The origin of the additional gas-phase oxygen is important because etching systems like Ar/O_2 plasmas have been shown to remove oxygen from the SnO_2 lattice.[13] The etching action increases the amount of oxygen vacancies in the SnO_2 lattice, thereby increasing the amount of adsorbed oxygen, and allowing the formation of the oxygen anion layer at lower temperatures. These surface changes are what is thought to be source of the increased response to target gases and lowering the T_s.[13-15] Pan *et al.* also attributed their improved sensor performance to the increased surface area of the SnO_2 nanowires after being etched by the plasma (P = 40 and 80 W).[13] Thus, the desired result of creating oxygen vacancies via plasma treatment, validated by the XPS data shown in Fig. 4.3, could be a possible source of the observed additional gas-phase oxygen in the plasma. Additional support for this hypothesis comes from earlier observations in

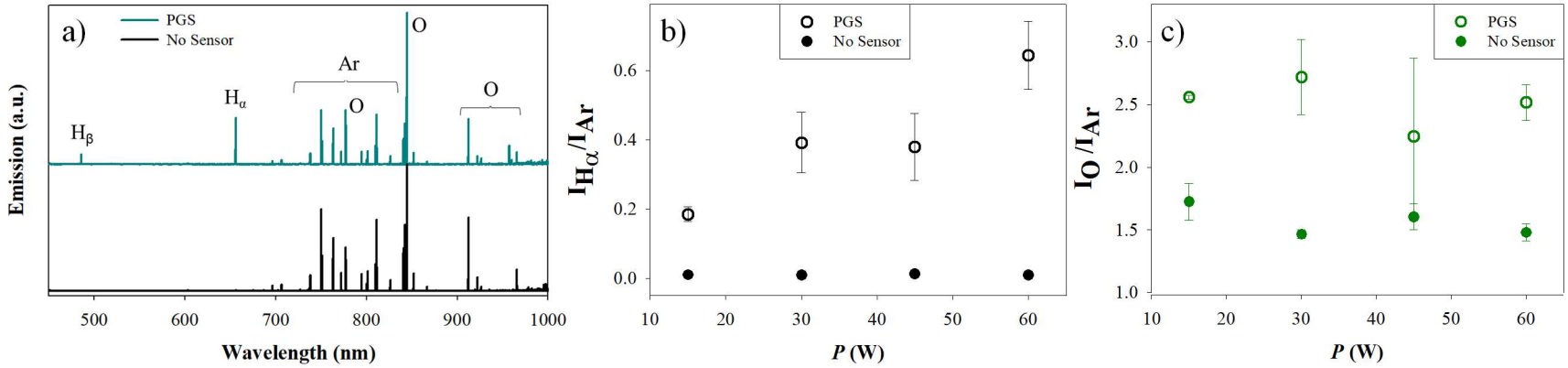

Figure 4.4. Raw OES spectra from 450 – 1000 nm (a) for Ar/O_2 plasma treatment (p = 140 mTorr, P = 60 W) with and without the PGS. Peaks are labeled with associated excited state species. Relative excited state H_α (b) and O (c) densities as a function of applied plasma power in an Ar/O_2 plasma with (open circles) and without (closed circles) PGS.

our laboratory using a 100% H_2 plasma and SnO_2 NP on ZrO_2 wafer substrates.[24] Similar to our system, there are still multiple sources of oxygen; however, excited state OH radicals were formed in the gas phase only when SnO_2 was present in the plasma. Moreover, the simultaneous formation of Sn atoms in the gas-phase detected by OES was a clear indicator of NP etching.

To determine if the current treatments improved gas sensor performance, we attempted to collect sensing measurements with the UT PGSs. Unfortunately, the resistance of the UT PGSs was too large to be quantified. As such, we chose to use a standard substrate (ZrO_2 wafer) to support the NP for the control device (referred to as "UT sensor", henceforth, to distinguish it from the UT PGS), fabricated using a method previously described.[16] The UT sensor had response ≈ 1 for all target gases at all T_S tested, as shown in Fig. 4.5. This suggests the UT sensor is relatively inert as a sensing material at the low sensor temperatures examined. This lack of response is expected because the low T_S cannot drive the formation reaction for ionosorbed oxygen with which the target gases can interact.[5, 9, 26]

The T_S dependent response of the plasma-treated PGS (p = 140 mTorr, P = 15 – 60 W) when exposed to EtOH, CO, and benzene is shown in Fig. 4.6. Note that unlike the UT PGS, these plasma-treated PGSs had a measurable resistance, allowing gas-sensing studies to be performed. This could be the result of activation of the carbon paste electrodes with the plasma treatment creating a more conductive substrate. Similar electrode improvement was seen by Wang *et al.* when treating their carbon paste electrodes with a O_2 plasma.[27] The 15 W treated PGS had the largest response to both EtOH (Response = 65.99 ± 0.35) and benzene (Response = 15.14 ± 0.05) at T_S = 50 °C. SMO sensors typically have a higher response to EtOH than benzene and CO; thus, the mildest treatment would be the most likely to behave similarly to

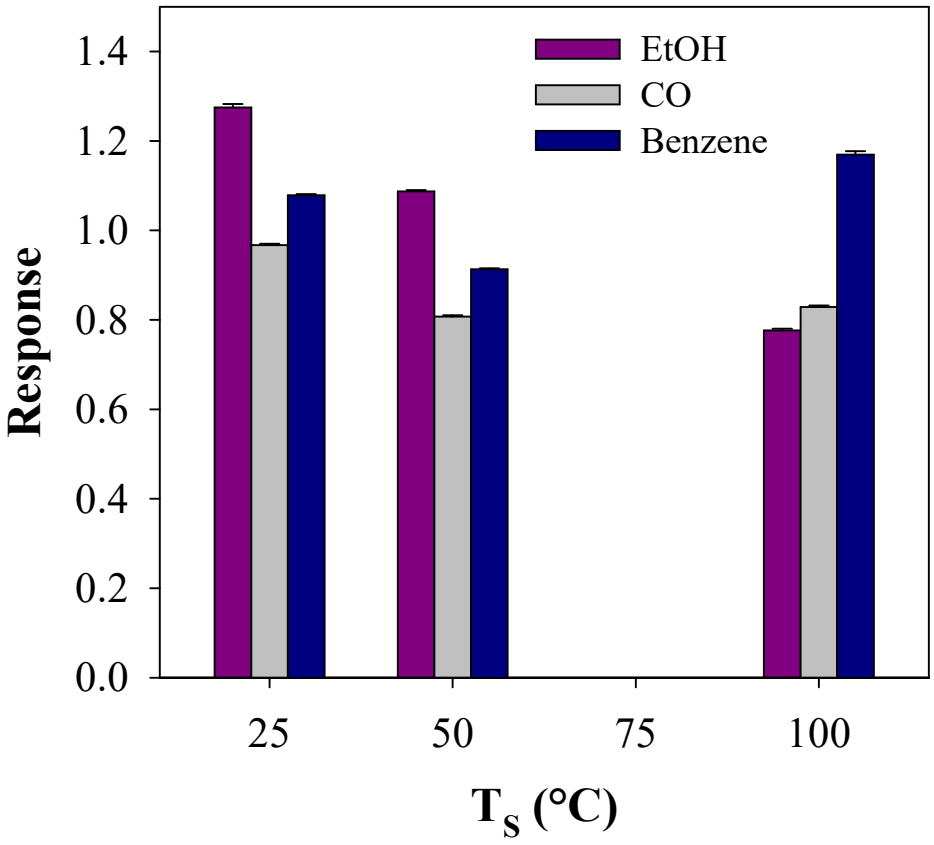

Figure 4.5. Temperature dependent response to ethanol$_{(v)}$, 100 ppm CO, and 100 ppm benzene of the UT sensor as a function of T_S. Calculated weighted error is ≤0.66% of response where not visible.

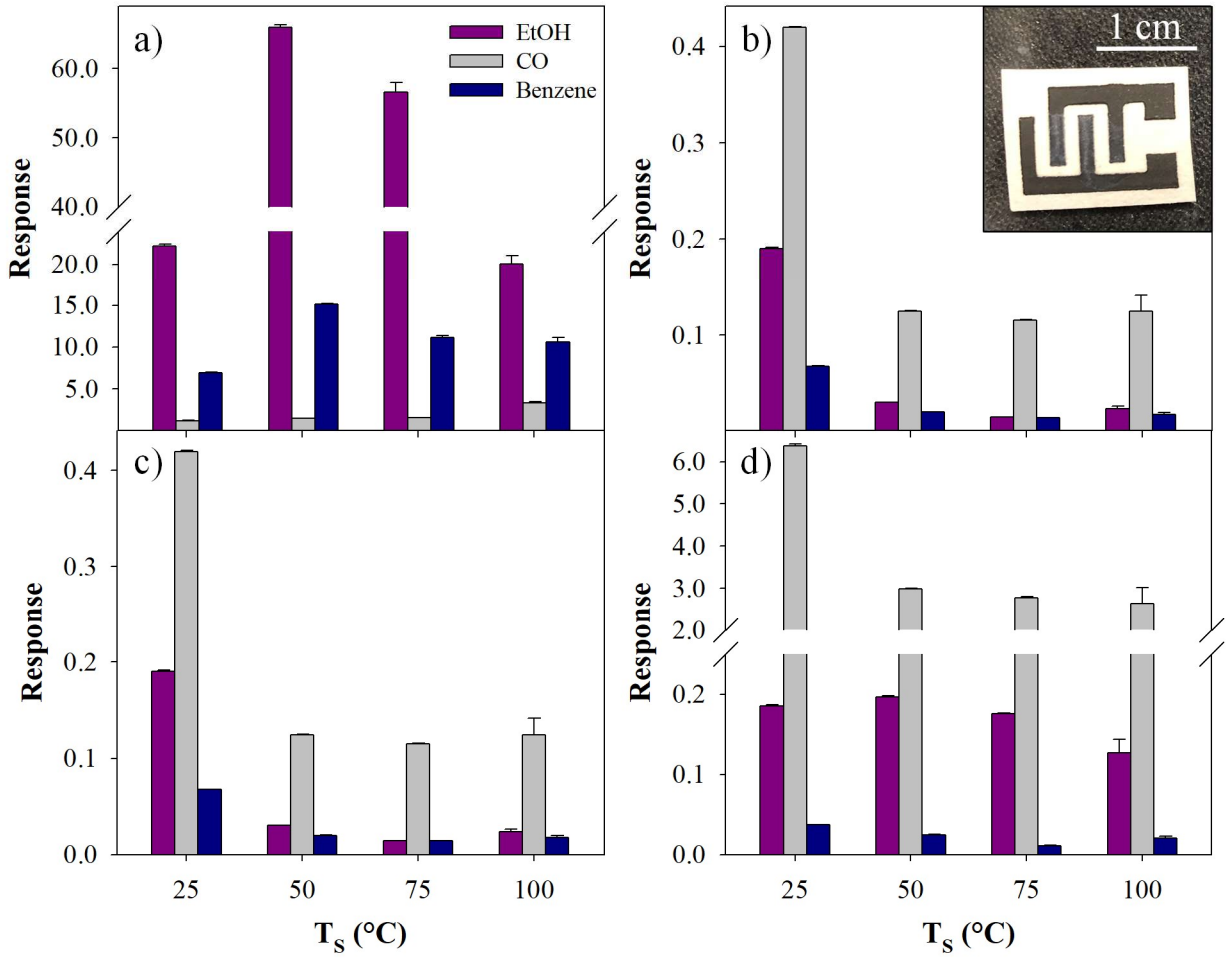

Figure 4.6. Temperature dependent response to ethanol$_{(v)}$, 100 ppm CO, and 100 ppm benzene of PGS devices plasma treated at 15 (a), 30 (b), 45 (c), or 60 W (d) applied rf power with p = 140 mTorr. Inset shows photograph of the PGS with NP after plasma treatment. Calculated weighted error is ≤2.40% of response where not visible.

native SMO.[26] The PGS treated in a 60 W plasma had the largest response to CO (6.37 ± 0.05) at T_S = 25 °C, decreasing to ≈ 3 at T_S≥50 °C. Notably, devices treated at other *P* had responses essentially the same as those for the control device, regardless of T_S. The distinguishable responses to the different gases are a promising indication that the selectivity of the PGS can be tuned by changing plasma treatment parameters, further improving the performance of this device. In addition, the optimal operating T_s for all target gases is ≤50 °C, which is much lower than previously reported SMO sensors, where optimal temperatures often exceed 300 °C.

Based on the T_S dependent response, the PGSs with the largest response to all target gases were selected for further study. The response and recovery behavior toward benzene and CO for the 15 and 60 W treated sensors, respectively, can be seen in Fig. 4.7. It should be noted that these response and recovery studies were collected as preliminary results to demonstrate the applicability of these novel sensors for real-time gas detection, and clearly indicate the need for further optimization of this home-built system for these types of experiments. From the T_S dependent response, even the largest response to both benzene and CO is much lower than that of EtOH (25% and 10%, respectively), so further work looking at this aspect of sensor performance was done using EtOH as the target gas to best understand the maximum capabilities of these plasma modified PGS. In addition, SMO sensors typically display a higher response to EtOH than to the other target gases,[26] further validating this choice to use EtOH as the primary focus of these preliminary studies. The lack of observable response and recovery behavior of the UT sensor at T_S = 25 °C can be seen in Fig. 4.8a. Although there appears to be some initial response to EtOH exposure, this behavior does not persist with subsequent exposures, so no response or recovery times were calculated. This indicates that when first exposed to EtOH,

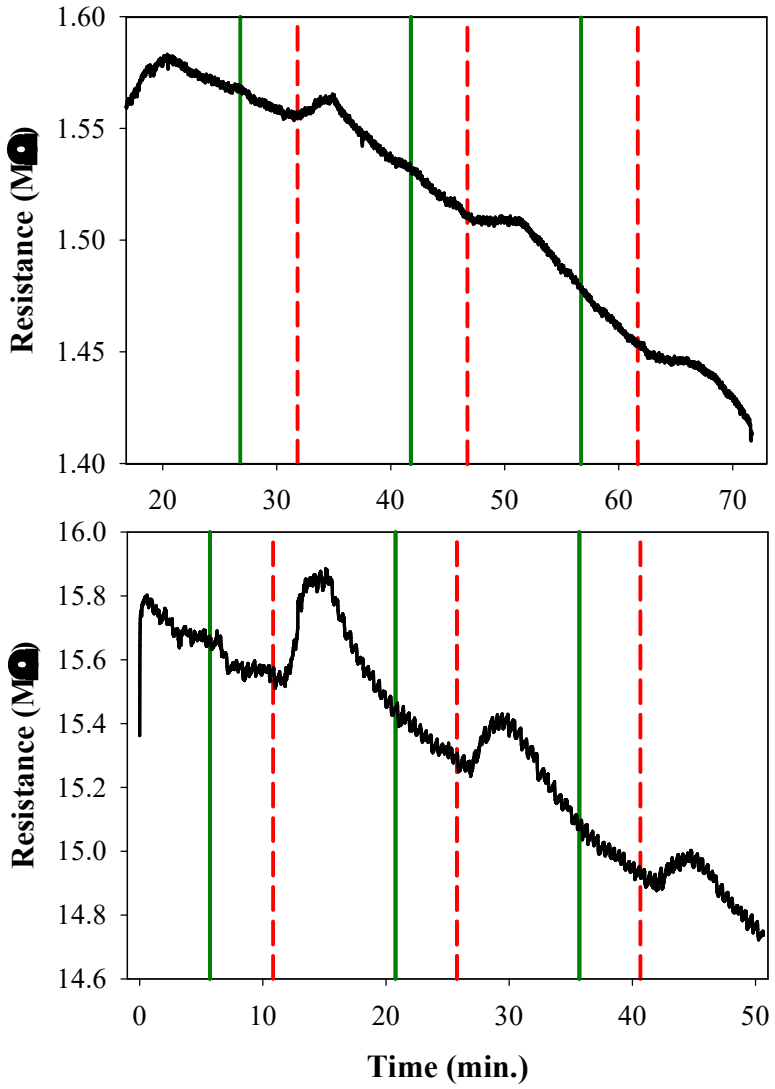

Figure 4.7. Response and recovery behavior of (top) 15 W PGS to benzene at T_S = 50 °C and (bottom) 60 W PGS to CO at T_S = 25 °C. Solid (green) lines indicate target gas flow on for the and dashed (red) lines indicate gas flow off.

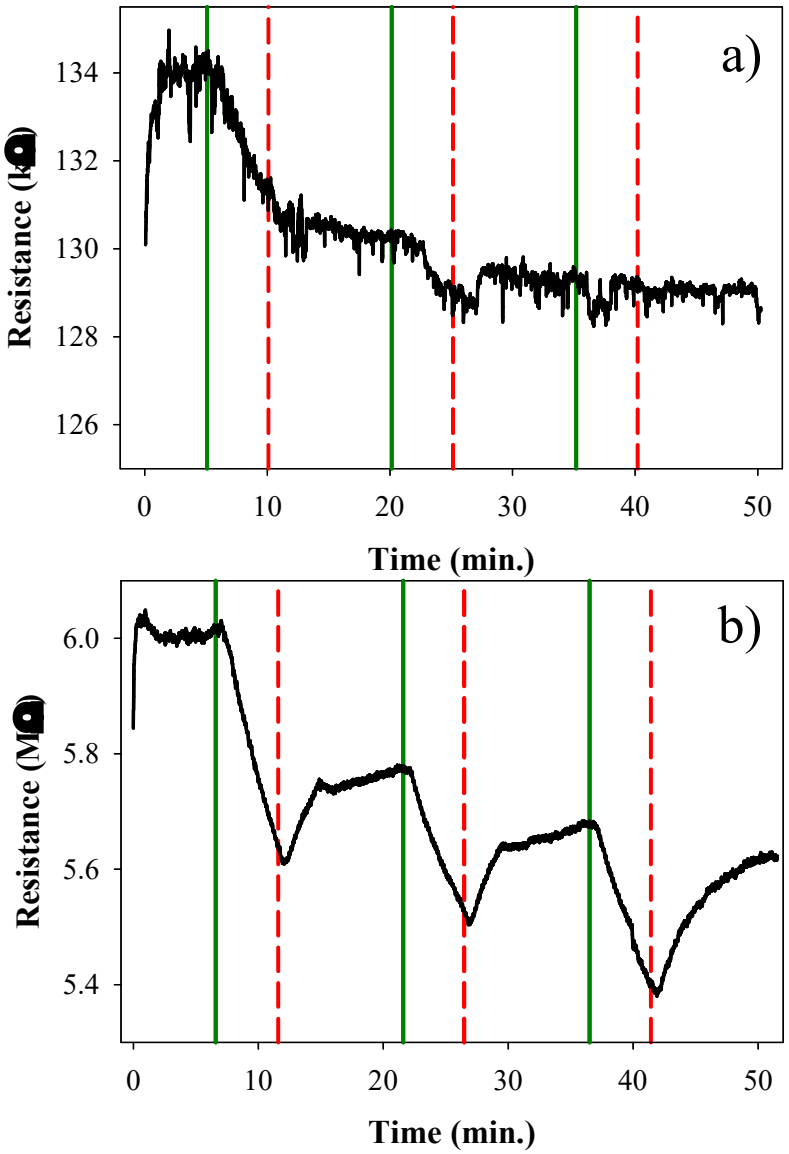

Figure 4.8. Ethanol response and recovery behavior of (a) UT sensor at T_S = 25 °C and (b) 15 W plasma-treated sensors at T_S = 50 °C. Solid (green) and dashed (red) lines indicate ethanol gas flow on and off, respectively.

there is some reactivity of the SnO_2 surface, leading to the observed decrease in resistance. But these active sites do not seem to regenerate during the EtOH "off-time" at this low T_S, resulting in a significantly smaller decrease in resistance with the second EtOH exposure and finally no change in resistance with the final exposure. This observed poisoning of the SnO_2 surface demonstrates that the UT material can only detect EtOH once before having to be replaced when operating at these low T_S.

Fig. 4.8b and Fig 2.1 shows the resistance of two PGS devices treated in 15 and 60 W plasmas (p = 140 mTorr) when exposed to EtOH at T_S = 50 and 25 °C, respectively. Like the UT sensors, the R_{air} does not recover fully to the initial resistance before any EtOH exposure for both PGS devices, once again indicating these reactive ionosorbed species were not completely reformed during the EtOH "off-time". The repeatable response and recovery behavior, however, might be a good indicator that either the total amount of surface reactive sites increased (therefore the EtOH poisoning did not have as much of an impact) or regeneration of reactive adsorbed oxygen occurred more efficiently after plasma treatment. Although the R_{air} does not recover to the starting value before any EtOH exposure, the R_{air} during each "off time" does stabilize, suggesting that the PGS could be reusable after recalibrating the device to this new resistance. Thus, along with improved response and recovery behavior, the plasma treated PGS also have the potential to be reused, whereas the UT sensors do not. Furthermore, this allows us to calculate recovery times relatively easily. From these data, the recovery times are estimated at 159 ± 15 s and 190 ± 14 s for the lower and higher P treated PGS, respectively. Similar to the T_S dependent results, the 15 W PGS performs better as an EtOH sensor as a result of its shorter recovery time and the observation that the resistance recovers more during the EtOH off periods. For comparison, a recent study of Pd/SnO_2 hollow submicrosphere devices reported EtOH

response and recovery times of 1.5 s and 18 s, respectively.[28] These measurements were made, however, at T_S = 300 ºC, considerably higher than the 25 to 50 ºC used here. Notably, another recent study of Pd/SnO_2 nanoceramics found room temperature CO response and recovery times of 30 and 40 s, respectively.[29] This study, however, heat treated their materials at temperatures of 600 – 1200 ºC as part of the fabrication process, making direct comparison to our materials difficult as annealing the SnO_2 can have a drastic effect on sensor response. Additionally, both examples utilized SnO_2 doped with another metal (Pd), complicating the material synthesis procedure and dramatically increasing device production cost.

Note that the resistance in EtOH does not stabilize but continues to decline throughout the 5 min exposure time. As such, we chose to not calculate response times directly from these data as they may not be truly representative of the performance of the plasma treated PGSs. Thus, as described in Chapter 2, an alternate approach to evaluating responsiveness was used by fitting each of the R_{EtOH} portions of these resistance curves with a linear regression (R^2 values were all >0.99). The resulting slopes provide a measure of the response rate for each sensor. For the sensors treated in the 15 and 60 W plasmas, we calculated a response rate of $1.1 \pm 0.3 \times 10^{-3}$ MΩ/s and $3.0 \pm 0.7 \times 10^{-4}$ MΩ/s, respectively.

It is well established that tuning T_s can improve sensor selectivity for a specific analyte and can also affect reaction kinetics at the material surface.[5, 9, 26] Recently, it was suggested that lower operating temperatures result in larger response with hybrid SMO sensors because the adsorption-desorption process occurs too quickly at higher T_S to be monitored by changes in bulk resistance.[30] A similar phenomenon may also be occurring with the plasma treated sensors, resulting in better sensor performance with slower reaction kinetics. Note that sensor response to EtOH in these dynamic studies do not match the expected values calculated in the static studies

at these $T_{S,}$ shown in Fig. 4.6. This is probably because during EtOH exposure, the R_{EtOH} continues to decrease during the entire "on time", indicating that the static sensing response values represent a maximum expected response to a gas and not the actual response that the sensor will demonstrate in real time. Thus, the static and dynamic studies should be performed in tandem to first determine the optimal modification and operating temperature parameters for a specific gas, then to monitor the real-time device performance.

Sensing data were also collected to determine if system pressure is another parameter that could be tuned to improve sensor performance. Figure 4.9 shows the response to EtOH, CO, and benzene of the sensors treated at various pressures and P = 60 W. Similar to the P = 15 W treatment (see Fig. 4.6a) the p = 100 mTorr treatment resulted in an increased response to EtOH and benzene, when compared to the UT device. These PGSs, however, have a lower response to all target gases when compared to the p = 140 mTorr treated PGSs. Thus, plasma treatment in general improves the gas sensing behavior of SnO_2; however, altering the pressure does not have as positive an impact as changing the applied rf power for the pressures studied herein.

Another study examined the gas sensing properties of Ar/O_2 plasma-treated SnO_2 nanowires as a function of applied rf power.[13] With the exception of nanowires treated at 80 W, and coworkers also saw a similar trend when looking at R_{air} as a function of treatment time.[14] We have collected similar data on our sensors, Fig. 4.10, and find that R_{air} decreases with applied plasma treatment resulted in an overall improved response to EtOH for elevated T_S = 220 – 250 °C. The 40 W treatment had a response of 4.98 and demonstrated reproducible response and recovery behavior at 250 °C. Pan *et al.* attribute the improved performance after plasma treatment to an increase in oxygen vacancies on the surface and a resulting increase in chemisorbed oxygen, as demonstrated by the increase in R_{air} with increasing applied power.

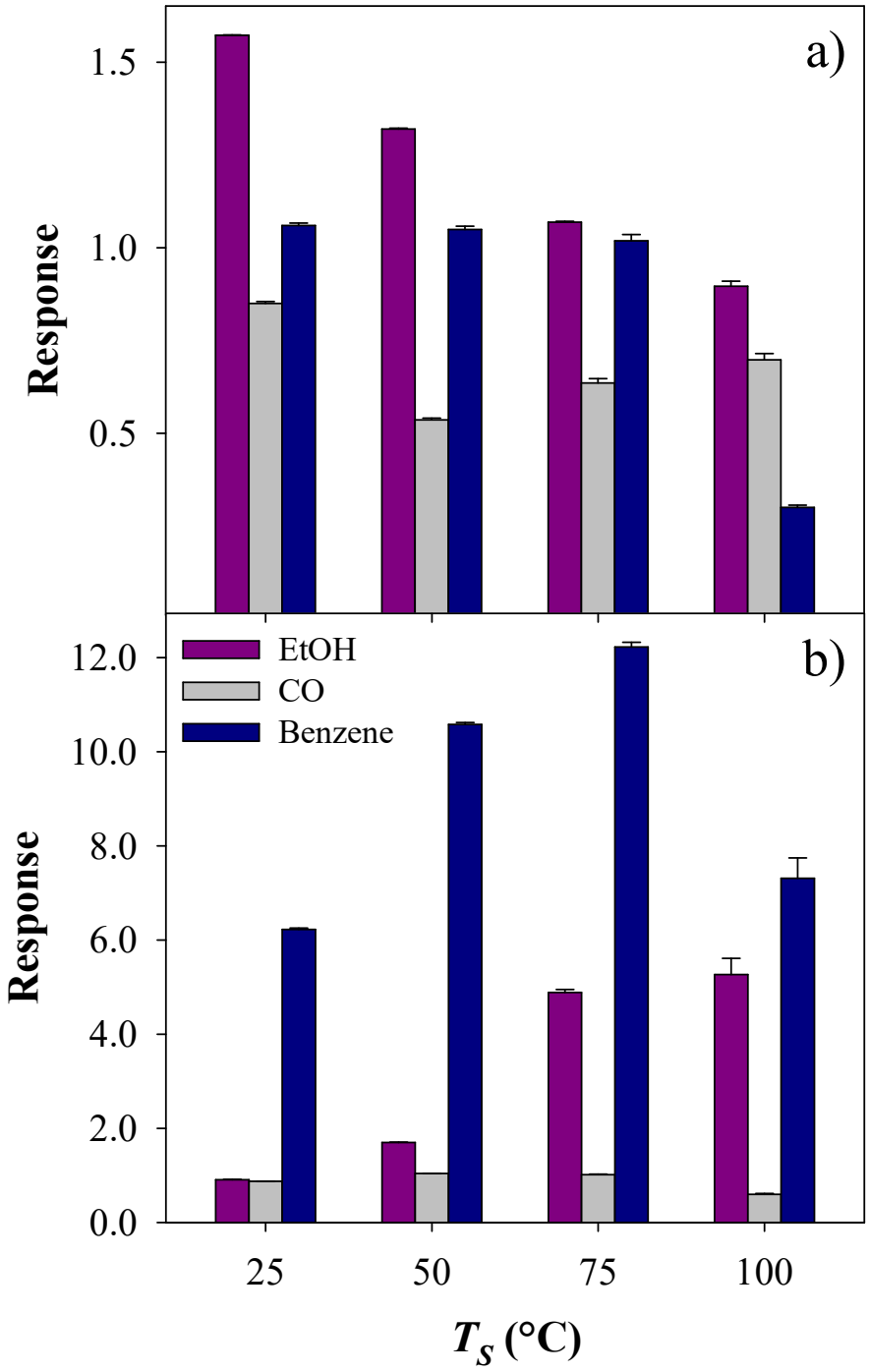

Figure 4.9. Temperature dependent response to ethanol$_{(v)}$, 100 ppm CO, and 100 ppm benzene of PGS devices plasma treated at P = 60 W and p = (a) 50 and (b) 100 mTorr. Calculated weighted error is ≤0.85% of response where not visible.

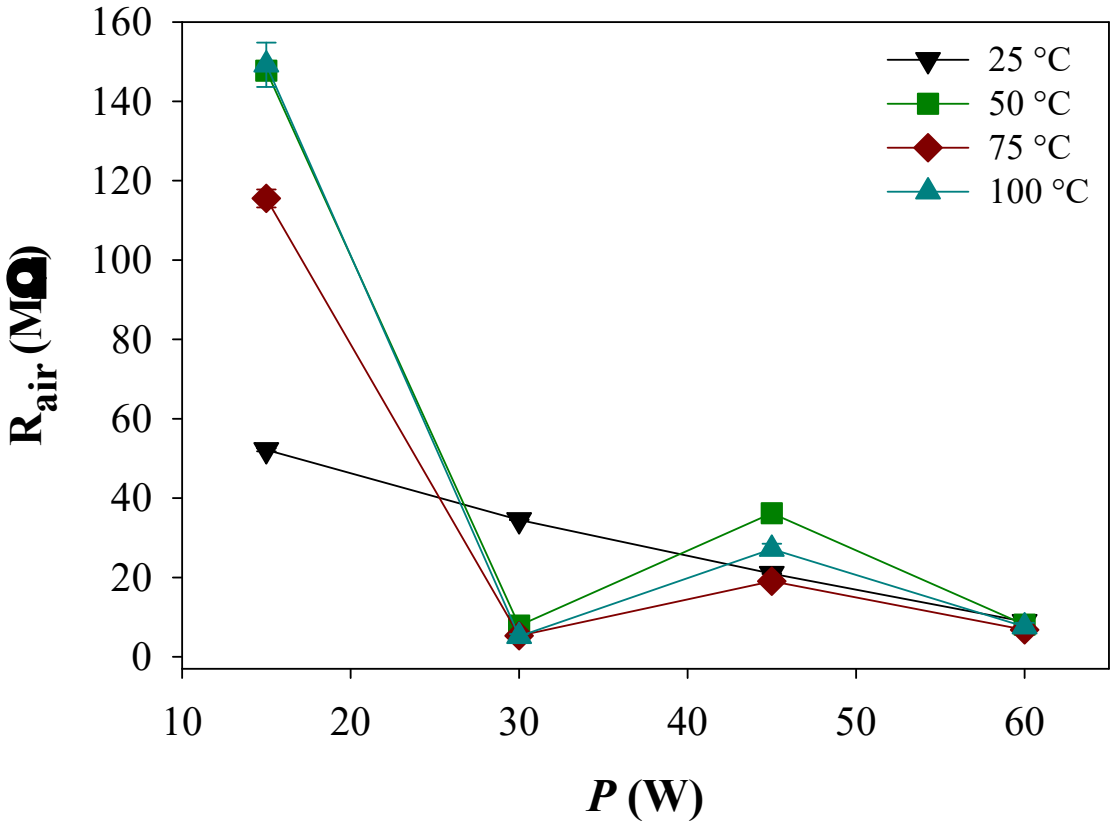

Figure 4.10. Raw resistance of PGS in air at T_s = 25 – 100 °C as a function of *P* with *p* = 140 mTorr. Error on all points represent standard deviation calculated from the mean of n = 3 trials.

Likewise, Beniwal power for most of the powers studied (at p = 140 mTorr). Based on the literature interpretation of these trends, it appears the 15 W treatment results in the most chemisorbed oxygen with which the target gases can interact, leading to the largest responses toward the gases tested. In addition, the R_{air} for the 60 W treated PGS seems to be independent of temperature, overall indicating that T_S is less of a factor for sensors treated under these changes, and ultimately resulting in improved gas sensing at room temperature.

To understand why these changes in oxygen adsorption resulted in such intense changes in response for plasma-treated sensors, we must consider how each of the target gases interacts with the SMO surface. In their computational studies, Yue *et al.* found that on the SnO_2(110) surface, EtOH first adsorbs specifically to the bridging oxygen position and subsequently desorbs with that oxygen atom, ultimately resulting in a net gain of an electron to the SnO_2 matrix, an overall reducing interaction.[31] Because the 15 W treated sensor displays the highest $R_{air,}$ we can assume it has the most adsorbed oxygen (in the bridging position or otherwise). As such, this sensor should have the largest response to EtOH, which is exactly what we see, Fig. 4.6. Similarly, Tamaki *et al.* determined CO reacts with an adsorbed bridging oxygen; however, they found CO also needs to interact with a lattice oxygen to form the CO_3^{2-} structure observed in infrared spectra.[32] Therefore, just creating a high concentration of oxygen vacancies may not produce the best CO sensor because both adsorbed and lattice oxygen atoms are required. Our data reflect this observation as the 15 W treatment did not display a large response to CO. This suggests the plasma treatment under these conditions did not result in an optimal ratio of adsorbed to lattice oxygen for CO detection. In contrast, the 60 W treatment displayed the greatest response to CO, Fig. 4.6d, which indicates this plasma treatment created a surface that preferentially responds to CO, likely because it had a more optimal O_{ads}/O_{lat} ratio.

Overall, the observation that different plasma treatments result in sensors that respond differentially to different analytes indicates that this approach could provide the capability of producing tailored PGS that are both selective and sensitive to specific gases. Clearly, additional work is needed to fully understand the plasma-surface interactions as well as the resulting sensor performance for these unique devices. Thus, next steps for further improving our sensing materials include examining alternate fabrication strategies and materials with an eye specifically toward improving the response/recovery times for ethanol as well as the other analytes and measuring additional performance metrics such as selectivity in mixed gas exposures. Alternate SMO architectures that more conformally coat the paper substrate could also further improve the performance of these PGS.

4.3 Summary

Here, a simple, inexpensive fabrication technique for PGS devices effectively produced a gas sensor capable of detecting a range of analytes at room temperature. Device characterization and performance studies indicate that plasma treated PGSs have the potential to be reusable and show significant promise when compared to the UT sensors. Upon plasma surface modification, response to all target gases was significantly increased over that for control devices. Moreover, the room temperature response and recovery behavior in the presence of EtOH suggests these PGS devices can effectively operate at reduced T_S relative to current commercially available SMO sensors. Ongoing studies of PGS in our laboratory will examine morphologies that will optimize conformal treatment of the substrate to maximize the amount of accessible SMO. Exploring a larger parameter space with our plasma treatments, including alternative precursor gases and an expanded pressure/power regime, will allow further understanding of the relationship between material properties and gas sensing performance. These two strategies

work toward achieving better fundamental understanding of the mechanisms behind SMO gas detection, and thereby the development of targeted approaches to effective gas sensor design.

REFERENCES

1. Bonney, R.; Shirk, J. L.; Phillips, T. B.; Wiggins, A.; Ballard, H. L.; Miller-Rushing, A. J.; Parrish, J. K., Next Steps for Citizen Science. *Science* **2014,** *343* (6178), 1436.
2. Snyder, E. G.; Watkins, T. H.; Solomon, P. A.; Thoma, E. D.; Williams, R. W.; Hagler, G. S. W.; Shelow, D.; Hindin, D. A.; Kilaru, V. J.; Preuss, P. W., The Changing Paradigm of Air Pollution Monitoring. *Environ. Sci. Technol.* **2013,** *47* (20), 11369-11377.
3. Environmental Defence Fund., Pathways 2025: EDF Strategic Plan. Environmental Defence Fund: 2017.
4. Nikzad, N.; Verma, N.; Ziftci, C.; Bales, E.; Quick, N.; Zappi, P.; Patrick, K.; Dasgupta, S.; Krueger, I.; Rosing, T. Š.; Griswold, W. G., CitiSense: Improving Geospatial Environmental Assessment of Air Quality Using a Wireless Personal Exposure Monitoring System. In *Proceedings of the Conference on Wireless Health*, ACM: San Diego, California, 2012; pp 1-8.
5. Dey, A., Semiconductor Metal Oxide Gas Sensors: A review. *Mater. Sci. Eng., B* **2018,** *229*, 206-217.
6. Degler, D., Trends and Advances in the Characterization of Gas Sensing Materials Based on Semiconducting Oxides. *Sensors* **2018,** *18* (10), 3544.
7. Gardon, M.; Guilemany, J. M., A Review on Fabrication, Sensing Mechanisms and Performance of Metal Oxide Gas Sensors. *J. Mater. Sci.: Mater. Electron.* **2013,** *24* (5), 1410-1421.
8. Bârsan, N.; Weimar, U., Understanding the Fundamental Principles of Metal Oxide Based Gas Sensors; the Example of CO Sensing with SnO_2 Sensors in the Presence of Humidity. *J. Phys.: Condens. Matter* **2003,** *15* (20), R813-R839.
9. Batzill, M.; Diebold, U., The Surface and Materials Science of Tin Oxide. *Prog. Surf. Sci.* **2005,** *79* (2-4), 47-154.
10. Suematsu, K.; Yamada, K.; Yuasa, M.; Kida, T.; Shimanoe, K., Evaluation of Oxygen Adsorption Based on the Electric Properties of SnO_2 Semiconductor Gas Sensors. *Sens.* **2016,** *28* (11), 1211-1217.
11. Gimenez, A. J.; Yáñez-Limón, J. M.; Seminario, J. M., ZnO−Paper Based Photoconductive UV Sensor. *J. Phys. Chem. C* **2011,** *115* (1), 282-287.
12. Gimenez, A. J.; Luna-Bárcenenas, G.; Sanchez, I. C.; Yáñez-Limón, J. M., Paper-Based ZnO Oxygen Sensor. *IEEE Sens. J.* **2015,** *15* (2), 1246-1251.
13. Pan, J.; Ganesan, R.; Shen, H.; Mathur, S., Plasma-Modified SnO_2 Nanowires for Enhanced Gas Sensing. *J. Phys. Chem. C* **2010,** *114* (18), 8245-8250.
14. Beniwal, A.; Sahu, P. K.; Sunny In *Enhanced Sensing Performance of Nanostructured SnO_2 Sensor Through Oxygen Plasma Treatment*, 2018 IEEE SENSORS, 28-31 Oct. 2018; 2018; pp 1-4.
15. Stuckert, E. P.; Miller, C. J.; Fisher, E. R., The Effect of Ar/O_2 and H_2O Plasma Treatment of SnO_2 Nanoparticles and Nanowires on Carbon Monoxide and Benzene Detection. *ACS Appl. Mater. Interfaces* **2017,** *9* (18), 15733-15743.
16. Stuckert, E. P.; Fisher, E. R., Ar/O_2 and H_2O Plasma Surface Modification of SnO_2 Nanomaterials to Increase Surface Oxidation. *Sens. Actuators B* **2015,** *208*, 379-388.
17. Shearer, J. C.; Fisher, E. R., Design and Operation of a Rotating Drum Radio Frequency Plasma Reactor for the Modification of Free Nanoparticles. *Rev. Sci. Instrum.* **2013,** *84* (6), 063904.

18. Pegalajar-Jurado, A.; Mann, M. N.; Maynard, M. R.; Fisher, E. R., Hydrophilic Modification of Polysulfone Ultrafiltration Membranes by Low Temperature Water Vapor Plasma Treatment to Enhance Performance. *Plasma Process. Polym.* **2016,** *13* (6), 598-610.
19. Tompkins, B. D.; Dennison, J. M.; Fisher, E. R., Etching and Post-Treatment Surface Stability of Track-Etched Polycarbonate Membranes by Plasma Processing Using Various Related Oxidizing Plasma Systems. *Plasma Process. Polym.* **2014,** *11* (9), 850-863.
20. Hawker, M. J.; Pegalajar-Jurado, A.; Fisher, E. R., Conformal Encapsulation of Three-Dimensional, Bioresorbable Polymeric Scaffolds Using Plasma-Enhanced Chemical Vapor Deposition. *Langmuir* **2014,** *30* (41), 12328-12336.
21. Johansson, L.-S.; Campbell, J. M., Reproducible XPS on Biopolymers: Cellulose Studies. *Surf. Interface Anal.* **2004,** *36* (8), 1018-1022.
22. Ciftyürek, E.; Šmíd, B.; Li, Z.; Matolín, V.; Schierbaum, K., Spectroscopic Understanding of SnO_2 and WO_3 Metal Oxide Surfaces with Advanced Synchrotron Based; XPS-UPS and Near Ambient Pressure (NAP) XPS Surface Sensitive Techniques for Gas Sensor Applications Under Operational Conditions. *Sensors* **2019,** *19* (21), 4737.
23. Szuber, J.; Czempik, G.; Larciprete, R.; Koziej, D.; Adamowicz, B., XPS Study of the L-CVD Deposited SnO_2 Thin Films Exposed to Oxygen and Hydrogen. *Thin Solid Films* **2001,** *391* (2), 198-203.
24. Stuckert, E. P.; Miller, C. J.; Fisher, E. R., Gas-phase Diagnostics During H_2 and H_2O Plasma Treatment of SnO_2 Nanomaterials: Implications for Surface Modification. *J. Vac. Sci. Technol., B* **2017,** *35* (2), 021802.
25. Trevino, K. J.; Fisher, E. R., Detection Limits and Decomposition Mechanisms for Organic Contaminants in Water Using Optical Emission Spectroscopy. *Plasma Process. Polym.* **2009,** *6* (3), 180-189.
26. Ihokura, K.; Watson, J., *The Stannic Oxide Gas Sensor: Principles and Applications*. CRC Press: Boca Raton, 1994.
27. Wang, S. C.; Chang, K. S.; Yuan, C. J., Enhancement of Electrochemical Properties of Screen-Printed Carbon Electrodes by Oxygen Plasma Treatment. *Electrochim. Acta* **2009,** *54* (21), 4937-4943.
28. Xiao, L.; Xu, S.; Yu, G.; Liu, S., Efficient Hierarchical Mixed Pd/SnO_2 Porous Architecture Deposited Microheater for Low Power Ethanol Gas Sensor. *Sens. Actuators B* **2018,** *255*, 2002-2010.
29. Zhu, S.; Liu, Y.; Wu, G.; Fei, L.; Zhang, S.; Hu, Y.; Yan, Z.; Wang, Y.; Gu, H.; Chen, W., Mechanism Study on Extraordinary Room-Temperature CO Sensing Capabilities of Pd-SnO_2 Composite Nanoceramics. *Sens. Actuators B* **2019,** *285*, 49-55.
30. Walker, J. M.; Akbar, S. A.; Morris, P. A., Synergistic Effects in Gas Sensing Semiconducting Oxide Nano-Heterostructures: A Review. *Sens. Actuators B* **2019,** *286*, 624-640.
31. Yue, J.; Jiang, X.; Yu, A., Adsorption of the OH Group on SnO_2(110) Oxygen Bridges: A Molecular Dynamics and Density Functional Theory Study. *J. Phys. Chem. C* **2013,** *117* (19), 9962-9969.
32. Jun, T.; Masaki, N.; Yasutake, T.; Norio, M.; Noboru, Y.; Koji, M.; Yuji, N., Adsorption Behavior of CO and Interfering Gases on SnO_2. *Surf. Sci.* **1989,** *221* (1), 183-196.

CHAPTER 5

EFFECTS OF SURFACE HYDROPHOBICITY OF COMMON LAB COAT FABRICS ON NANOPARTICLE ATTACHMENT AND RESUSPENSION[1]

The following chapter includes work done in collaboration with Ms. Sadia M. Sorna, Dr. Candace Tsai (Department of Environmental Health Sciences, University of California, Los Angeles), and Dr. Ronald Reifenberger (Department of Physics and Astronomy, Purdue University). Here, four common lab coat materials (100% cotton, 80/20 polyester/cotton blend, 100% polypropylene, and Tyvek®) were treated with a C_3F_8 or $H_2O_{(v)}$ plasma to alter the surface wettability. Changes in surface chemistry and wettability were measured using XPS and WCA goniometry for the untreated (UT) and plasma treated materials. Contamination and release of Al_2O_3 nanoparticles, carbon black, and carbon nanotubes were quantified using SEM image analysis. I would also like to thank Dr. Angela R. Hanna for performing XPS characterization of the UT materials and Dr. Rebecca C. Miller for SEM characterization during limited instrument access resulting from COVID-19 restrictions. Funding was provided by the National Science Foundation (NSF CBET-1803067) and the Department of Health and Human Services, Center for Disease Control and Prevention (R21OH011507-01).

5.1 INTRODUCTION

Nanomaterials have become widespread in various applications, such as healthcare, energy storage materials, sensing devices, and catalysis because of their unique physicochemical

[1]Adapted from the manuscript in preparation for submission to *ACS Applied Materials and Interfaces* by K. A. M. Hiyoto, S. Sorna, R. Reifenberger, C. S. Tsai, and E. R. Fisher.

properties and diverse morphologies and compositions.[1-2] Although some nanomaterials can originate from natural processes, many of these applications utilize engineered nanoparticles (ENP) to ensure control over properties like morphology, size, and composition. Prevention of adverse health effects arising from exposure to ENP is vital for both workers in facilities producing/using these materials and researchers in laboratories. The National Institute for Occupational Safety and Health (NIOSH) provides general guidelines for handling nanomaterials.[3] Secondary exposure from contaminated personal protective equipment (PPE) and recommendations for using these PPE, however, has not been widely studied. In particular, ENPs released from PPE (i.e. lab coats) can come into contact with skin and cause dermal exposure or it can be released back into the air and inhaled, leading to harmful respiratory and cardiovascular effects.[4-6]

McDonagh et al. studied the effect of particle size, level of physical activity, and fabric type on the resuspension of tagged silica particles.[7-8] The authors found that the smallest particles (3 μm) were easily deposited on the fabrics, but the number of particles released increased as particle size increased during resuspension. In addition, higher levels of physical activity while wearing the contaminated fabrics and the weave pattern, rather than the fabric composition were found to have a more significant impact on particle release. Although these studies thoroughly examined several factors impacting particle adhesion and release, the authors only employed micron sized silica and did not study the behavior of nanomaterials. Examination of nanoparticles could be useful, as Brownian motion can influence nanoparticle interaction (either adhesion or resuspension) and change the probability of secondary exposure with these materials. Previous work done in the Tsai lab demonstrated the adhesion and resuspension of Al_2O_3 nanoparticles (NP) with several common lab coats (polyester/cotton, Tyvek®, and

polyester).[6] It was found that the polyester/cotton coats had the highest level of contamination and release, whereas polyester had the lowest. Although this previous work looked at both woven and nonwoven fabrics, these studies were only performed with one type of nanomaterial morphology; thus, further work exploring more morphologically complex materials such as carbon nanotubes (CNT) is needed to determine if nanomaterial morphology also plays a role in ENP interaction. Expansion of previous work including studying the underlying mechanisms of NP adhesion and release from the contaminated PPE fabric requires further study to minimize secondary exposure.

In addition to expanding different morphologies of the nanomaterials studied, the role of surface properties of the fabrics themselves should also be explored. As seen in the above noted studies, fabric texture dominates when determining particle release. Even if the fabrics have a similar weave pattern or chemical composition, direct comparison between the different materials introduces a level of complexity such that the role of surface chemistry cannot be dismissed. Low-temperature plasma treatment is a useful strategy for tailoring surface properties as it allows for modification of the material's surface while maintaining the bulk properties. Plasmas have been used to both deposit a conformal thin film and to functionalize a variety of textiles and polymers.[9-11] By keeping the overall weave pattern of the fabrics the same and only modifying the surface chemistry, a direct comparison can be made to evaluate if this is an effective strategy to decrease secondary ENPs exposure.

5.2 RESULTS AND DISCUSSION

A significant goal of this work seeks to utilize plasma processing to deposit conformal coatings or to functionalize fabrics, ultimately improving potential PPE materials. Fluorocarbon (FC) plasmas have been extensively used to create hydrophobic surfaces through formation of a

FC film, where the film deposition process is hypothesized to be more efficient at lower y/x ratios of C_xF_y precursors.[12] C_3F_8 was thus selected as the precursor gas, as we have previously documented FC film formation on various substrate architectures, including wafers (Si, ZrO),[13-14] zeolites,[15] and complex polymer structures (scaffolds, electrospun fibers).[16-17] As these FC coatings result in hydrophobic surfaces, $H_2O_{(v)}$ plasma treated fabrics were also used to create a highly hydrophilic surface for comparison and to determine the role of hydrophobicity on nanomaterial attachment. Prior work in our lab examined the effect of $H_2O_{(v)}$ plasma treatment on polymeric membranes (polyethersulfone, polysulfone, track-etched polycarbonate, polyethylene, and polystyrene).[18-21] This system was chosen over O_2 plasmas because $H_2O_{(v)}$ plasma successfully implant O-containing functional groups on these polymers with less substrate etching and damage.

Atomic compositions of the untreated (UT), plasma treated fabrics are included in Table 5.1. The surface chemistry of the UT PP and Tyvek® materials is mostly carbon, 89.2 and 82.8% respectively, which supports the hydrocarbon chemical structure for both compounds. The 100% cotton (cotton) and blend samples showed an increased amount of O on the surface. Also note that the blend fabric contained small amounts of Si (4.8%). This is likely from the manufacturing process of these materials, as liquid Si is commonly used in a fabric softening step during the production of garments made of rougher materials (e.g. polyester). High-resolution C_{1s} XPS spectra are depicted in Figure 5.1 for all the UT fabrics studied herein, suggesting the surface of these materials consists of carbon in environments corresponding to C-C/C-H, C-O, and C=O at binding energies 284.6, 286, and 288.5 eV, respectively. As expected for the nonwoven fabrics (Fig. 5.1a and d), no C=O functionality was measured and these samples contained the smallest amount of C-O functionality. Cotton-containing materials

Table 5.1. XPS atomic composition of the UT and plasma treated fabric samples[a]

Plasma Precursor Gas	Material	C (%)	O (%)	Si (%)	F (%)
UT	PP	89.2 (0.9)	10.8 (0.9)	--	--
	Tyvek®	82.8 (2.6)	17.4 (2.4)	--	--
	blend	70.3 (0.6)	24.9 (0.9)	4.8 (0.6)	--
	cotton	65.9 (0.9)	33.9 (0.7)	--	--
C_3F_8	PP	82.0 (3.7)	9.8 (1.9)	--	8.1 (2.8)
	Tyvek®	77. 0 (1.0)	11.3 (2.1)	--	10.5 (1.9)
	blend	71.0 (2.1)	20.8 (1.0)	--	8.2 (1.3)
	cotton	64.9 (2.5)	22.7 (2.0)	--	12.5 (0.9)
	glass slide	32.1 (0.2)	28.9 (2.5)	11.1 (0.7)	27.8 (3.4)
$H_2O_{(v)}$	PP	85.6 (1.4)	14.3 (1.4)	--	--
	Tyvek®	82.3 (0.7)	17.7 (0.7)	--	--
	blend	71.0 (0.8)	29.0 (0.8)	--	--
	cotton	55.1 (0.8)	44.9 (0.8)	--	--

[a]All analyses were performed for an n = 6 – 9; standard deviation of the mean is reported in parentheses.

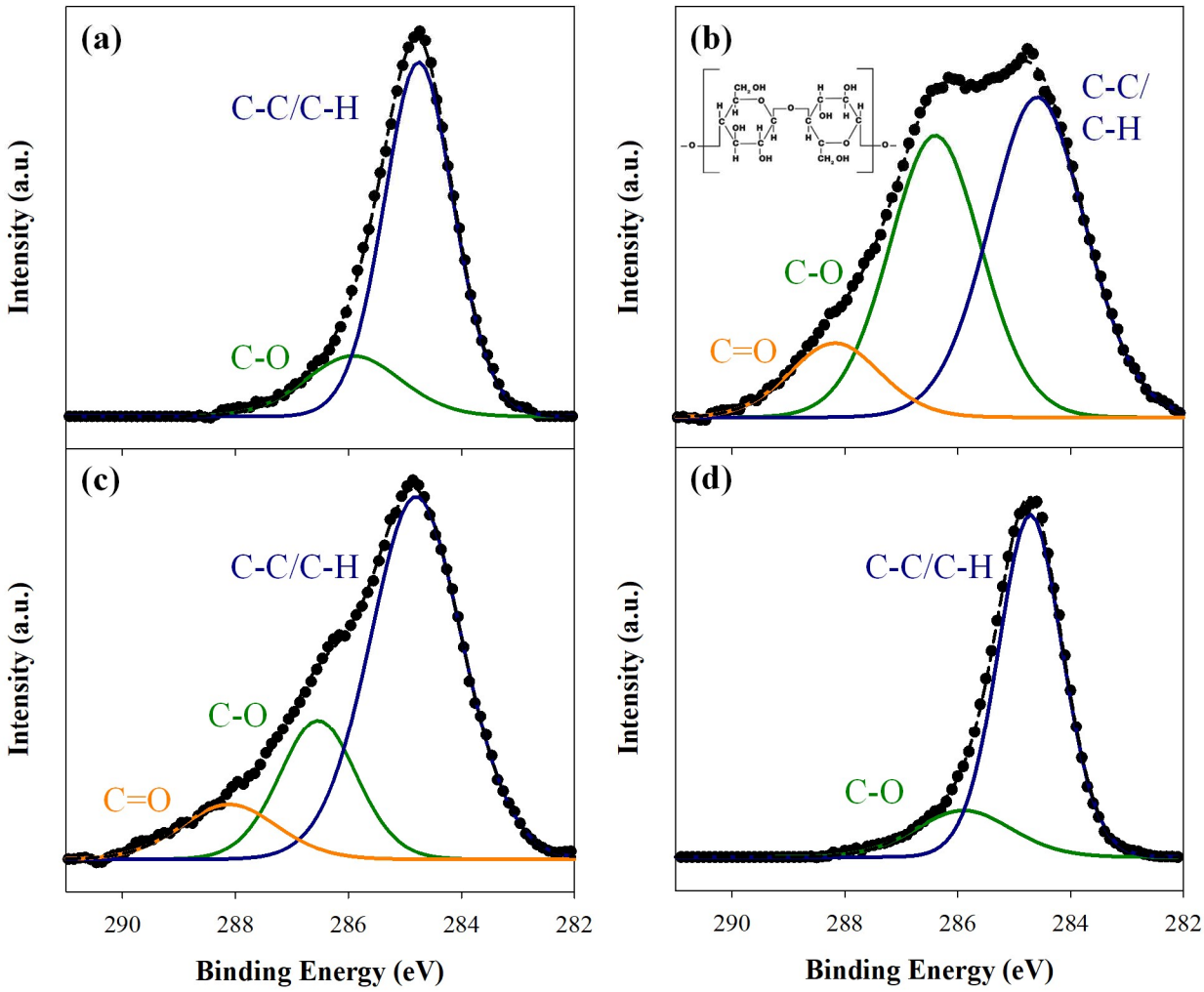

Figure 5.1. High-resolution C_{1s} XPS spectra of the UT (a) PP, (b) cotton, (c) blend, and (d) Tyvek®. Inset in (b) shows the chemical structure of cotton and peak labels correspond to assigned binding environments.

(Fig. 5.1b and c) show elevated amounts of oxygen bound to carbon functionality, again supported by the chemical structure of cotton, inset in Figure 5.1b.

Compared to the UT fabrics, the FC coated fabrics gained ~10% F (with corresponding decreases in percent O and C). The FC samples (Fig. 5.2) still retain a C-C/C-H peak centered at ~284.7 eV, arising from the underlying fabric. Although typical carbon-fluorine peaks (CF_3 at 293.5 eV and CF_2 at 292.0 eV) were not present, the high-resolution F_{1s} spectra have a prominent peak at ~689.0 eV, signifying that the samples contain some F-C binding. As the C-CF (286.9 eV) and CF (289.9 eV) peaks slightly overlap with the C-O and C=O peaks, it was challenging to fit these spectra with these binding environments separately. Therefore, the peaks at ~286.5 eV and ~288.1 eV were attributed to both the carbon-oxygen and carbon-fluorine peaks and labeled C-O/C-CF and C=O/CF, respectively. Because of the absence of some carbon-fluorine peaks and the low percent of F in all FC samples, a glass slide was treated with a FC plasma (p = 30 mTorr, P = 50 W, sample distance of 10 cm) to ensure film deposition was occurring in the reactor and that these unexpected results were a consequence of analyzing these morphologically complex fabrics. The high-resolution C_{1s} spectrum of this treated glass slide can be seen in Figure 5.3, and the atomic composition data are included in Table 5.1. Based on an O:Si ratio of ~2, both the O and Si contributions can be assigned to the glass substrate. In addition, these samples contain ~30% F (almost three times that of the fabric samples), indicating good film deposition under these parameters. Notably, the high-resolution C_{1s} spectrum contains all the expected carbon-fluorine peaks. Thus, the prominent contribution from the underlying fabric and low F concentration of the FC treated samples are likely sampling anomalies arising from the complex morphology.

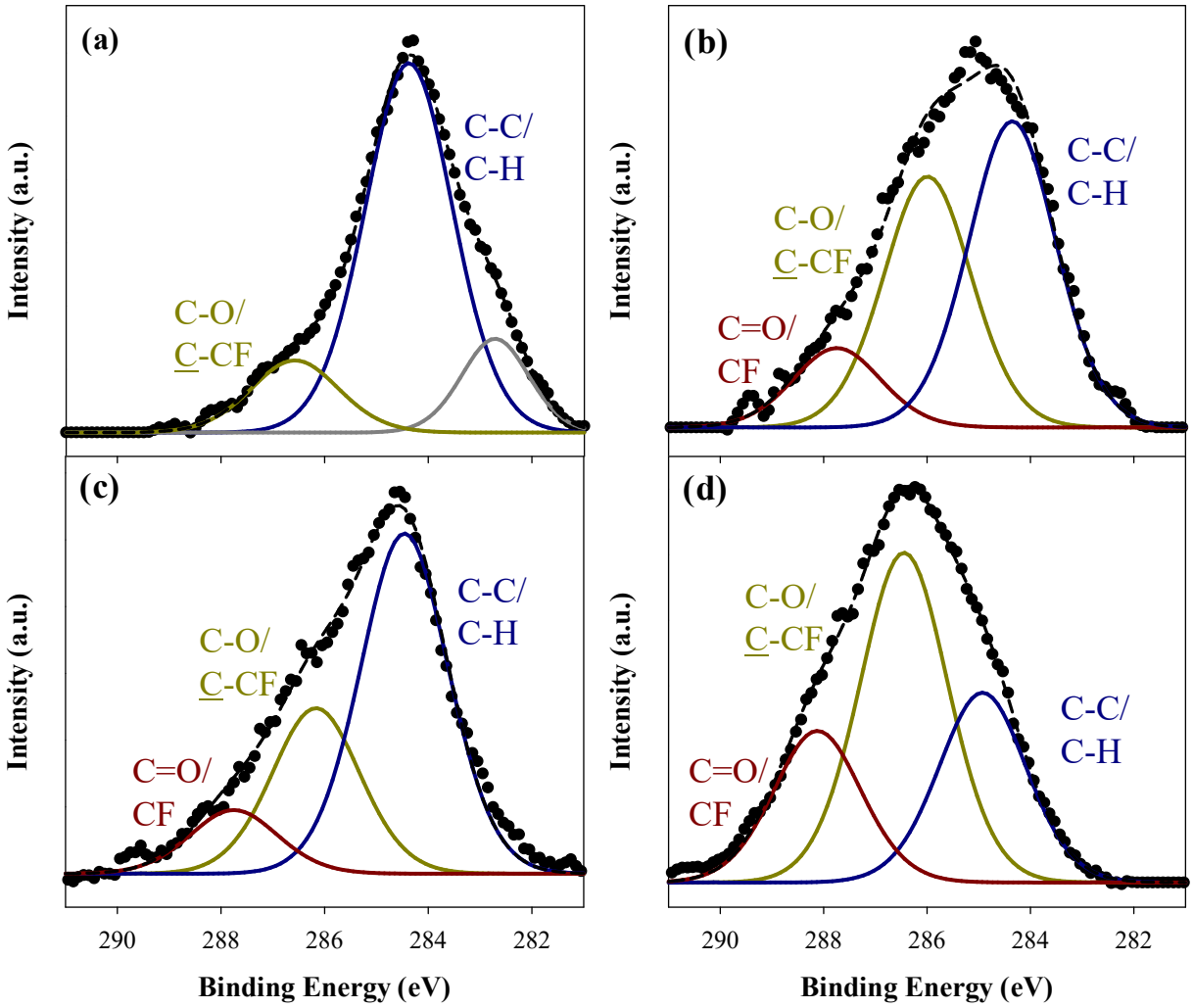

Figure 5.2. High-resolution C_{1s} XPS spectra for (a) PP, (b) cotton, (c) blend, and (d) Tyvek®, after FC plasma treatment (P = 50 W, p = 30 mTorr).

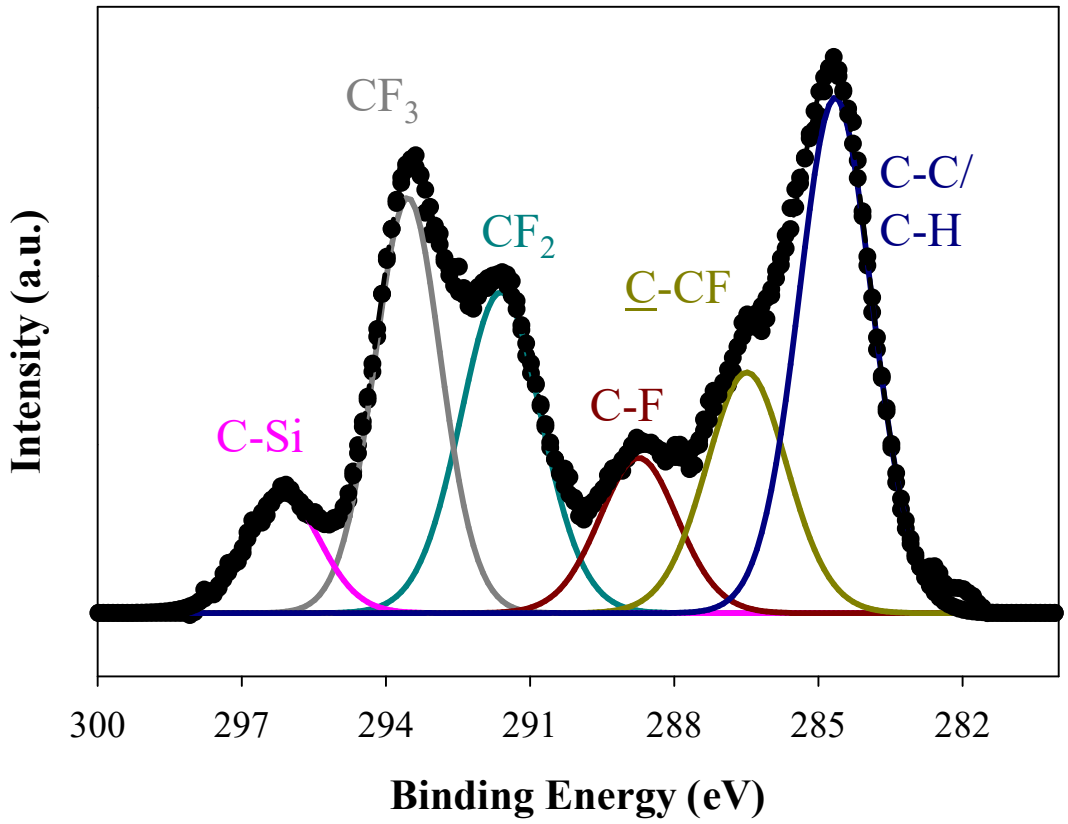

Figure 5.3. High-resolution C_{1s} XPS spectrum of a glass slide after FC treatment (P = 50 W, p = 30 mTorr). Labels correspond to assigned peak binding environments.

Similar to the FC treatment, only minor changes in the atomic composition of the fabrics are seen after $H_2O_{(v)}$ plasma exposure. This treatment resulted in all samples except for Tyvek® to have a 4 – 10% increase in surface O. Figure 5.4 contains the high-resolution C_{1s} spectra of the $H_2O_{(v)}$ materials, showing $H_2O_{(v)}$ plasma treatment of PP and Tyvek® samples increased C-O functionality and resulted in an additional peak corresponding to a C=O binding environment. Note that at three of the nine spots analyzed, the Tyvek® C_{1s} spectra looked identical to the UT fabric, indicating that O-functionalization was not consistent throughout the sample. The uneven functionalization could account for this being the only sample that did not have increased percent O after plasma treatment.

WCA analysis was used to monitor changes in surface wettability of the fabrics. As discussed previously,[16] measuring WCA on porous hydrophilic materials is challenging as the water drop tends to wick through the material, causing the WCA to change with time. As such, here we report static contact angles nominally hydrophobic materials with drops that do not appreciably change during the course of the measurement, and utilize dynamic WCA measurements to calculate absorption rates (volume of water absorbed per unit time) for nominally hydrophilic materials where the water drop disappears during analysis. In this way, we can nominally compare treatments by understanding either the change in static WCA and/or differences in water absorption rates. The static and dynamic WCA measurements of the UT and FC samples are shown in Table 5.2. These data reveal that UT PP and Tyvek® coats are hydrophobic (with static WCA of 121.7 ± 6.3° and 125.9 ± 4.5°, respectively) and the UT blend and cotton coats are hydrophilic (absorption rates of 4.24 ± 0.75 and 18.9 ± 3.5 μL/s, respectively). From the known chemical structures and XPS analysis, these results are expected

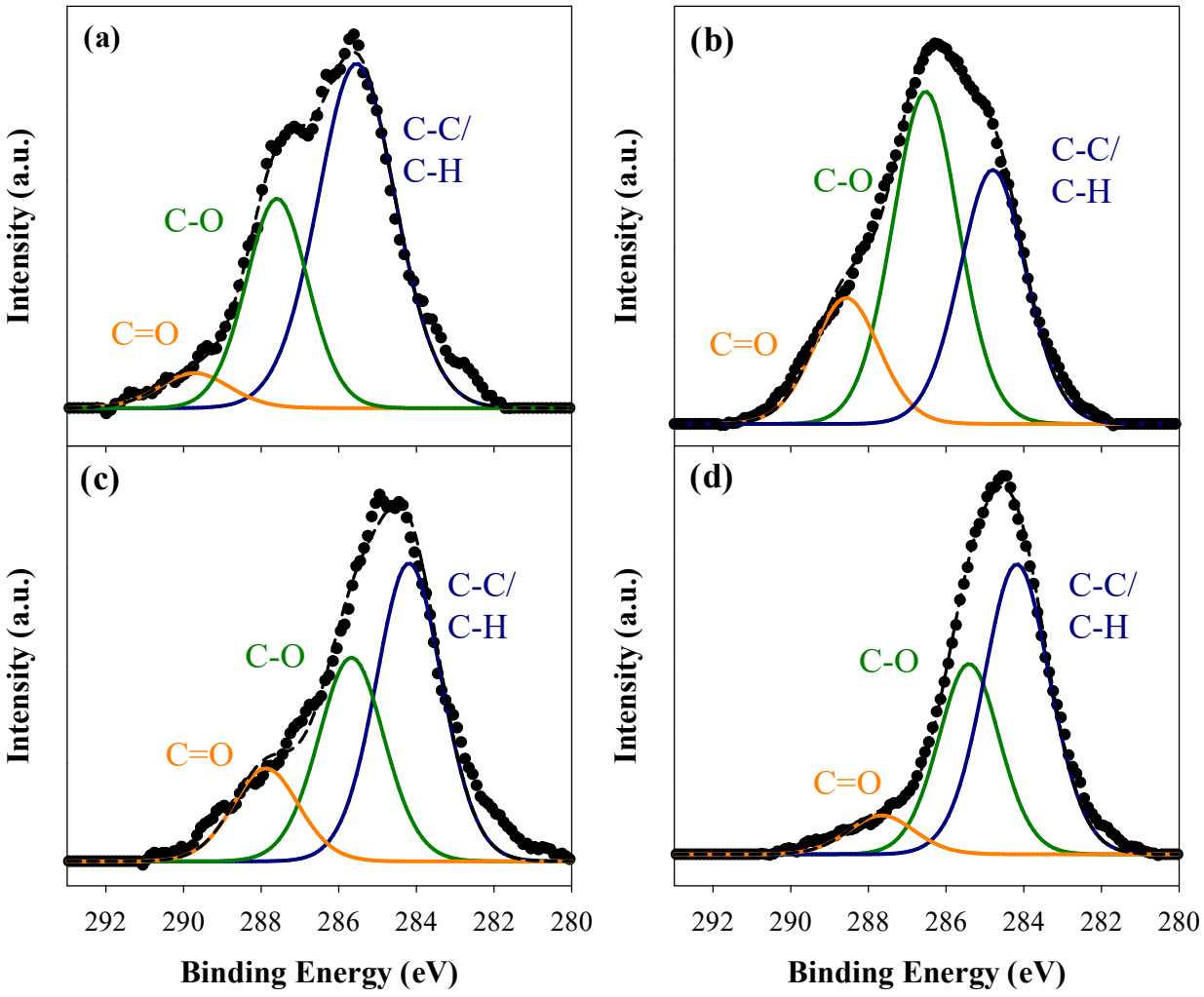

Figure 5.4. High-resolution C_{1s} XPS spectra for (a) PP, (b) cotton, (c) blend, and (d) Tyvek®, after $H_2O_{(v)}$ plasma treatment (P = 30 W, p = 15 mTorr).

Table 5.2. WCA for UT and FC plasma treated samples.[a]

	Coat	Static WCA (°)	Absorption Rate (μL s^{-1})
UT	PP	121.7 (6.3)	--
	Tyvek®	125.9 (4.5)	--
	blend		4.24 (0.75)
	cotton		18.9 (3.5)
C_3F_8	PP	123.7 (3.1)	--
	Tyvek®	125.0 (7.8)	--
	blend	--	0.101 (0.019)
	cotton	139.4 (2.6)	--

[a]All analyses were performed for n = 9; standard deviation of the mean is reported in parentheses.

as PP and Tyvek® (patented type of high-density polyethylene) are synthetic fibers composed of hydrocarbon polymers, while the cotton contains some oxygen functionality, nominally rendering cotton-containing materials more hydrophilic.

After FC plasma exposure, all materials have a static WCA above 120°, except for the blend, which has an absorption rate of 0.101 ± 0.019 μL/s. Although the Tyvek® and PP have the same WCA before and after FC plasma exposure, the cotton becomes a superhydrophobic material (WCA = 139.4 ± 2.6°), and the absorption rate of the blend is significantly reduced, indicating these materials are more hydrophobic compared to their UT counterparts. Previous work in our labs using similar treatment conditions suggests these coatings have a relatively smooth and amorphous morphology and are stable after long periods under ambient conditions.[13, 17] Iriyama *et al.* similarly treated white Nylon 6 fabric with various FC plasmas.[22] In their studies, the UT Nylon 6 "absorbed water immediately," but after C_3F_8 plasma exposure, the authors measured a static WCA of ~130°.[22] Another study successfully transformed cotton into a superhydrophobic material using chemical vapor deposition.[23] The polyaniline-coated cotton had a WCA of 156 ± 2°, which was only reduced to ~146° after washing 30 times, indicating a robust coating. Although this modification strategy resulted in a more hydrophobic material than the FC cotton in this work, the fabrication process required cleaning, rinsing, and drying steps and took over an hour to complete. In contrast, the method presented here does not need any extra sample preparation and takes ~15 min for the entire treatment process.

One possible explanation for why the FC plasma treated blend displays an absorption rate may be related to the weave pattern of natural fiber fabrics. Figure 5.5 contains low magnification SEM images of all UT samples and inset photographs of the materials. The blend

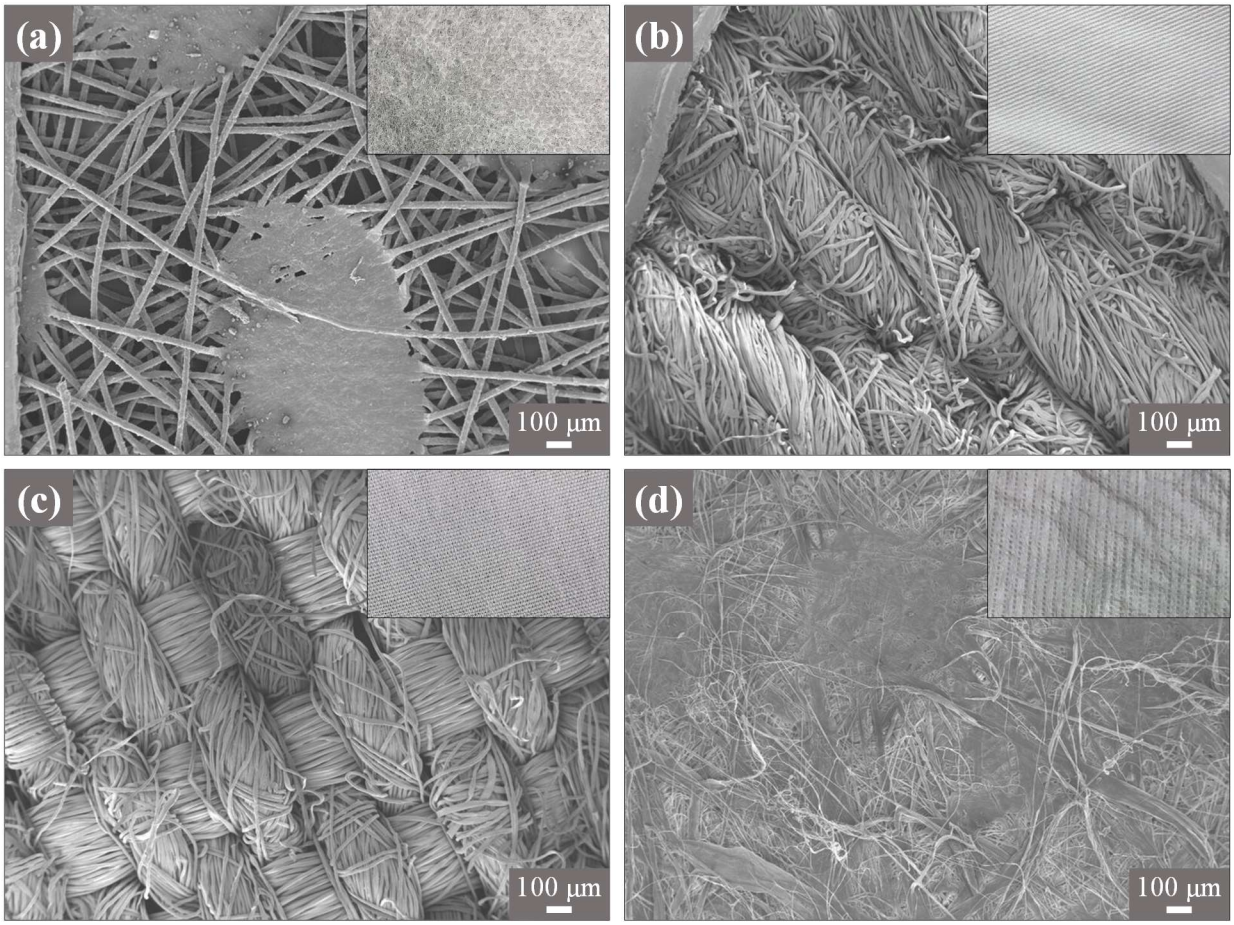

Figure 5.5. SEM images of UT (a) PP, (b) cotton, (c) blend, and (d) Tyvek®. All images taken at x50 magnification. All scale bars represent 100 µm and insets are photos of the fabric.

(Fig. 5.5c) has a plain weave, whereas the cotton (Fig. 5.5b) has a twill weave. Twill is typically the denser and more compact of the two weaves, potentially allowing a better blanket coverage with the FC coating, whereas the plain weave can have large gaps that the water can pass through. Visual inspection of the two fabrics (inset images in Fig. 5.5b and c) also shows these larger gaps, meaning that even if the individual fibers have a hydrophobic coating, the material is porous enough to still allow water to pass through it.

Table 5.3 lists WCA data of $H_2O_{(v)}$ plasma treated materials, clearly showing the increase in hydrophilicity compared to UT fabrics. The only sample that did not have a measurable absorption rate after $H_2O_{(v)}$ plasma exposure is PP. The WCA of this sample decreased by ~18° after plasma treatment, from ~122° (Table 5.2) to ~114°; nevertheless, this material is still considered hydrophobic.[16, 24] Harsher parameters (higher *P* and *p* and sample distance closer to the coil region of the plasma) were briefly explored, but resulted in the plasma burning a hole in the material within a minute of exposure to the plasma. Thus, further optimization of treatment conditions is needed to balance increasing the wettability of the PP while not significantly damaging the fabric.

For the remaining samples, an absorption rate was calculated after $H_2O_{(v)}$ plasma treatment. Similar to the UT materials, the $H_2O_{(v)}$ cotton has a much faster absorption rate than the blend (~46 and ~8 μL s^{-1}, respectively). The Tyvek® became very hydrophilic after $H_2O_{(v)}$ plasma modification, evidenced by the shift from a static WCA of ~126° to an absorption rate of 4.36 μL s^{-1}. The large error reported with these data comes from the absorbance rates ranging from 0.704 – 12.5 μL s^{-1}. Even with a more extensive sampling size (n = 18), the variability of these rates did not decrease, suggesting that the interaction of the $H_2O_{(v)}$ plasma with the Tyvek® is not as uniform as with the other materials. These data support the XPS results discussed

Table 5.3. WCA for fresh and aged $H_2O_{(v)}$ treated fabrics.[a]

Coat	Fresh	Aged – 2 Days	Aged – 1 month
Static WCA (°)			
PP	103.7 (8.7)	111.5 (4.6)	118.1 (5.1)
Absorption Rate (μL s^{-1})			
Tyvek®	4.36 (3.72)	4.27 (3.20)	4.78 (4.24)
blend	8.42 (1.32)	6.09 (1.74)	4.64 (1.60)
cotton	46.4 (5.2)	48.8 (4.7)	44.3 (5.2)

[a]All analyses were performed for n = 9; standard deviation of the mean is reported in parentheses.

previously, where some spots showed additional C-O and C=O functionality whereas other spots remain unchanged compared to the UT fabric. Again, this can be attributed to the challenge of treating substrates with complex morphologies.

Because WCA measurements reflect both the surface chemistry and morphology of the material,[16] these morphological changes can aid in explaining the observed WCA data of $H_2O_{(v)}$ treated samples. SEM images of UT and plasma treated fabrics, Figure 5.6, show that although all the samples experienced some degree of etching from $H_2O_{(v)}$ plasma exposure, the Tyvek® visually seems to have the most substantial morphological change. This plasma treatment enhanced the already existing texture of the fabric and sporadically formed large grooves on the material. Thus, the surface morphology may not be uniform between samples and even at different areas on the same sample, potentially contributing to the large error in the measured absorbance rates. The PP sample (Fig. 5.6c) does not have the same pitting observed on the other $H_2O_{(v)}$ fabrics, and this is the only material with a static WCA after plasma treatment. As with the $H_2O_{(v)}$ treated Tyvek®, the natural fibers (Fig. 5.6f and i) also have increased surface roughness after plasma treatment and demonstrated an increase in hydrophilicity when compared to the UT fabrics.

Previous work in our lab demonstrated that some plasma-treated polymeric materials experience some hydrophobic recovery after two weeks and up to a month after plasma modification.[21, 25] Hydrophobic recovery is thought to be caused at least partially by the rearrangement, or burying of high surface energy components (i.e. oxygen functionality) over time or chemical reactions with atmospheric O_2 and H_2O.[21, 25-26] To try and prevent the reorganization of surface functional groups, Holc *et al.* compared the WCA of O_2 plasma treated polyacrylonitrile aged at room temperature and 5 °C. Although both samples exhibited some

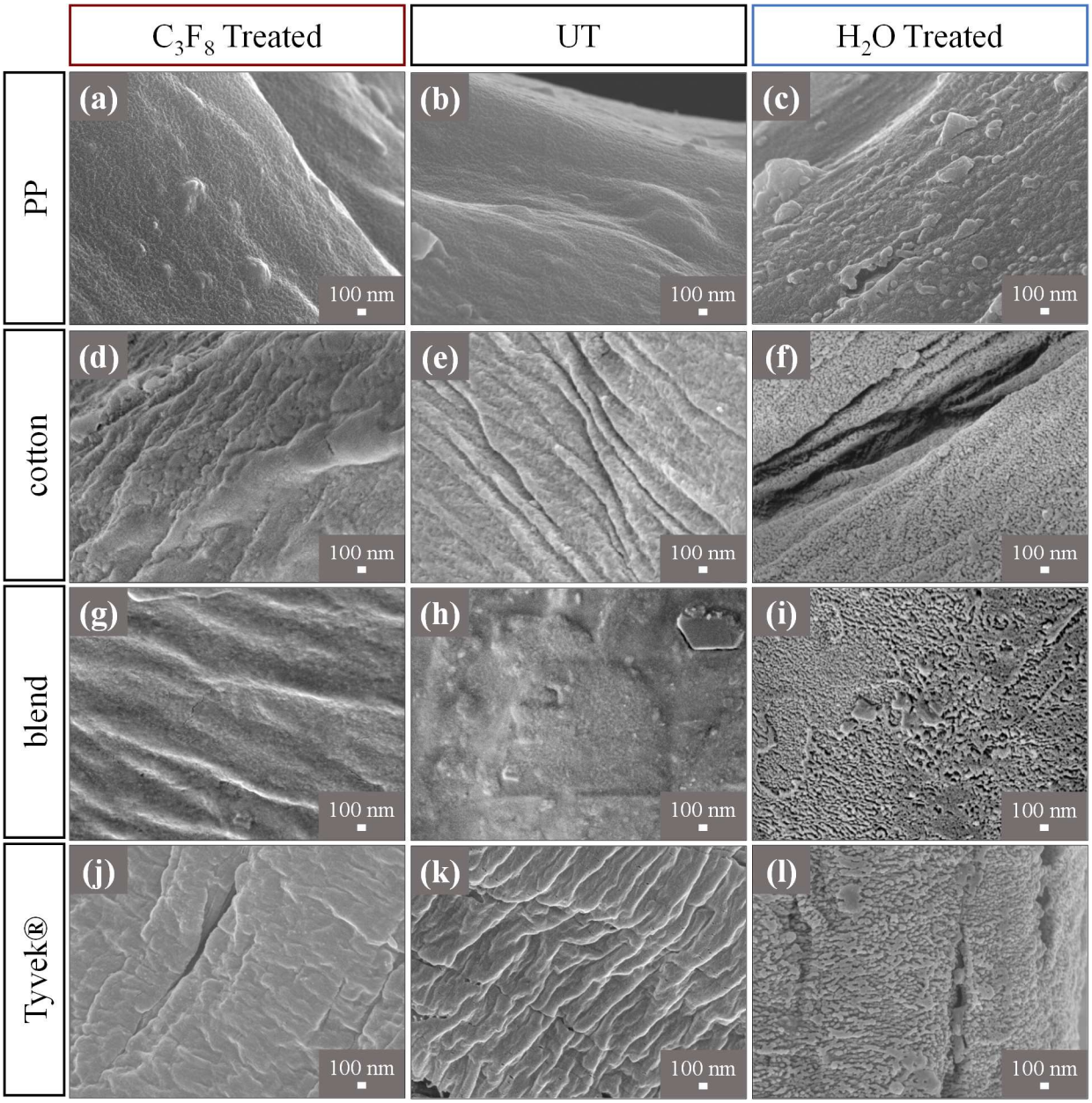

Figure 5.6. SEM images of (a – c) PP, (d-f) cotton, (g – i) blend, and (j – l) Tyvek® fabrics. The (b, e, h, k) UT, (a, d, g, j) FC and (c, f, i, l) $H_2O_{(v)}$ plasma treated samples were all Au coated prior to imaging. All images taken at x30,000 magnification and inset scale bars represent 100 nm.

hydrophobic recovery, the one stored at the lower temperature aged slower than the room temperature sample, which was attributed to the "less intensive" reorientation of surface groups at the lower temperature.[26] Therefore, for this work, WCA measurements of $H_2O_{(v)}$ treated samples were made after aging in ambient conditions to determine the relative permanence of the treatments. Samples were measured after aging two days and after one month. The shorter time measurement provided data to ensure the treatment was still effective at the time of the ENP exposure studies in the Tsai Lab. The 2-day aged samples still have WCA and absorption rates within experimental error of the freshly treated samples, indicating that the ENP contamination results were not impacted by the delay between plasma modification and nanomaterial contamination. WCA measurements made on the 1-month aged samples, however, suggest that hydrophobic recovery does occur but is dependent on the material. The 1-month $H_2O_{(v)}$ PP and blend have a WCA of 118.1° and an absorption rate of 4.64 $\mu L\ s^{-1}$, respectively. These values are within error of the UT material, meaning there was hydrophobic recovery for these fabrics. Notably, the 1-month aged Tyvek® sample continues to be completely wettable with a measurable absorption rate, whereas the UT material had a static WCA = 125.9°. Likewise, the cotton samples still had an absorption rate of 44.3 $\mu L\ s^{-1}$ compared to the UT material's absorption rate of 4.24 $\mu L\ s^{-1}$. These results suggest $H_2O_{(v)}$ plasma modification of the Tyvek® and cotton is stable enough to be an effective method to increase the hydrophilicity of these fabrics; however, further treatment optimization is needed for the PP and blend materials.

To understand the role of surface chemistry on ENP attachment and resuspension, both the UT and plasma modified materials were contaminated with either Al_2O_3 NP, carbon black, or CNT as described in Section 2.6. The number and size of ENP agglomerates were determined from SEM image analysis of the contaminated and shaken fabrics. Figures 5.7 and 5.8 show the

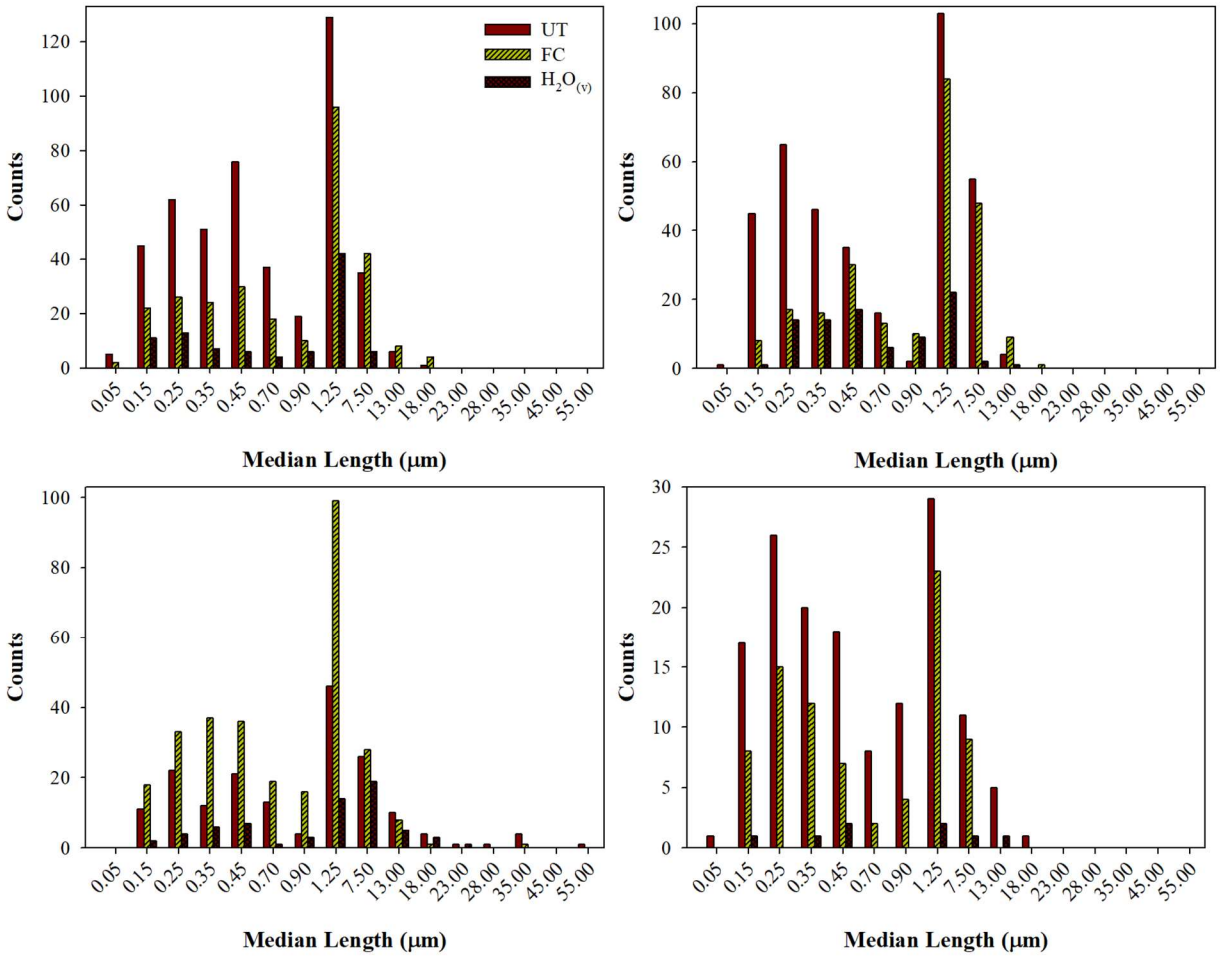

Figure 5.7. Carbon black agglomerates on (a – b) Tyvek® and (c – d) cotton. Agglomerates counted after (a, c) initial contamination and (b, d) shaking sample for 2 min.

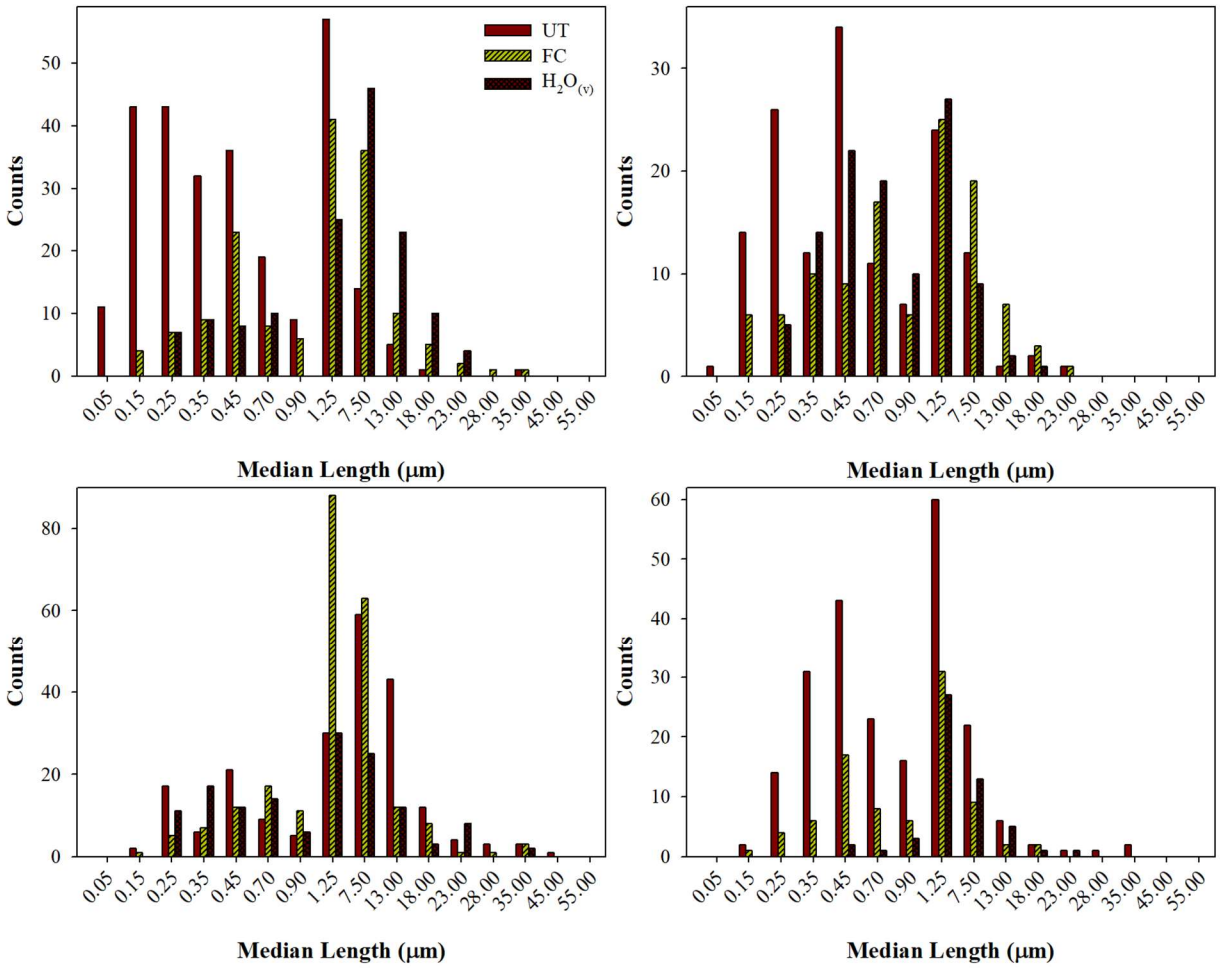

Figure 5.8. Carbon black agglomerates on (a – b) blend and (c – d) PP. Agglomerates counted after (a, c) initial contamination and (b, d) shaking sample for 2 min.

Table 5.4. Raw counts of carbon black agglomerates on UT and plasma treated fabrics after contamination and shaking.[a]

	Tyvek®						**cotton**						**PP**						**blend**					
	Contaminated			After Shaking			Contaminated			After Shaking			Contaminated			After Shaking			Contaminated			After Shaking		
Size Range	UT	FC	$H_2O_{(v)}$	UT	FC	$H_2O_{(v)}$	UT	FC	$H_2O_{(v)}$	UT	FC	$H_2O_{(v)}$	UT	FC	$H_2O_{(v)}$	UT	FC	$H_2O_{(v)}$	UT	FC	$H_2O_{(v)}$	UT	FC	$H_2O_{(v)}$
1-100nm	5	2	0	1	0	0	0	0	0	1	0	0	0	0	0	0	0	0	11	0	0	1	0	0
101-200nm	45	22	11	45	8	1	11	18	2	17	8	1	2	1	0	2	1	0	43	4	0	14	6	0
201-300nm	62	26	13	65	17	14	22	33	4	26	15	0	17	5	11	14	4	0	43	7	7	26	6	5
301-400nm	51	24	7	46	16	14	12	37	6	20	12	1	6	7	17	31	6	0	32	9	9	12	10	14
401-600nm	76	30	6	35	30	17	21	36	7	18	7	2	21	12	12	43	17	2	36	23	8	34	9	22
600-800nm	37	18	4	16	13	6	13	19	1	8	2	0	9	17	14	23	8	1	19	8	10	11	17	19
800nm-1um	19	10	6	2	10	9	4	16	3	12	4	0	5	11	6	16	6	3	9	6	0	7	6	10
1um-5um	129	96	42	103	84	22	46	99	14	29	23	2	30	88	30	60	31	27	57	41	25	24	25	27
5um-10um	35	42	6	55	48	2	26	28	19	11	9	1	59	63	25	22	9	13	14	36	46	12	19	9
11um-15um	6	8	0	4	9	1	10	8	5	5	0	1	43	12	12	6	2	5	5	10	23	1	7	2
16-20um	1	4	0	0	1	0	4	1	3	1	0	0	12	8	3	2	2	1	1	5	10	2	3	1
21-25um	0	0	0	0	0	0	1	0	1	0	0	0	4	1	8	1	0	1	0	2	4	1	1	0
26-30um	0	0	0	0	0	0	1	0	0	0	0	0	3	1	0	1	0	0	0	1	0	0	0	0
31-40um	0	0	0	0	0	0	4	1	0	0	0	0	3	3	2	2	0	0	1	1	0	0	0	0
41-50um	0	0	0	0	0	0	0	0	0	0	0	0	1	0	0	0	0	0	0	0	0	0	0	0
51-60um	0	0	0	0	0	0	1	0	0	0	0	0	0	0	0	0	0	0	0	0	0	0	0	0
Total #	**466**	**282**	**95**	**372**	**236**	**86**	**176**	**296**	**65**	**148**	**80**	**8**	**215**	**229**	**140**	**223**	**86**	**53**	**271**	**153**	**142**	**145**	**109**	**109**

[a]All measurements made for an n = 2 fabric samples.

number and size distribution of the carbon black contaminated fabrics with the raw counts included in Table 5.4. In general, for each material, the UT fabrics had the largest number of carbon black agglomerates for the contaminated and shaken samples, followed by the FC, and finally the $H_2O_{(v)}$. Also, the carbon black aggregates <400 nm typically show minor changes after shaking, demonstrating that the smaller clusters have better adhesion to the fabrics. For all three types of Tyvek®, the number of agglomerates is similar for the contaminated and shaken samples. These results suggest that although the Tyvek® does not prevent carbon black attachment, the particles do not resuspend, and the risk of secondary exposure is lower when compared to the other materials. With the cotton (Fig. 5.7c and d), the aggregate count is lower than the Tyvek® before and after shaking. The FC cotton had the most carbon black after contamination, but the number of agglomerates drastically decreased after shaking. The $H_2O_{(v)}$ samples also showed some ENP loss after shaking; however, the UT fabric had similar counts for the contaminated and shaken samples. These data suggest cotton has a lower risk of carbon black contamination, but only the UT fabric has potentially lower secondary exposure. The blend fabric (Fig. 5.8a and b) has one of the lower aggregate counts of the four coats studied. Although the UT and plasma treated materials showed some ENP release after shaking, the difference was not as significant as seen with the cotton samples. Interestingly, attachment of the carbon black on the PP (Fig. 5.10d) appears independent of plasma treatment, but only the plasma treated samples show a significant reduction in agglomerates after shaking.

Al_2O_3 NP aggregate counts on the fabrics are shown in Figures 5.9 and 5.10 and Table 5.4. Here, the initial attachment of the Al_2O_3 is lower than the carbon black, with minor count changes before and after shaking for clusters <600 nm. Like the carbon black studies, there is little change in the amount of Al_2O_3 before and after shaking the Tyvek® samples. The UT and

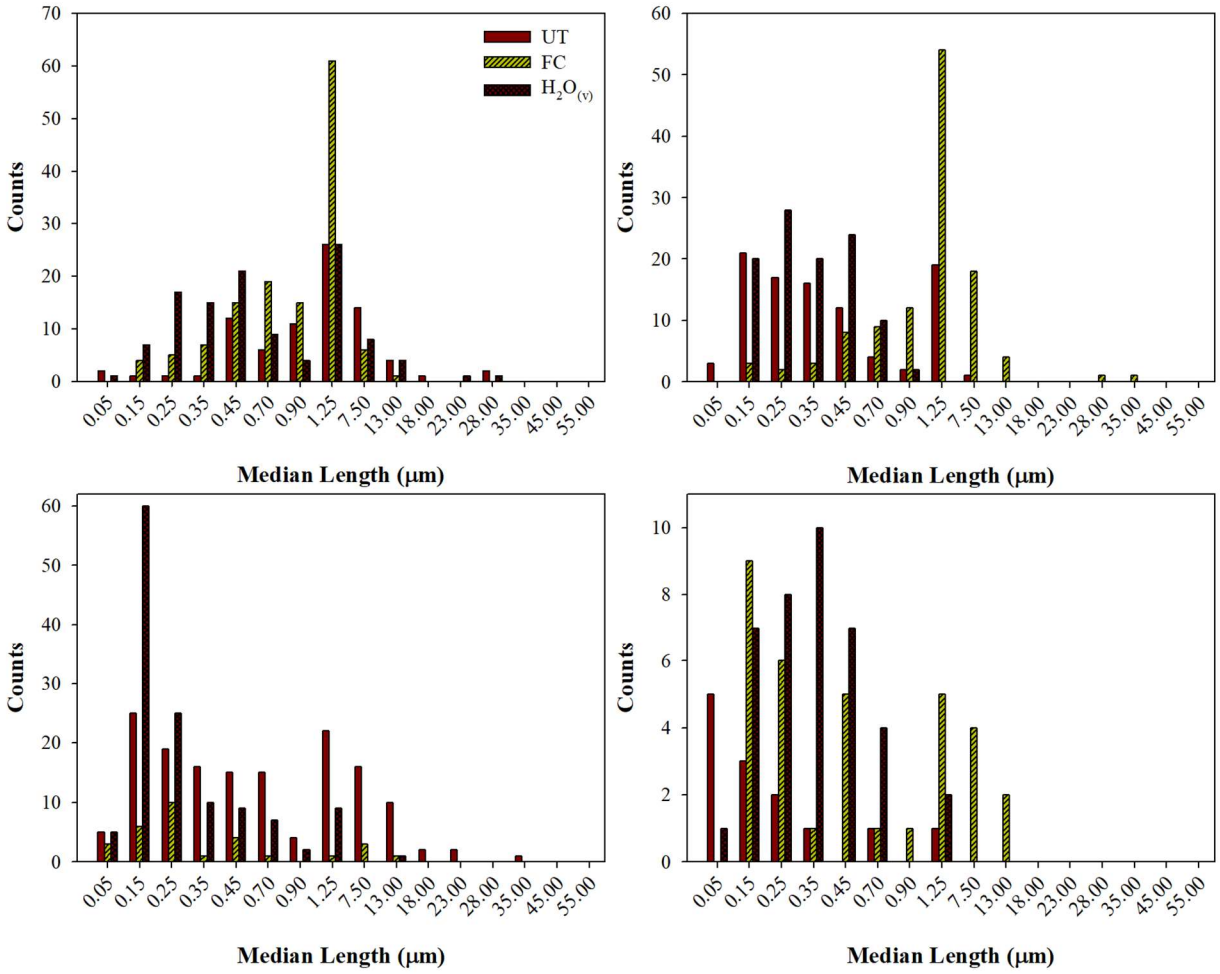

Figure 5.9. Al_2O_3 agglomerates on (a – b) Tyvek® and (c – d) cotton. Agglomerates counted after (a, c) initial contamination and (b, d) shaking sample for 2 min.

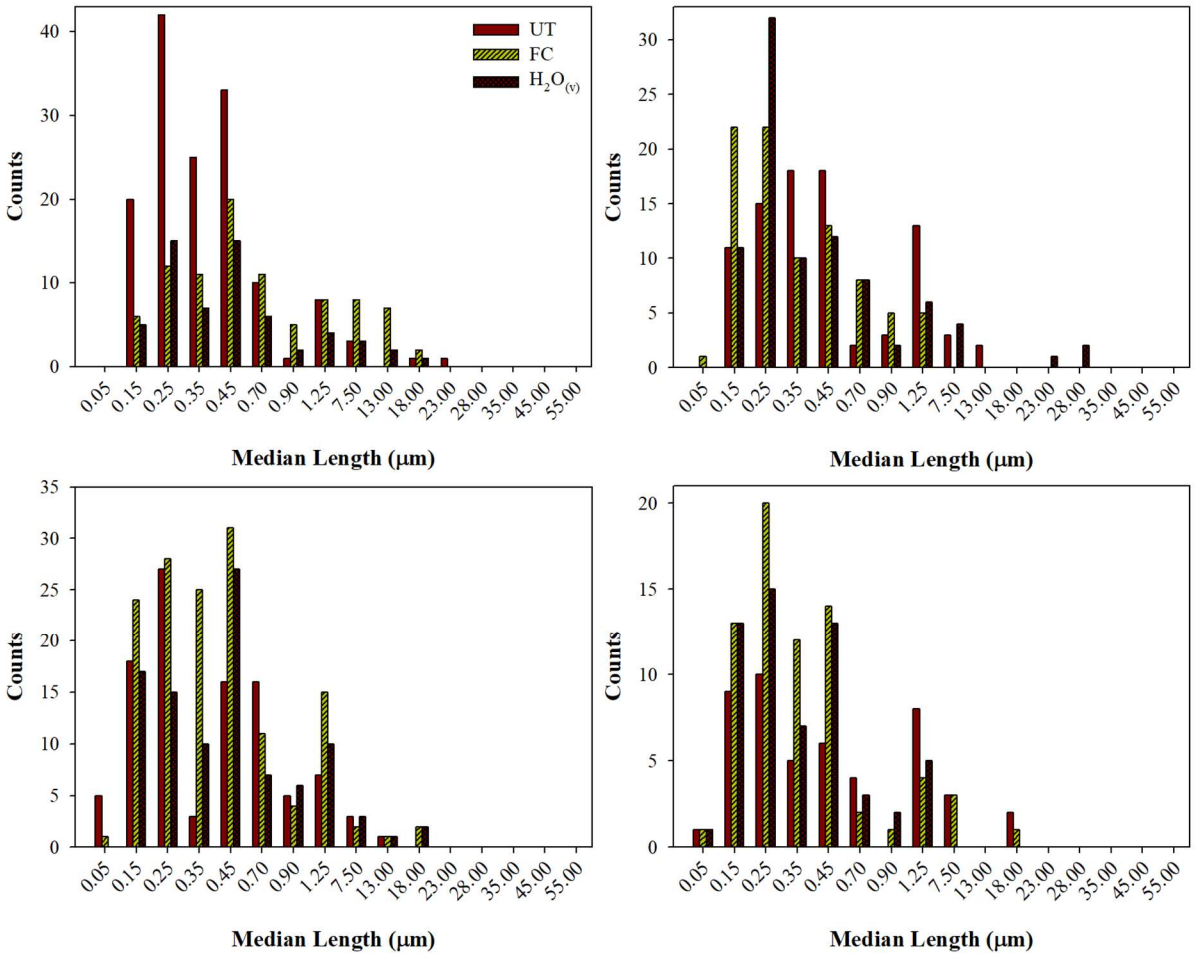

Figure 5.10. Al_2O_3 agglomerates on (a – b) blend and (c – d) PP. Agglomerates counted after (a, c) initial contamination and (b, d) shaking sample for 2 min

Table 5.5. Raw counts of Al_2O_3 agglomerates on UT and plasma treated fabrics after contamination and shaking.[a]

	Tyvek®						cotton						PP						blend					
	Contaminated			After Shaking			Contaminated			After Shaking			Contaminated			After Shaking			Contaminated			After Shaking		
Size Range	UT	FC	$H_2O_{(v)}$	UT	FC	$H_2O_{(v)}$	UT	FC	$H_2O_{(v)}$	UT	FC	$H_2O_{(v)}$	UT	FC	$H_2O_{(v)}$	UT	FC	$H_2O_{(v)}$	UT	FC	$H_2O_{(v)}$	UT	FC	$H_2O_{(v)}$
1-100nm	2	0	1	3	0	0	5	3	5	5	0	1	5	1	0	1	1	1	0	0	0	0	1	0
101-200nm	1	4	7	21	3	20	25	6	60	3	9	7	18	24	17	9	13	13	20	6	5	11	22	11
201-300nm	1	5	17	17	2	28	19	10	25	2	6	8	27	28	15	10	20	15	42	12	15	15	22	32
301-400nm	1	7	15	16	3	20	16	1	10	1	1	10	3	25	10	5	12	7	25	11	7	18	10	10
401-600nm	12	15	21	12	8	24	15	4	9	0	5	7	16	31	27	6	14	13	33	20	15	18	13	12
600-800nm	6	19	9	4	9	10	15	1	7	1	1	4	16	11	7	4	2	3	10	11	6	2	8	8
800nm-1um	11	15	4	2	12	2	4	0	2	0	1	0	5	4	6	0	1	2	1	5	2	3	5	2
1um-5um	26	61	26	19	54	0	22	1	9	1	5	2	7	15	10	8	4	5	8	8	4	13	5	6
5um-10um	14	6	8	1	18	0	16	3	0	0	4	0	3	2	3	3	3	0	3	8	3	3	0	4
11um-15um	4	1	4	0	4	0	10	1	1	0	2	0	1	1	1	0	0	0	0	7	2	2	0	0
16-20um	1	0	0	0	0	0	2	0	0	0	0	0	0	2	2	2	1	0	1	2	1	0	0	0
21-25um	0	0	1	0	0	0	2	0	0	0	0	0	0	0	0	0	0	0	1	0	0	0	0	1
26-30um	2	0	1	0	1	0	0	0	0	0	0	0	0	0	0	0	0	0	0	0	0	0	0	2
31-40um	0	0	0	0	1	0	1	0	0	0	0	0	0	0	0	0	0	0	0	0	0	0	0	0
41-50um	0	0	0	0	0	0	0	0	0	0	0	0	0	0	0	0	0	0	0	0	0	0	0	0
51-60um	0	0	0	0	0	0	0	0	0	0	0	0	0	0	0	0	0	0	0	0	0	0	0	0
Total #	**81**	**133**	**114**	**95**	**115**	**104**	**152**	**30**	**128**	**13**	**34**	**39**	**101**	**144**	**98**	**48**	**71**	**59**	**144**	**90**	**60**	**85**	**86**	**88**

[a]All measurements made for an n = 2 fabric samples.

$H_2O_{(v)}$ cotton had significant decreases after shaking (Fig. 5.9 c – d), but the FC cotton had the lowest amount of Al_2O_3 after contamination and relatively the same amount after shaking. Thus, if working with Al_2O_3 NP or similar materials, the FC cotton fabric potentially has the lowest contamination level and risk for secondary exposure. For the blend and PP fabrics (Fig. 5.10), the counts after shaking appear to be independent of treatment type. Previous work from the Tsai group studied the interaction of Al_2O_3 with UT cotton blend, Tyvek®, and polyester.[6] Although they used somewhat different fabrics, the results presented here are similar such that the cotton blend had higher contamination and release when compared to the Tyvek®.

From the McDonagh *et al.* studies, our work supports their observation that the number of particles released increases as the size of the particles increases.[8] The data presented here, however, also seem to contradict their finding that the tightness/pattern of the fabric is the sole influencing factor on ENP adhesion.[7] If this were the case, we would expect to observe the cotton and blend with similar counts before and after shaking, whereas the PP and Tyvek® have a majority of ENP released after shaking. In addition, there would not be significant differences between the behavior of the UT and plasma treated samples for a given fabric. Thus, the type and surface chemistry of the material must have some effect on ENP attachment and release.

Finally, Table 5.5 lists the numbers of individual and bundled CNT. These results were reported without a size distribution due to the irregular shape of the agglomerates not allowing for a representative diameter to be determined. Samples were only imaged after shaking, so comparison of the amount before and after shaking cannot be performed. From these data, Tyvek® has the most CNT remaining after shaking, followed by the blend, then cotton, and finally the PP. In general, the FC samples have the largest number of bundles, whereas the UT samples have the most individual CNT. This observation supports the result in the Al_2O_3 and

Table 5.6. Total number of CNT after shaking.[a]

Plasma Precursor Gas	Material	Total # CNT Bundles	Total # Individual CNT
UT	PP	61	25
	Tyvek®	156	248
	blend	160	45
	cotton	103	11
C_3F_8	PP	86	24
	Tyvek®	214	174
	blend	281	39
	cotton	151	59
$H_2O_{(v)}$	PP	35	28
	Tyvek®	131	53
	blend	145	7
	cotton	63	0

[a]All measurements made for an n = 2 fabric samples.

carbon black studies and suggests the material's surface chemistry cannot be ignored when studying these samples ENP adhesion and resuspension characteristics.

As a direct comparison of ENP attachment and release, SEM images were taken at the same spot before and after shaking the PP. This fabric was selected as it has easily identifiable landmarks on the material, allowing for confidence that the areas imaged were the same, despite removing the sample from the instrument to perform the shaking experiments. In Figure 5.11, SEM images of the ENP-contaminated UT PP are shown before and after shaking. Because of the Au coating required for imaging these samples, distinct dark spots where ENP fell off can be seen in the image. As observed with the agglomerate counts, the larger ENP easily fall off after shaking. The red circles in Figure 5.11 highlight some areas where ENP were displaced from elsewhere and have reattached. This reattachment may be beneficial as it can serve as an alternative method to prevent secondary nanomaterial exposure. Figure 5.12 shows the same spot imaging of the FC PP samples contaminated with carbon black and CNT. These images also show dark spots where the ENP have fallen off or relocated after shaking. However, these FC samples do not have as many ENP released after shaking as seen with the UT materials.

The number and size distribution of the aggregates counted in these same spot images are plotted in Figure 5.14. For most agglomerates, shaking the UT PP (Fig. 5.14a and c) results in ~50% reduction of ENP. This behavior is also observed with the FC PP contaminated with carbon black. With the FC PP, the CNT counts do not show as significant of a decrease after shaking, and for the smaller clusters, the counts increase. This indicates that even though the CNT is moving around on the fabric, the CNT are still adhering to the material and not completely falling off or being resuspended. This is a promising result, as the continued attachment of the CNT to the FC PP means that the ENP are not being resuspended and have a

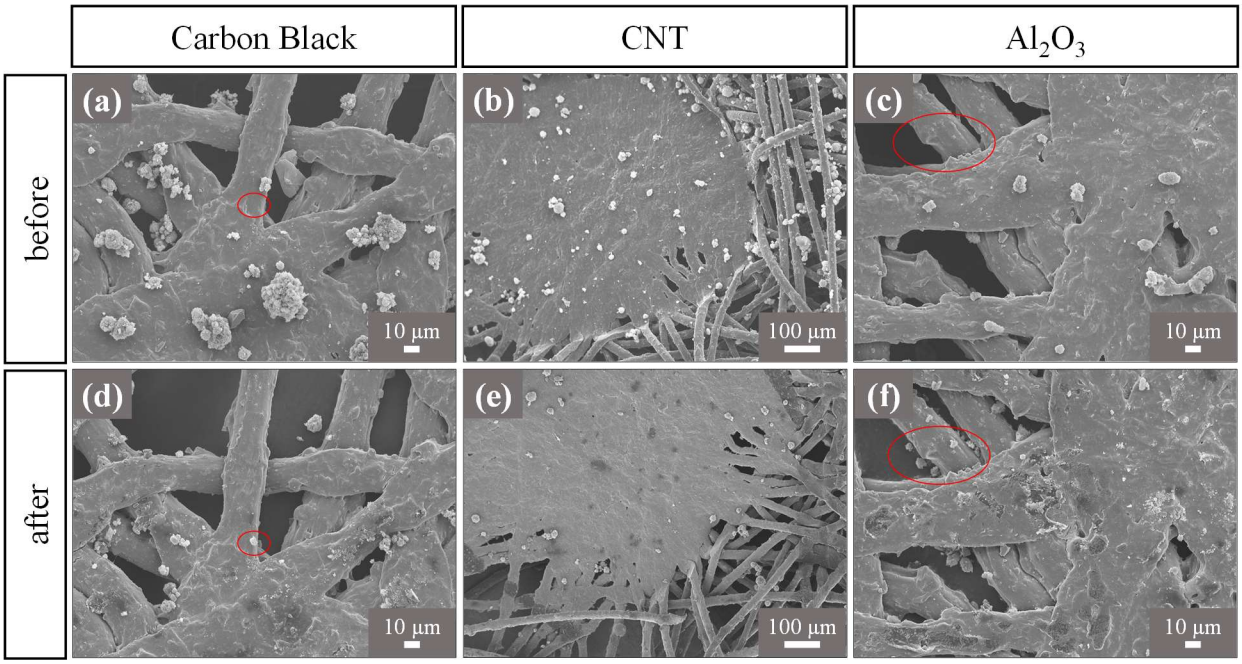

Figure 5.11. SEM images of UT PP (a – c) before and (d - f) after contamination with (a, d) carbon black, (b, e) CNT, and (c, f) Al_2O_3. Red circles indicate areas where ENP have reattached to the fabric. Images taken at (a, c, d, f) x500 and (b, e) x110 magnification.

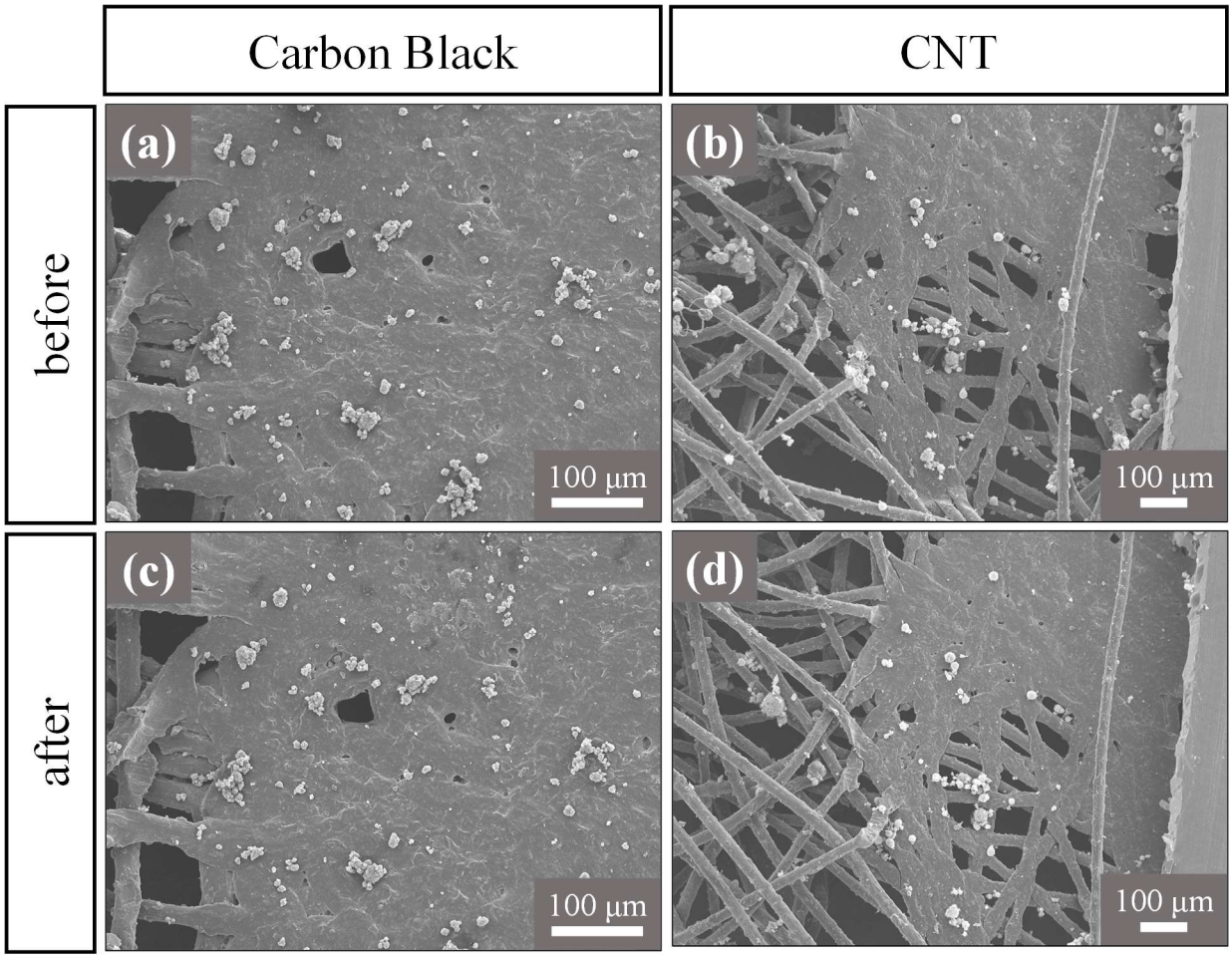

Figure 5.12. SEM images of FC PP (a – b) before and (c - d) after contamination with (a, c) carbon black and (b, d) CNT. Images taken at (a, c) x200 and (b, d) x100 magnification.

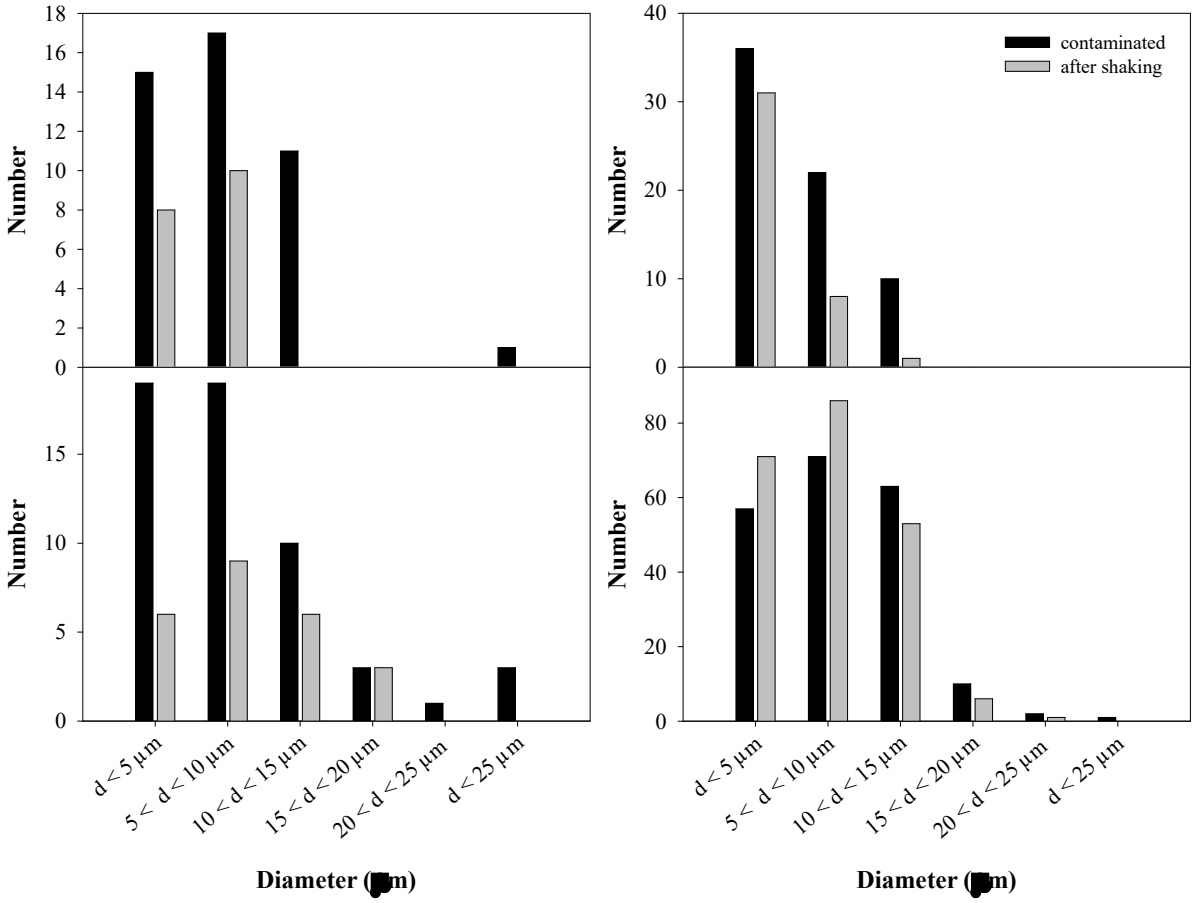

Figure 5.14. Number of (a – b) carbon black and (c – d) CNT agglomerates on (a, c) UT and (b, d) FC PP from same spot analysis. Black bars represent counts from contaminated samples and gray bars represent counts after shaking the same sample.

lower risk of being inhaled by the wearer. This study demonstrates that the deposition of a FC film altered the interaction of the CNT with the PP, suggesting that the surface chemistry of a material plays some role in the attachment and resuspension behavior of ENP. It is clear that further work is needed to analyze a larger sample size for the UT and FC PP and to do these same spot analyses on all of the fabrics to understand these interactions fully and improve PPE.

5.3 SUMMARY

The attachment and release of several ENP with four PPE fabrics were investigated to understand how different properties affect their interactions and ultimately to improve the materials by mitigating contamination or risk of secondary exposure. The surface chemistry and wettability of these fabrics was tuned using either a C_3F_8 or $H_2O_{(v)}$ plasma and monitored with XPS and WCA analysis. The C_3F_8 plasma deposited a FC coating, increasing the material hydrophobicity, whereas the $H_2O_{(v)}$ plasma implanted O-functionality and etched the surface, nominally increasing the hydrophilicity. Notably, the latter treatment ultimately resulted in a relatively permanent increase in hydrophilicity of the cotton and Tyvek®, with the other two materials exhibiting hydrophobic recovery after a month of aging. Contamination and release studies indicate that in general, agglomerates <600 μm have the highest attachment to all of the fabrics studied, and the probability of a particle being released after shaking increases as its size increases. The $H_2O_{(v)}$ materials display the lowest carbon black contamination, and the FC cotton showed the lowest contamination and resuspension amounts. Finally, the same spot SEM analysis studies reveal that displaced CNT particles on FC PP are likely to reattach elsewhere on the fabric, providing an alternative method to limiting secondary exposure. These efforts toward understanding the role of material properties on the attachment of ENP may lead to strategies for determining what type of fabric is the best for protecting the wearer from adverse health effects

from exposure to nanomaterials. Although further work is needed to optimize the hydrophilic treatments of some of the fabrics, ultimately, these data demonstrate that plasma modification is a viable route to creating improved materials for PPE.

REFERENCES

1. Singh, A. K., Chapter 1 - Introduction to Nanoparticles and Nanotoxicology. In *Engineered Nanoparticles*, Singh, A. K., Ed. Academic Press: Boston, 2016; pp 1-18.
2. Jose Varghese, R.; Sakho, E. h. M.; Parani, S.; Thomas, S.; Oluwafemi, O. S.; Wu, J., Chapter 3 - Introduction to Nanomaterials: Synthesis and Applications. In *Nanomaterials for Solar Cell Applications*, Thomas, S.; Sakho, E. H. M.; Kalarikkal, N.; Oluwafemi, S. O.; Wu, J., Eds. Elsevier: 2019; pp 75-95.
3. General Safe Practices for Working with Engineered Nanomaterials in Research Laboratories. National Insitute for Occupational Safey and Health: 2012.
4. Kan, H.; Pan, D.; Castranova, V., Engineered Nanoparticle Exposure and Cardiovascular Effects: The Role of a Neuronal-Regulated Pathway. *Inhal. Toxicol.* **2018,** *30* (9-10), 335-342.
5. Tang, C.-S.; Chuang, K.-J.; Chang, T.-Y.; Chuang, H.-C.; Chen, L.-H.; Lung, S.-C. C.; Chang, L.-T., Effects of Personal Exposures to Micro- and Nano-Particulate Matter, Black Carbon, Particle-Bound Polycyclic Aromatic Hydrocarbons, and Carbon Monoxide on Heart Rate Variability in a Panel of Healthy Older Subjects. *Int. J. Environ. Res. Public Health* **2019,** *16* (23), 4672.
6. Tsai, C. S.-J., Contamination and Release of Nanomaterials Associated with the Use of Personal Protective Clothing. *Ann Occup Hyg* **2015,** *59* (4), 491-503.
7. McDonagh, A.; Byrne, M. A., The Influence of Human Physical Activity and Contaminated Clothing Type on Particle Resuspension. *J. Environ. Radioact* **2014,** *127*, 119-126.
8. McDonagh, A.; Byrne, M. A., A Study of the Size Distribution of Aerosol Particles Resuspended from Clothing Surfaces. *J. Aerosol Sci* **2014,** *75*, 94-103.
9. Zhao, J.; Song, L.; Shi, Q.; Luan, S.; Yin, J., Antibacterial and Hemocompatibility Switchable Polypropylene Nonwoven Fabric Membrane Surface. *ACS Appl. Mater. Interfaces* **2013,** *5* (11), 5260-5268.
10. Lao, L.; Fu, L.; Qi, G.; Giannelis, E. P.; Fan, J., Superhydrophilic Wrinkle-Free Cotton Fabrics via Plasma and Nanofluid Treatment. *ACS Appl. Mater. Interfaces* **2017,** *9* (43), 38109-38116.
11. Karaman, M.; GÜRsoy, M.; AykÜL, F.; Tosun, Z.; Kars, M. D.; Yildiz, H. B., Hydrophobic Coating of Surfaces by Plasma Polymerization in an RF Plasma Reactor with an Outer Planar Electrode: synthesis, characterization and biocompatibility. *Plasma Sci Technol* **2017,** *19* (8), 085503.
12. d'Agostino, R.; Cramarossa, F.; Fracassi, F.; Illuzzi, F., 2 - Plasma Polymerization of Fluorocarbons. In *Plasma Deposition, Treatment, and Etching of Polymers*, d'Agostino, R., Ed. Academic Press: San Diego, 1990; pp 95-162.
13. Cuddy, M. F.; Fisher, E. R., Contributions of CF and CF_2 Species to Fluorocarbon Film Composition and Properties for C_xF_y Plasma-Enhanced Chemical Vapor Deposition. *ACS Appl. Mater. Interfaces* **2012,** *4* (3), 1733-1741.
14. Hanna, A. R.; Cuddy, M. F.; Fisher, E. R., Energy Partitioning and Its Influence on Surface Scatter Coefficients within Fluorinated Inductively Coupled Plasmas. *J. Vac. Sci. Technol., A* **2017,** *35* (5), 05C308.
15. Hanna, A. R.; Fisher, E. R., Tailoring the Surface Properties of Porous Zeolite Constructs Using Plasma Processing. *Microporous Mesoporous Mater.* **2020,** *307*, 110467.

16. Hawker, M. J.; Pegalajar-Jurado, A.; Fisher, E. R., Innovative Applications of Surface Wettability Measurements for Plasma-Modified Three-Dimensional Porous Polymeric Materials: A Review. *Plasma Process. Polym.* **2015,** *12* (9), 846-863.
17. Hawker, M. J.; Pegalajar-Jurado, A.; Fisher, E. R., Conformal Encapsulation of Three-Dimensional, Bioresorbable Polymeric Scaffolds Using Plasma-Enhanced Chemical Vapor Deposition. *Langmuir* **2014,** *30* (41), 12328-12336.
18. Steen, M. L.; Hymas, L.; Havey, E. D.; Capps, N. E.; Castner, D. G.; Fisher, E. R., Low Temperature Plasma Treatment of Asymmetric Polysulfone Membranes for Permanent Hydrophilic Surface Modification. *J. Membr. Sci.* **2001,** *188* (1), 97-114.
19. Steen, M. L.; Butoi, C. I.; Fisher, E. R., Identification of Gas-Phase Reactive Species and Chemical Mechanisms Occurring at Plasma−Polymer Surface Interfaces. *Langmuir* **2001,** *17* (26), 8156-8166.
20. Tompkins, B. D.; Dennison, J. M.; Fisher, E. R., Etching and Post-Treatment Surface Stability of Track-Etched Polycarbonate Membranes by Plasma Processing Using Various Related Oxidizing Plasma Systems. *Plasma Process. Polym.* **2014,** *11* (9), 850-863.
21. Tompkins, B. D.; Fisher, E. R., Evaluation of Polymer Hydrophobic Recovery Behavior Following H_2O Plasma Processing. *J. Appl. Polym. Sci.* **2015,** *132* (20).
22. Iriyama, Y.; Yasuda, T.; Cho, D. L.; Yasuda, H., Plasma Surface Treatment on Nylon Fabrics by Fluorocarbon Compounds. *J. Appl. Polym. Sci.* **1990,** *39* (2), 249-264.
23. Zhou, X.; Zhang, Z.; Xu, X.; Guo, F.; Zhu, X.; Men, X.; Ge, B., Robust and Durable Superhydrophobic Cotton Fabrics for Oil/Water Separation. *ACS Appl. Mater. Interfaces* **2013,** *5* (15), 7208-7214.
24. Gao, L.; McCarthy, T. J., Teflon is Hydrophilic. Comments on Definitions of Hydrophobic, Shear versus Tensile Hydrophobicity, and Wettability Characterization. *Langmuir* **2008,** *24* (17), 9183-9188.
25. Steen, M. L.; Jordan, A. C.; Fisher, E. R., Hydrophilic Modification of Polymeric Membranes by Low Temperature H_2O Plasma Treatment. *J. Membr. Sci.* **2002,** *204* (1), 341-357.
26. Holc, M.; Zaplotnik, R.; Mozetic, M.; Vesel, A., Surface Modification and Aging of Polyacrylonitrile Butadiene Styrene Polymer Induced by Treatment in RF Oxygen Plasma. *IEEE Trans. Plasma Sci.* **2018,** *46* (10), 3669-3676.

CHAPTER 6

EXPLORATION OF OTHER NANO- AND MICRO-SIZED MATERIALS FOR SENSOR AND ENERGY STORAGE APPLICATIONS

This chapter describes the fabrication and characterization of several nano- and micro-sized materials targeted as potential nanoscale sensors. Preliminary sensing data using the MO on both paper and ZrO_2 substrates are presented to demonstrate the applicability of these materials as gas sensors. In addition, expansion of proof-of-concept work performed by Ms. Zoe Mann is included. These studies focus on the growth of vertically aligned graphene nanosheets (VGN), primarily through the lens of troubleshooting fabrication parameters and a thorough literature review of VGN growth utilizing plasmas. Specific acknowledgments for this section include Steven Marquez for performing the SEM characterization during limited instrument access resulting from COVID-19 restrictions and Ms. Zoe Mann for helpful discussions about her work with the VGN materials. This work was supported by funding from the National Science Foundation (NSF CBET – 1803067).

6.1 Introduction

Although SnO_2 is one of the most commonly studied and used commercial gas sensor materials, other semiconducting metal oxides (SMO) such as ZnO, TiO_2, and WO_3 are also being explored as potential alternatives.[1-2] All work in Chapters 3 and 4 was done using only commercially available SnO_2 nanoparticles (NP). Examining alternate SMO materials and morphologies paired with plasma treatments, provides a much wider range of options for determining the best material to detect a specific gas. Previous work in our group, compared the

sensing performance of untreated (UT) and plasma treated SnO_2 NP and nanowires (NW).[3] Although the NW have higher exposed surface area (and thus, theoretically more material for the gases to interact with), the NP generally had higher responses to CO and benzene, indicating that direct comparisons of these materials are needed to fully optimize gas detection. As discussed in Chapter 4, the sensor operating temperature (T_S) is vital to the reactivity of the material and therefore the response to a target gas. This, however, is a unique challenge for multi-gas detection with a single type of SMO, as it would require each gas's sensor to be held at different T_S to avoid cross-detection. Alternative SMO may be useful, particularly for multi-gas detection utilizing a design that could contain multiple SMO sensors. With this configuration, one could imagine that each material demonstrates preferential sensing for a specific gas while the entire device is held at a constant temperature.

In addition, expanding on the work presented in Chapter 4, by directly growing these materials onto a paper substrate, the amount of surface area available for gas molecules to interact with is greatly increased. As seen in Figure 6.1a and SEM images in Figure 4.2 c – f, when NP are dropcast onto the paper substrate, the NP do not encapsulate the individual fibers in a monolayer, resulting in more of a blanket-like coating. Thus, if the SMO were to be grown directly on the substrate, a more conformal coating could be achieved, allowing paper fibers throughout the entire thickness of the substrate to be utilized. The simplest form of this involves deposition of a thin film (TF) (Fig. 6.1b) followed by growing nanostructures on the paper (Fig. 6.1c). With conventional chemical vapor deposition (CVD) growth methods typically requiring $T_S \geq 300$ °C (specifically 700 °C for the NW growth done in our lab),[3-5] this synthetic route cannot be used with paper substrates. Instead, sonochemical[6] and hydrothermal[7] methods were adapted to be compatible with the paper substrate and equipment in our laboratory.

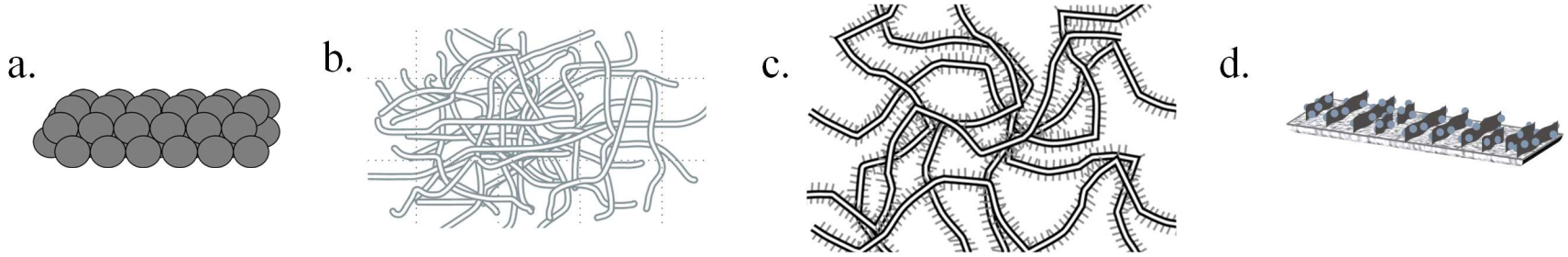

Figure 6.1. Simplified schematic of possible MO constructs for sensing materials: (a) drop cast NP, (b) thin films grown on paper, (c) microrods grown on paper, and (d) composite MO/VGN grown on Ni foam. Materials are ordered in increasing amount of exposed surface area.

Composite SMO and graphene-based sensors represent another type of material gaining attention.[8-10] Like SMO sensors, graphene is a p-type semiconductor and adsorption of gas onto the surface results in observable conductance changes.[11] Thus, combining n-type semiconductors (like SnO_2 and ZnO) with graphene and forming a p-n heterojunction enhances the conductivity of the graphene, resulting in an increased sensor response.[12] In addition, SMO decoration of graphene structures is thought to increase the number of possible sites for gas adsorption.[12] Similar to the benefits of using a paper supporting substrate, discussed in Chapter 4, by attaching the SMO onto the VGN, more of the surface of the metal oxide is exposed when compared just having the SMO supported on a flat substrate. As this process is complicated, further work is needed to better understand the interaction of the gas with the surface of the composite material and the resulting sensor behavior and performance.

Graphene and composite SMO-graphene are also commonly studied materials for energy storage applications.[13-16] In particular, vertical graphene nanosheets (VGN) are of special interest for supercapacitor materials due to their high surface area. Perhaps more importantly, the orientation of the VGN allows for enhanced electron transport when compared to other morphologies employed in supercapacitors. Similar to gas sensor materials, large accessible surface area is important for supercapacitor applications as it allows for more interaction with electrolyte ions, thereby increasing the material's capacitance. Other beneficial properties of VGN and composite VGN materials for energy storage is discussed in Appendix A. Overall, the work presented in this chapter on the synthesis and characterization of these materials complements findings from previous chapters and provides a potential path for future work with these projects.

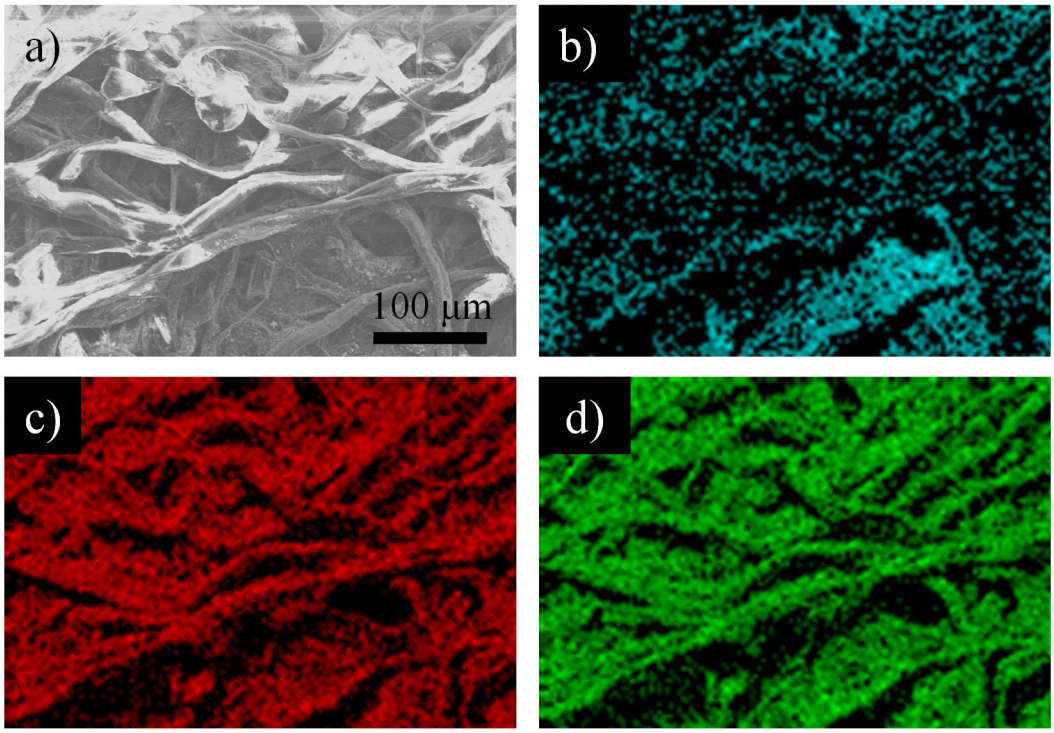

Figure 6.2. (a) SEM image and corresponding EDS elemental composition maps of (b) Zn, (c) C, and (d) O at x250 magnification for the ZnO NP PGS.

6.2 Results and Discussion

As a direct comparison to earlier studies, ZnO NP PGS were fabricated using the same dropcast method. Similar to images shown in Figure 4.1, EDS elemental maps (Fig. 6.2) show the presence of elements corresponding to the paper substrate and the NP. Note that the distribution of Zn looks to be relatively uniform over the entirety of the sample spot, indicating good coverage of the paper substrate with the NP. As we found with the UT SnO_2 PGS, the resistance of the UT ZnO PGS was too high to measure with the current sensing system; thus, we made UT sensors utilizing ZrO_2 wafers as the supporting substrate. Figure 6.3 shows the response of these sensors to ethanol (EtOH) and CO. At these low T_S, the response of the UT sensors was < 1, demonstrating that effective detection of these gases cannot be achieved with the UT ZnO PGS.

We were, however, able to effectively treat the ZnO PGS with Ar/O_2 plasmas and perform preliminary sensor measurements. Figure 6.4 displays the CO response of P = 45 and 60 W Ar/O_2 plasma treated ZnO PGS. Clearly, plasma treatment increased the response to CO when compared to the UT sensors, with the largest response resulting from the 60 W treatment. We hypothesize that the Ar/O_2 plasma treatment likely etches O from the SMO lattice allowing for increased O adsorption and enhanced sensor response, similar to our observations with the SnO_2 PGS.

As noted above, one of the limitations to the dropcast methodology is that we do not achieve a conformal coating of the NP on the paper substrate. Thus, we also attempted to conformally grow SnO_2 directly onto the paper substrate utilizing a sonochemical method adapted to deposit a SnO_2 TF.[6] After the 6 hr sonication, the 0.3 g samples of paper increased in mass by ~0.05 g, and the growth solution turned opaque, both indications that some sort of

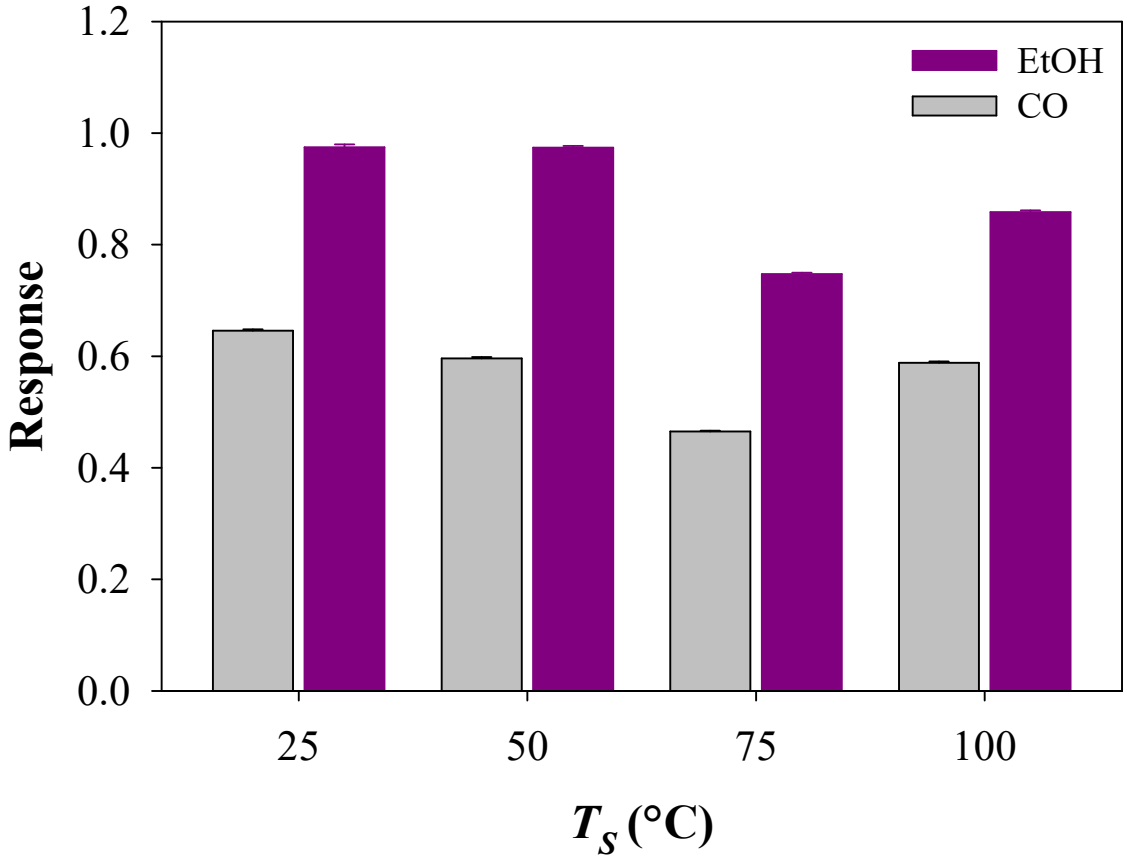

Figure 6.3. Response of UT ZnO NP on ZrO_2 wafer to EtOH and CO gas exposure.

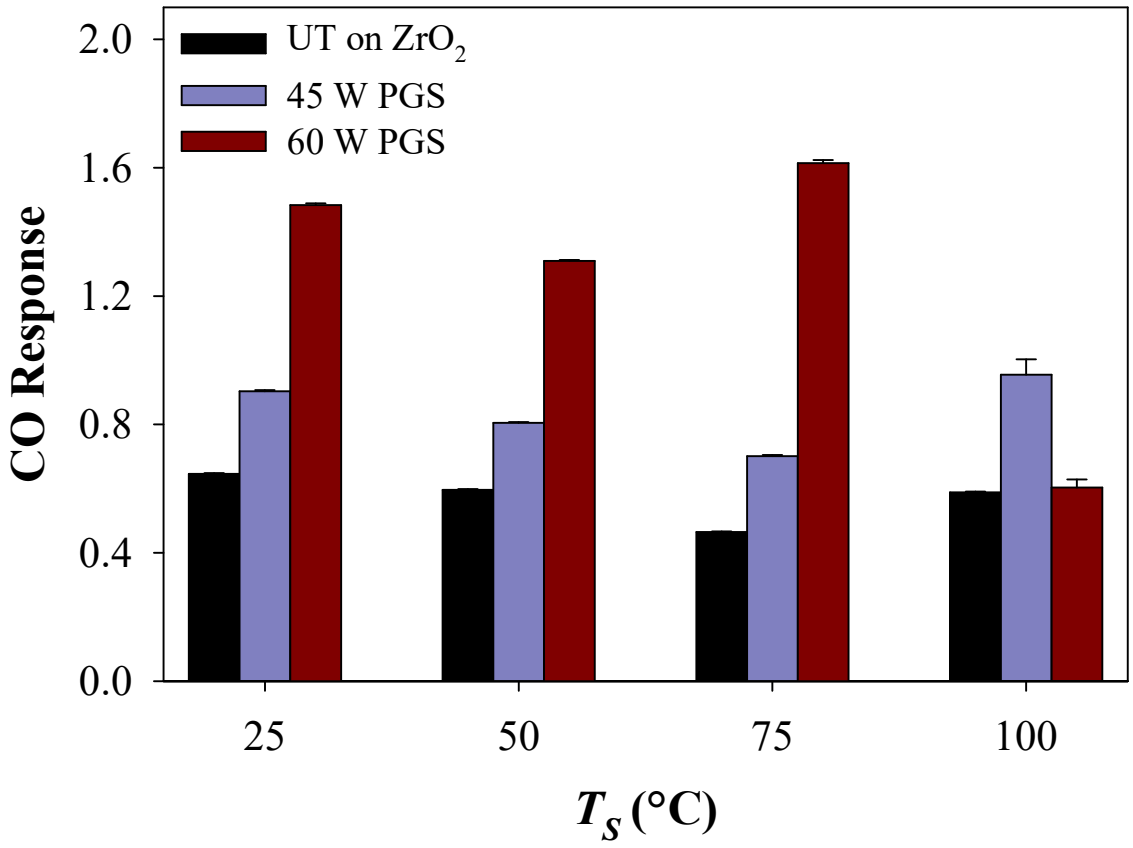

Figure 6.4. CO response data for UT ZnO NP on ZrO_2 wafer and Ar/O_2 plasma treated ZnO PGS (p = 140 mTorr, with either P = 45 W or 60 W).

material growth occurred. These samples were then analyzed using XRD and XPS. Notably, only a broad peak at ~22° corresponding to the paper substrate appeared in the XRD pattern, with no distinct SnO_2 peaks (Fig. 6.5). This technique, however, analyzes the bulk of the sample (sampling depth on the μm scale), so it is possible that a TF of SnO_2 was synthesized on the paper and is too thin to be detected with XRD. Given that the goal of the sonochemical method was to implant a more conformal, and arguably thinner layer of the metal oxide, we also performed XPS analysis to potentially capitalize on its shallower sampling depth. The survey spectrum in Fig. 6.6a reveals the expected peaks attributed to Sn, O, and C, along with very small Cl peaks. The Cl contamination most likely arises from starting reagent not rinsed off after the sonication step.

Representative high-resolution spectra for Sn, O, and C are shown in Figure 6.6b – d, along with theoretical fits to determine elemental composition of the samples (Sn: 28.6 ± 1.2%; O: 37.0 ± 2.8%; and C: 34.4 ± 4.0%). The significant presence of C indicates we are likely sampling the underlying paper this as well as any adventitious C that might be present. Typically, XPS is analyzes the top ~10 nm of the sample, therefore the TF must be <10 nm as it can be detected but with a significant signal from the underlying substrate. Although the thinness of the film is promising for conformal coating, further work is needed to determine if this is the case with these samples. One strategy to do this would be to burn off the paper by calcinating the sample (the original method determined 500 °C for 5 hr to remove a cotton substrate) and imaging the product.[6] If structures that resemble hollow tubes are left, this is a good indicator that this method was successful in depositing a conformal coating of SnO_2 on the paper.

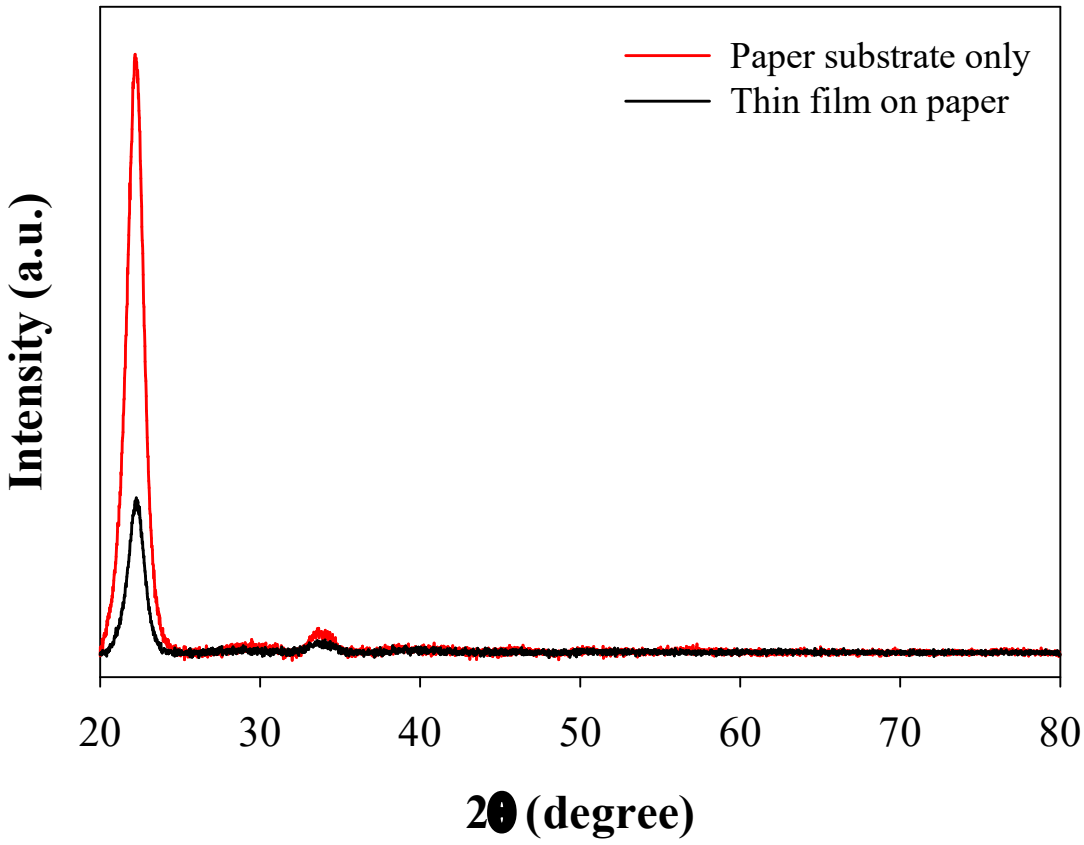

Figure 6.5. PXRD pattern of ZnO µrods grown on paper.

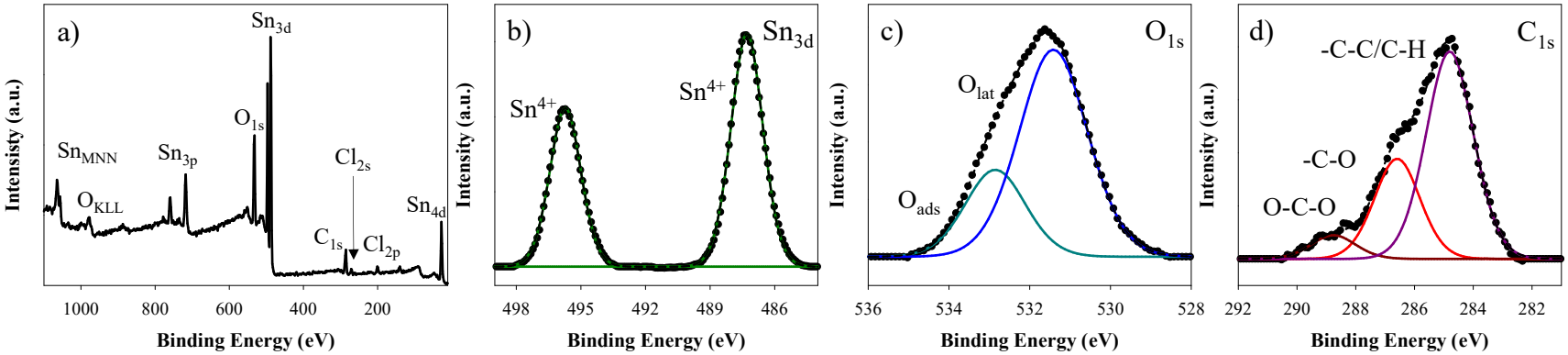

Figure 6.6. XPS (a) survey and high resolution (b) Sn_{3d}, (c) O_{1s}, and (d) C_{1s} spectra of the SnO_2 TF grown on paper. Inset labels correspond to fitted binding environment assignments.

From the O_{1s} spectrum, peaks corresponding to lattice O (O_{lat}) and adsorbed O (O_{ads}) are present in a ratio of 3.2, similar to the O_{lat}/O_{ads} of the UT SnO_2 NP (see Table 4.1). This similarity suggests this SnO_2 PGS will behave similarly to the UT SnO_2 NP PGS, and will be unlikely to detect any of the target gases at $T_S \leq 100$ °C. Nevertheless, preliminary sensor measurements were attempted. Several approaches were employed to determine if the response of the SnO_2 TF sensors could be measured. Initially, the SnO_2 TF on the plain paper substrate was placed in the sensing chamber for measurements; however, the resistance of these materials was greater than the upper limit of the multimeter (1200 MΩ). In the second approach, these samples were treated with an Ar/O_2 plasma (p = 140 mTorr, P = 15 W) to try to lower the material resistance (similarly to what we observed with the SnO_2 NP PGS). Unfortunately, the fabricated SnO_2 TF sensors still overloaded the instrument. Finally, the TF growth was repeated on the paper containing the screen-printed electrodes. For these more complex substrates, we found that the sensor needed to be partially submerged in the growth solution (see Fig. 2.1) and a plain strip of paper added to the back of the sensor to ensure that the material being analyzed was actually located between the interdigitated electrodes as opposed to just measuring the shortest path between the alligator clips.

This approach resulted in some success. Indeed, these composite sensors had a measurable and somewhat stable resistance of ~150 – 180 MΩ. Nevertheless, when the air flow was turned on (represented by the solid green line in Figure 6.7), the sensor's resistance rapidly increased (from ~160 to ~580 MΩ). During this trial, the T_S was increased from 25 to 100 °C (indicated by the red arrow in Fig. 6.7). Initially, the resistance quickly decreased as expected; however, this behavior did not persist and instead the resistance increased at a faster rate until ultimately overloading the instrument. Although it is difficult to determine what exactly was

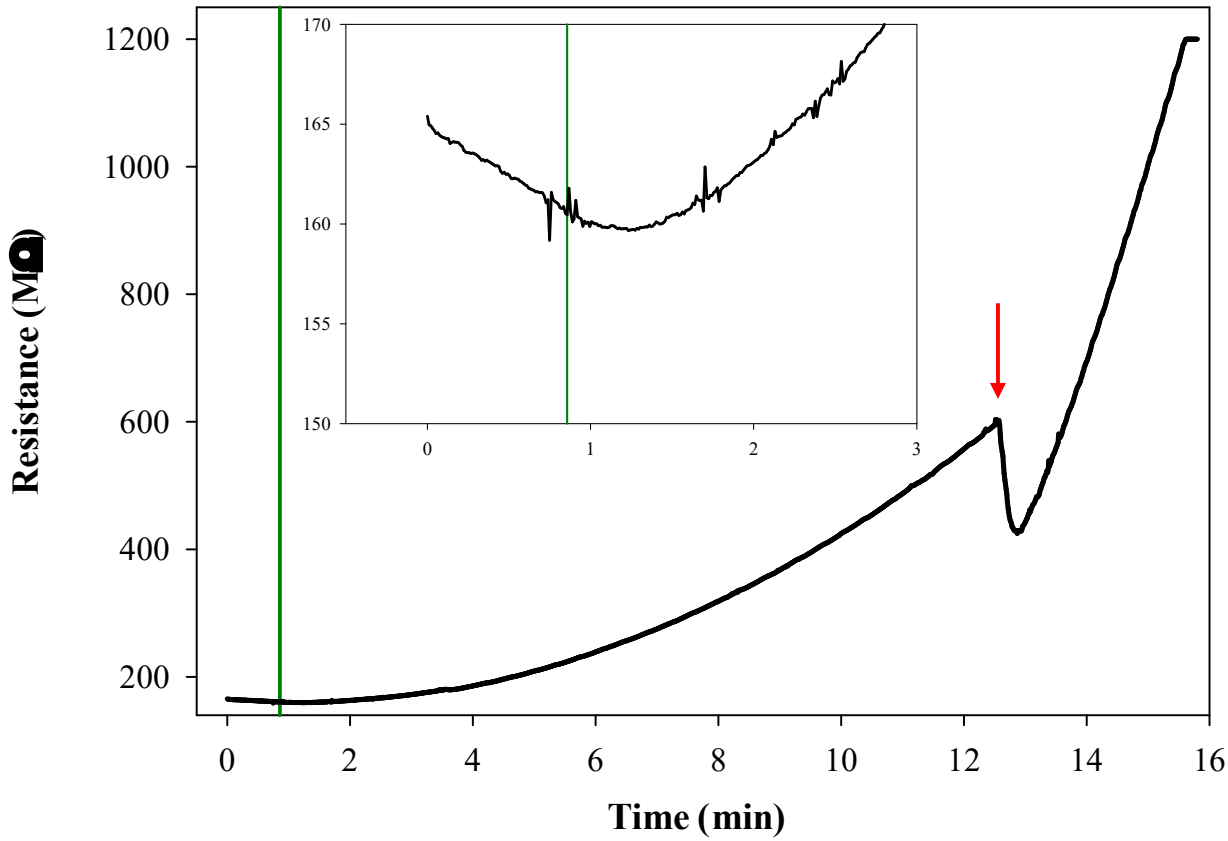

Figure 6.7. Raw resistance in air of a UT SnO_2 TF PGS. The solid vertical green line represents when air flow was turned on and the red arrow indicates when T_s was increased to 100 °C. Inset plot is an expanded view of 0 – 3 min in the sensing experiment.

happening during these trials, one possible explanation may be that there was too much O_2 adsorbing onto the sensor with the constant flow of air. O_2 generally has an oxidizing interaction with SnO_2 that results in an increase in material resistance. Thus, when there is a fixed amount of O_2 interacting with the sensor (i.e., when no air is flowing through the sensing chamber) the resistance is relatively stable. In contrast, when a steady supply of O_2 is available (i.e., air flow is turned on) potential absorption sites are no longer the limiting factor (due to the increased material surface area) and the continuous O_2 adsorption raises the material resistance. Clearly, further work is needed to optimize gas sensing experiments to ensure the resistance of these sensors can be measured and to better understand what is happening at the material surface. For example, lowing the flow rate may alleviate this issue. The studies presented in this work used a flow rate of 25 sccm for all of the gases as this was the lowest rate that the mass flow controllers could achieve. By adding a pump to the system, the flow rate can be lowered, allowing for less O_2 interacting with the SMO and potentially a measurable resistance of the SnO_2 TF.

Another method briefly explored to grow MO sensor material directly onto a paper substrate hydrothermally synthesizes ZnO microrods (μrods). Figure 6.8a shows a representative XRD pattern of the ZnO on paper with labeled diffraction peaks. SEM images of the μrods (Fig, 6.8b) clearly display well-formed rods that strongly resemble the structures grown in the original report of this methodology.[7] In addition, the inset photo of the paper substrate after growth demonstrates that macroscopic coverage of the substrate can easily be seen without the aid of magnifying instrumentation.

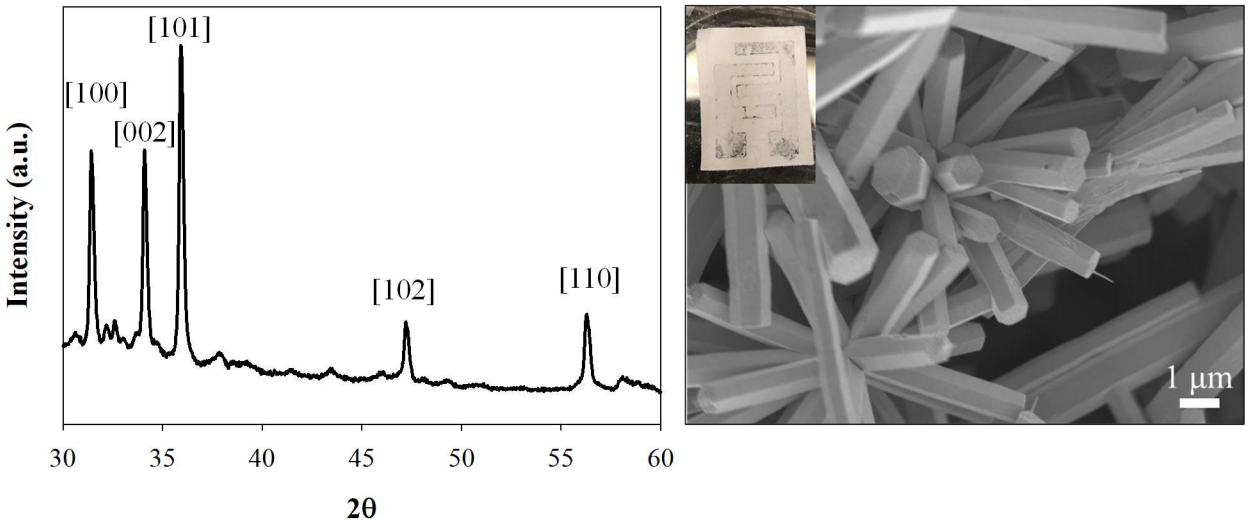

Figure 6.8. (a) XRD pattern with labeled diffraction peaks and (b) SEM image of ZnO μrods grown on paper. Inset photo is of the PGS after μrod growth.

Although these microrods nominally have a lower surface area to volume ratio than their nanoparticle counterparts, they may still display superior gas sensing performance. The CO response of the ZnO μrods on the ZrO_2 wafer is reported in Figure 6.9 (UT ZnO NP included for comparison). For most of the T_S tested, the μrods had a larger response to CO when compared to the NP. This result is somewhat unexpected as nanomaterials are generally thought to be more reactive due to their higher surface area to volume ratio when compared to micro or even bulk materials. The higher reactivity should result in more gas-SMO interactions and a higher observed response to the CO.

Although morphology may play a role in this result, the quality of the ZnO cannot be dismissed. The commercially available ZnO NP used in this study have a manufacturer reported purity of 97% with Al as the dopant. As noted in the Section 6.1, sometimes composite materials can have a synergistic effect and increase the performance when compared to the individual materials.[10] Here, however, it appears that the addition of Al could be suppressing some of the response to CO when compared to the in-lab grown μrods that reportedly have minimal surface contamination.[7] It is promising that the ZnO μrods have the largest response to CO at 25 °C, suggesting these could be a useful material for room temperature gas sensors. Unfortunately, at all other T_S examined, both ZnO sensors have a CO response <1, demonstrating that these UT materials still need to be optimized for low temperature detection of gases.

Following the morphology schematic of MO constructs presented in Figure 6.1, the last type of material investigated was VGN and MO/VGN grown on Ni foam. Although both materials could be used as a gas sensor, this work was originally started as a continuation and confirmation of another Fisher group member's project. Briefly, solid precursors (butter and

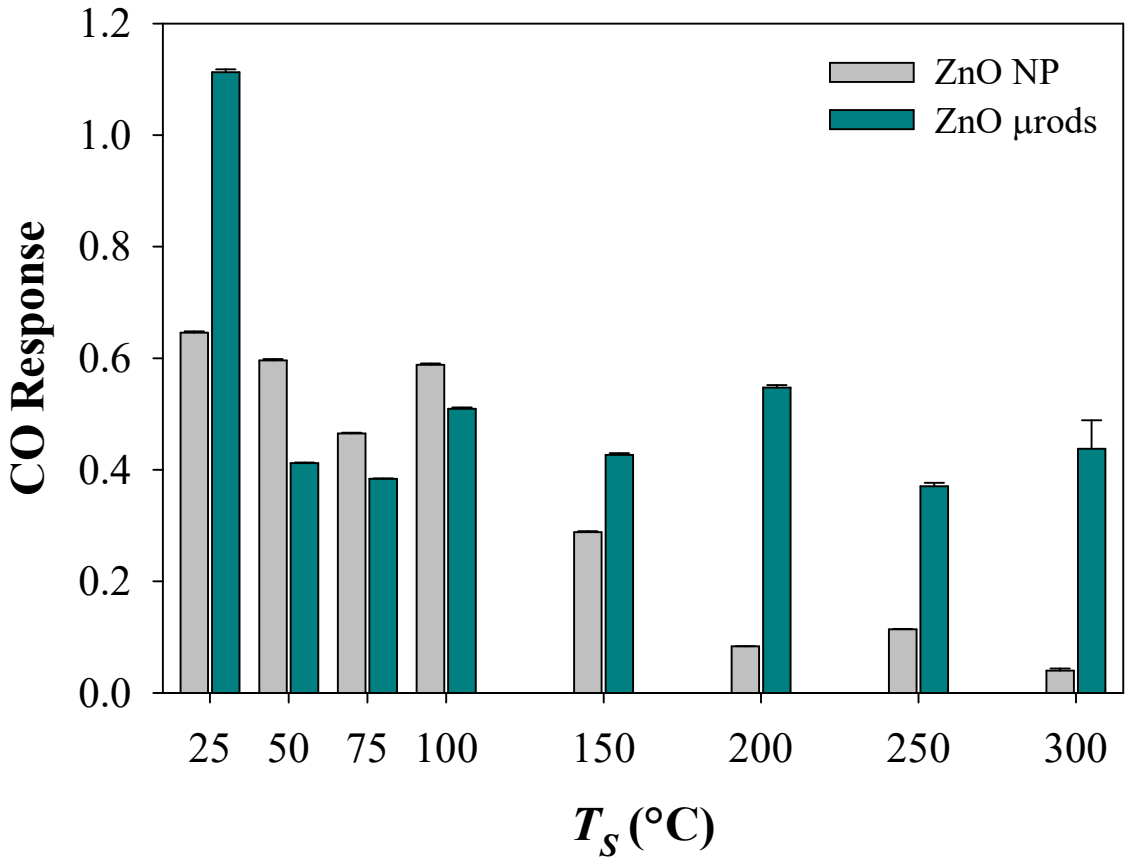

Figure 6.9. CO response of UT ZnO NP and µrods on a ZrO_2 wafer as a function of T_S.

coconut oil) were applied directly to Ni foam and a pulsed Ar plasma was used to convert the precursor to VGN in a process adapted from previously reported studies.[17-18] The key feature of these studies was the use of a pulsed plasma rather than a continuous wave plasma. Pulsing the plasma ultimately provides a lower temperature environment for the synthesis, nominally requiring lower energy costs as well. Preliminary synthesis and material characterization of the Ni foam and UT coconut oil performed by Ms. Zoe Mann is discussed in Appendix A. The experimental details for the growth of the VGN and MO/VGN samples can be found in Section A.3.

Initially, when beginning this process, I started with coconut oil as the precursor (because most of the previous work was done using butter) and used a smaller sample holder (Fig. 6.10) to resolve some of the coupling and reflective power issues observed when recreating Ms. Mann's work. The use of the smaller holder also allowed for treatment of two samples while keeping sample placement within the coil consistent. In contrast, the larger sample holder spread three samples throughout the length of the reactor coil, potentially introducing inconsistencies in the resulting materials. Previous work in our group demonstrates that this sample placement is critical to control as gas-phase species and resulting material properties change throughout the length of the reactor.[19-20] Although the reflective power on the rf power supply was lowered to <10 W, the persisting coupling within the reactor resulted in the plasma "bright spot" not being in the coil (where the samples were placed), but instead appeared downstream by the exhaust arm. This was detrimental to the plasma conversion process, as demonstrated by the vast difference in sample color shown in Figure 6.10. Other efforts to eliminate the coupling included (1) adding additional grounding straps, (2) lowering p, and (3) using a range of sample placements along the reactor. I also returned to using butter as the solid precursor. The primary

Figure 6.10. Photographs of two sample holders (center); and VGN samples resulting from the larger sample holder (left) and smaller sample holder (right).

motivation for the switch in precursor was its higher melting temperature compared to coconut oil, anticipating that this would help the precursor remain on the Ni foam instead of melting off and onto the sample holder and reactor walls. As seen in Figure 6.11, the sample clearly demonstrates that no VGN were formed at these parameters.

Much of the work performed on this project entailed a range of different troubleshooting activities. For example, previous work in our lab noted that successful growth was consistently observed when using a "dirty" reactor (generally described as having film deposition from earlier treatments not removed from the reactor walls) and substrates without any butter on them. This is a process that more closely resembles plasma-enhanced CVD (PE-CVD) rather than the plasma conversion that was reported in the literature. Briefly, what we believe was occurring in these instances is that the plasma activated/removed the previously deposited film from the walls of the reactor and formed carbon-containing radicals that are often identified as being vital species in VGN growth.[21-23] These radicals can then be deposited onto the substrate leading to the formation of VGN.

To make this process more reproducible, an alternate approach was tested. Specifically, a clean reactor was used and a series of two plasma exposures (gas flow: 5 min → plasma on: 10 min → gas flow: 5 min → plasma on: 10 min → gas flow: 5 min) was employed to replicate in a more controllable fashion the ad hoc process occurring in the dirty reactor. This process resulted in the most drastic sample color change and is most likely due to the longer treatment time. In addition, during the second plasma exposure there was significantly decreased plasma coupling (i.e., the plasma "bright spot" was in the coil region rather than downstream) compared to the system during the first exposure. Based on our observations of what was occurring with the dirty

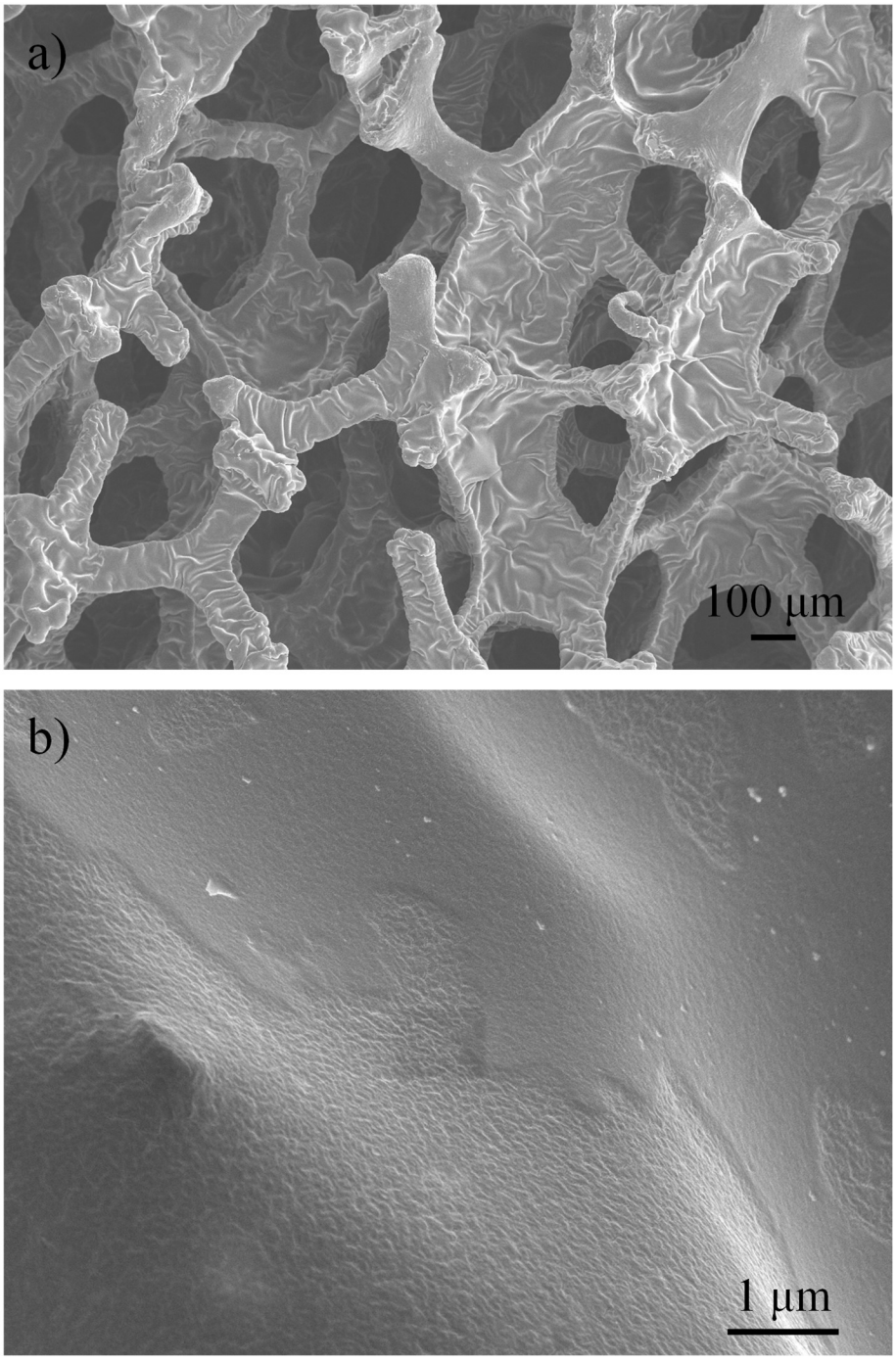

Figure 6.11. SEM images of butter P50 sample on Ni foam at (a) x60 and (b) x15000 magnification.

reactor, we hypothesize that during the first plasma exposure, the coconut oil on the samples is vaporized and deposited throughout the coil region of the reactor. This step also serves to remove the large excess of coconut oil from the Ni foam, potentially leaving only a thin layer that is easier for the plasma to convert to VGN. During the second plasma exposure (now with the "dirty" reactor walls), the coconut oil can be redeposited on the Ni foam. The thinner layer of the solid precursor and the vaporized gas-phase species from the reactor walls can increase VGN growth compared to the single plasma exposure process.

Reviewing the literature reveals that H_2 addition to the plasma feedgas could increase the likelihood of forming VGN. Seo *et al*. reported that a plasma feedgas ration of 80:20 of H_2:Ar grew the tallest and most uniform VGN their substrates.[17] The addition of H_2 in the plasma feedgas is often seen in traditional PE-CVD growth of VGN from precursors like methane or fluorocarbons as it removes impurities in the material through H-atom abstraction.[21, 23-24] Based on these reports, I chose to add some H_2 to the plasma feedgas (70:30 ratio of H_2:Ar, p = 60 mTorr). From Figure 6.12a, we can see that the UT coconut oil on the Ni foam results in a smooth coating that maintains the foam morphology of the substrate. At higher magnification, we observe an irregular morphology on the surface of the material. With the plasma treated samples (utilizing the double plasma exposure and addition of H_2 in the feedgas) the low magnification images (Fig. 6.12c and e) demonstrate that like the UT sample, the morphology of the foam is maintained and conformally coated. From the higher magnification images (Fig. 6.12d), although fully formed VGN are not apparent, these structures resemble literature examples depicting the very early stages of VGN growth.[21] These early-stage structures are also seen when TiO_2 NP were added to the coconut oil, indicating that the inclusion of the MO to the

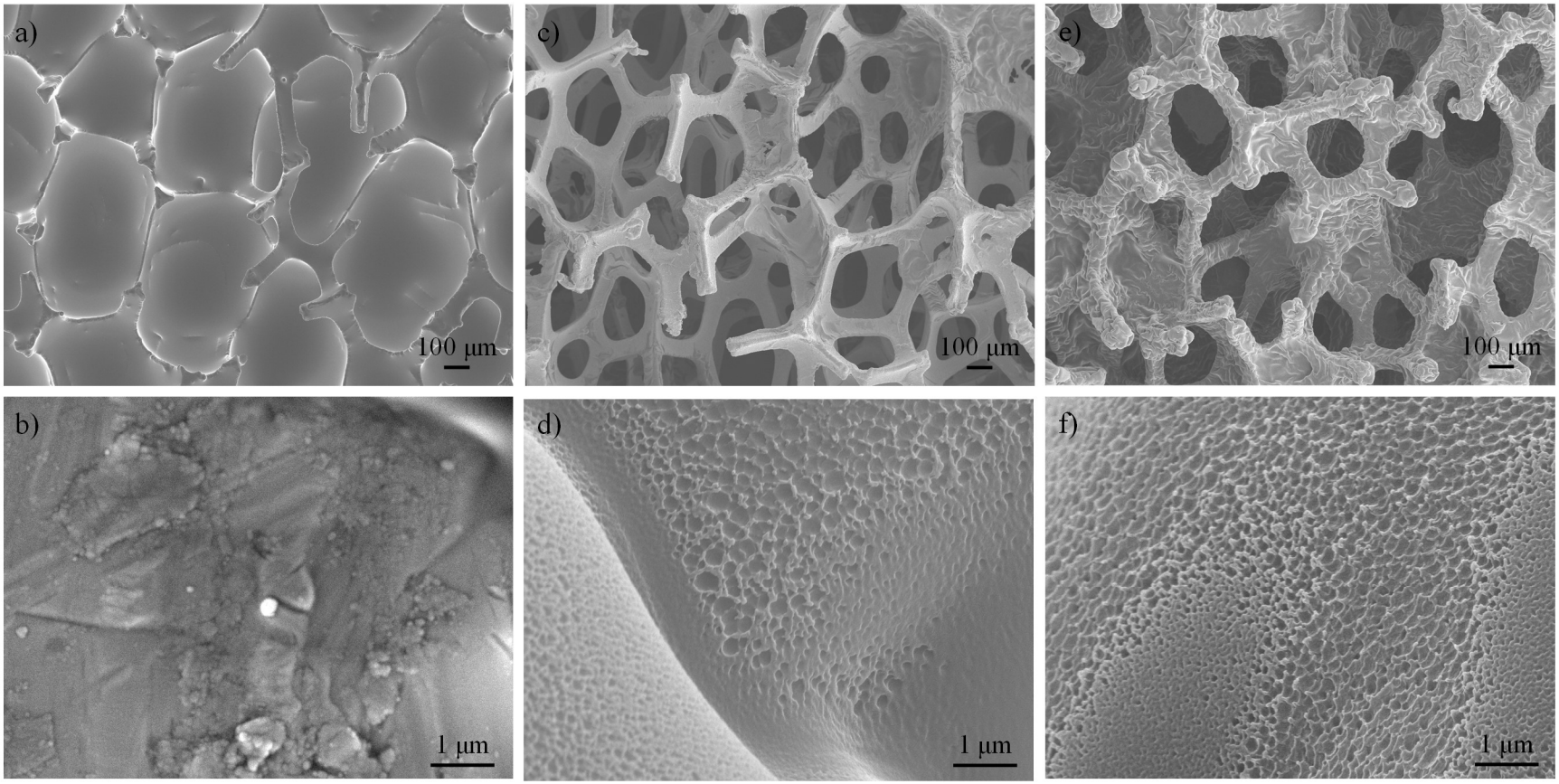

Figure 6.12. SEM images of (a – b) UT coconut oil and double plasma exposed (c – d) coconut P50 and (e – f) MO/coconut P50 samples. Images were taken at (a, c, e) x60 and (b, d, f) x15000 magnification.

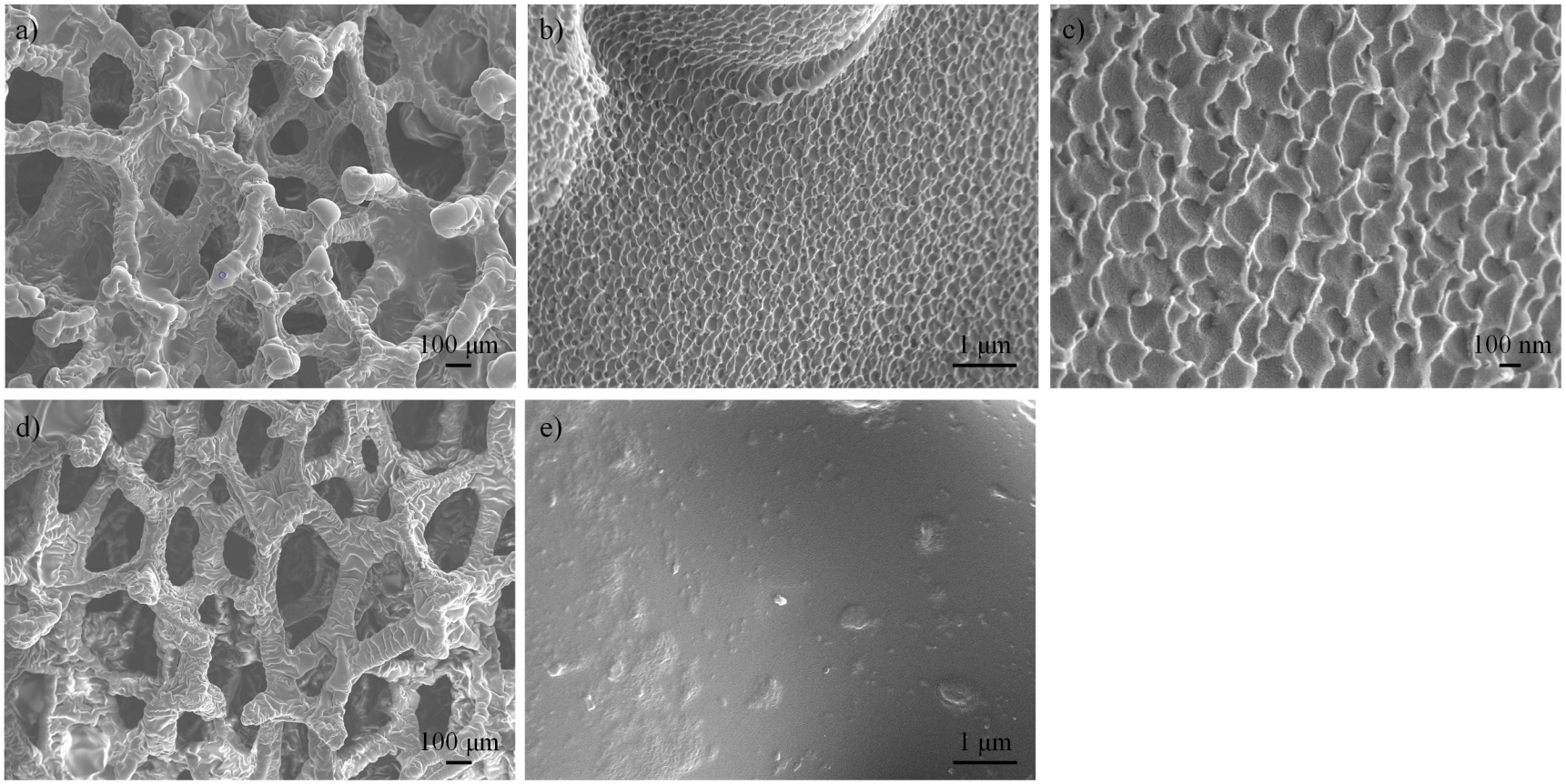

Figure 6.13. SEM images of butter double plasma exposed P50 samples placed on the (a- c) downstream and (d –e) upstream ends of the sample holder. Images were taken at (a, d) x60, (b, e) x1500, and (c) x50000 magnification.

solid precursor is not detrimental to the formation and growth of the VGN in this system. Compared to the relatively smooth surface of the single plasma exposure sample (Fig. 6.11b), these are promising results that the double exposure and addition of H_2 to the feedgas improve the formation of VGN and MO/VGN.

The observation that VGN are growing via PE-CVD rather than straight plasma conversion is also supported by the lack of growth when using the smaller sample holder. With the larger sample holder, the sample on the inlet side of the coil serves as a sacrificial precursor source similar to the film on the "dirty" reactor walls. The plasma can then vaporize the solid precursor, forming growth species in the gas phase that can then be deposited on the samples downstream, allowing for increased VGN growth on these substrates. Comparison of SEM images of downstream (Fig. 6.13 a – c) and upstream (Fig. 6.13d – e) samples support this theory. Structures that appear to be more distinct and uniformly shaped versions of the ones seen in Figure 6.12d and f can be seen on the downstream sample, whereas the upstream sample at the high magnification appears to be much smoother.

Along with allowing for a sacrificial precursor source, the larger sample holder may also be contributing to the actual growth process. Ma *et al.* added a Cu sleeve to their plasma reactor to achieve VGN growth with $P = 280$ W and heating their substrate to 500 °C.[22] They propose that increased growth with the Cu sleeve arises from the Cu surface catalyzing decomposition of the hydrocarbon precursor, thereby enhancing the formation of critical species in the VGN growth process. Another study also highlights the role of an upstream Cu catalyst on the deposition of graphene.[25] Instead of placing a Cu foil directly upstream of the sample, the authors placed their catalyst 3.5 – 7.0 cm upstream of the substrate to focus on the role of vaporized "free floating" Cu atoms catalyzing the decomposition of the precursor in the gas-

phase.[25] Although no gas-phase studies were done to confirm the presence of gaseous Cu; the authors state that this method relies on "the fact that Cu is a metal that readily sublimes" at the growth temperature used in this study (≥800 °C).[25] It should be noted that for samples grown for >3.5 hours, Cu islands were deposited on the substrate, suggesting that these particles participate in some form in graphene formation. Therefore, although the smaller sample holder allowed for better control of sample placement and lower reflected rf power, the larger sample holder served the dual purpose of having an additional precursor source and a potential catalyst in the growth process. In addition to optimizing VGN and MO/VGN growth, future work is needed using optical emission spectroscpocy to elucidate key species in the growth mechanism. Along with comparing species present with all of these troubleshooting steps, temporal studies can be done to calculate rates of formation and decomposition for these species within the system. Once this process is finalized, future work improving these materials for gas sensor or energy storage applications with post-synthetic plasma modification is outlined in Appendix A.

6.3 Summary

Here, the growth and characterization of several materials of interest for MO gas sensors were presented with varying degrees of success with either the synthetic process or the sensing performance. ZnO NP were successfully used to make a second type of MO PGS that demonstrated improved CO response at room temperature after plasma treatment. In addition, the comparison of the UT ZnO NP and μrod sensors highlights the need to examine the impact of both material morphology and purity when utilizing these materials in applications like gas sensors. The deposition of a SnO_2 TF on paper allows for the expansion of previous work done in our lab directly comparing various forms of SnO_2 and increases our understanding of the relationship between material structure and function. The current gas sensing experiments,

however, need to be adjusted so the resistance of these sensors can be measured and the response to target gases can be calculated.

Although a significant amount of work is still needed to reliably and reproducibly grow VGN from solid precursors, this work has made progress toward elucidating critical components in the formation of VGN. The importance of H_2 in the feed gas and a Cu catalyst were identified, and our results were supported by other published works. In addition, a more controlled and reproducible method was developed to imitate the conditions of the "dirty" reactor that was previously shown to grow VGN in our lab successfully.

REFERENCES

1. Kim, H.-J.; Lee, J.-H., Highly Sensitive and Selective Gas Sensors Using p-type Oxide Semiconductors: Overview. *Sens. Actuators B* **2014,** *192*, 607-627.
2. Fazio, E.; Spadaro, S.; Corsaro, C.; Neri, G.; Leonardi, S. G.; Neri, F.; Lavanya, N.; Sekar, C.; Donato, N.; Neri, G., Metal-Oxide Based Nanomaterials: Synthesis, Characterization and Their Applications in Electrical and Electrochemical Sensors. *Sensors* **2021,** *21* (7), 2494.
3. Stuckert, E. P.; Miller, C. J.; Fisher, E. R., The Effect of Ar/O_2 and H_2O Plasma Treatment of SnO_2 Nanoparticles and Nanowires on Carbon Monoxide and Benzene Detection. *ACS Appl. Mater. Interfaces* **2017,** *9* (18), 15733-15743.
4. Kan, D.; Niwa, Y.; Koganezawa, T.; Shimakawa, Y., Growth-Temperature-Dependent Coalescence Determines Structural Phase of Mist-Chemical-Vapor-Deposition-Grown SnO_2 Thin Films. *J. Appl. Phys.* **2018,** *124* (12), 125303.
5. Maleki, M.; Rozati, S. M., An Economic CVD Technique for Pure SnO_2 Thin Films Deposition: temperature effects. *Bull. Mater. Sci.* **2013,** *36* (2), 217-221.
6. Zhou, X.; Huang, B.; Zou, Y.; Xie, J.; Yang, J., Cotton-Templated Fabrication of Hierarchical SnO_2 Mesoporous Microtubes as the Anode Material of Lithium Ion Battery. *Mater. Lett.* **2014,** *120*, 279-282.
7. Vayssieres, L.; Keis, K.; Lindquist, S.-E.; Hagfeldt, A., Purpose-Built Anisotropic Metal Oxide Material: 3D Highly Oriented Microrod Array of ZnO. *The Journal of Physical Chemistry B* **2001,** *105* (17), 3350-3352.
8. Bai, H.; Guo, H.; Wang, J.; Dong, Y.; Liu, B.; Xie, Z.; Guo, F.; Chen, D.; Zhang, R.; Zheng, Y., A Room-Temperature NO_2 Gas Sensor Based on CuO Nanoflakes Modified with rGO Nanosheets. *Sens. Actuators B* **2021,** *337*, 129783.
9. Mehmood, S.; Zhao, X.; Fahad Bhopal, M.; Ullah Khan, F.; Yang, Y.; Wang, G.; Pan, X., MoO_2-Ni-Graphene Ternary Nanocomposite for a High-Performance Room-Temperature Ethanol Gas Sensor. *Appl. Surf. Sci.* **2021,** *554*, 149595.
10. Wang, C.; Wang, Y.; Yang, Z.; Hu, N., Review of Recent Progress on Graphene-Based Composite Gas Sensors. *Ceram. Int.* **2021,** *47* (12), 16367-16384.
11. Yuan, W.; Shi, G., Graphene-Based Gas Sensors. *J. Mater. Chem. A* **2013,** *1* (35), 10078-10091.
12. Mao, S.; Cui, S.; Lu, G.; Yu, K.; Wen, Z.; Chen, J., Tuning Gas-Sensing Properties of Reduced Graphene Oxide Using Tin Oxide Nanocrystals. *J. Mater. Chem.* **2012,** *22* (22), 11009-11013.
13. Ghosh, S.; Polaki, S. R.; Sahoo, G.; Jin, E.-M.; Kamruddin, M.; Cho, J. S.; Jeong, S. M., Designing Metal Oxide-Vertical Graphene Nanosheets Structures for 2.6V Aqueous Asymmetric Electrochemical Capacitor. *J Ind Eng Chem* **2019,** *72*, 107-116.
14. Poonam; Sharma, K.; Arora, A.; Tripathi, S. K., Review of Supercapacitors: Materials and Devices. *J. Energy Storage* **2019,** *21*, 801-825.
15. Sahoo, G.; Polaki, S. R.; Anees, P.; Ghosh, S.; Dhara, S.; Kamruddin, M., Insights Into the Electrochemical Capacitor Performance of Transition Metal-Vertical Graphene Nanosheet Hybrid Electrodes. *Phys. Chem. Chem. Phys.* **2019,** *21* (45), 25196-25205.
16. Stoica, S. D.; Vizireanu, S.; Acsente, T.; Dinescu, G., Hybrid Nanomaterial Architectures: Combining Layers of Carbon Canowalls, Nanotubes, and Particles. *Plasma Chem. Plasma Process.* **2018,** *38* (4), 695-706.

17. Seo, D. H.; Han, Z. J.; Kumar, S.; Ostrikov, K., Structure-Controlled, Vertical Graphene-Based, Binder-Free Electrodes from Plasma-Reformed Butter Enhance Supercapacitor Performance. *Adv. Energy Mater.* **2013,** *3* (10), 1316-1323.
18. Kumar, S.; Martin, P.; Bendavid, A.; Bell, J.; Ostrikov, K. K., Oriented Graphenes from Plasma-Reformed Coconut Oil for Supercapacitor Electrodes. *Nanomaterials* **2019,** *9* (12), 1679.
19. Hanna, A. R.; Fisher, E. R., Tailoring the Surface Properties of Porous Zeolite Constructs Using Plasma Processing. *Microporous Mesoporous Mater.* **2020,** *307*, 110467.
20. Stuckert, E. P.; Miller, C. J.; Fisher, E. R., Gas-Phase Diagnostics During H_2 and H_2O Plasma Treatment of SnO_2 Nanomaterials: Implications for Surface Modification. *Journal of Vacuum Science & Technology B* **2017,** *35* (2), 021802.
21. Shiji, K.; Hiramatsu, M.; Enomoto, A.; Nakamura, M.; Amano, H.; Hori, M., Vertical Growth of Carbon Nanowalls Using rf Plasma-Enhanced Chemical Vapor Deposition. *Diamond Relat. Mater.* **2005,** *14* (3), 831-834.
22. Ma, Y.; Jang, H.; Kim, S. J.; Pang, C.; Chae, H., Copper-Assisted Direct Growth of Vertical Graphene Nanosheets on Glass Substrates by Low-Temperature Plasma-Enhanced Chemical Vapour Deposition Process. *Nanoscale Research Letters* **2015,** *10* (1), 308.
23. Ghosh, S.; Polaki, S. R.; Kumar, N.; Amirthapandian, S.; Kamruddin, M.; Ostrikov, K. K., Process-Specific Mechanisms of Vertically Oriented Graphene Growth in Plasmas. *Beilstein J. Nanotechnol.* **2017,** *8*, 1658-1670.
24. Santhosh, N. M.; Filipič, G.; Tatarova, E.; Baranov, O.; Kondo, H.; Sekine, M.; Hori, M.; Ostrikov, K. K.; Cvelbar, U., Oriented Carbon Nanostructures by Plasma Processing: Recent Advances and Future Challenges. *Micromachines* **2018,** *9* (11), 565.
25. Teng, P.-Y.; Lu, C.-C.; Akiyama-Hasegawa, K.; Lin, Y.-C.; Yeh, C.-H.; Suenaga, K.; Chiu, P.-W., Remote Catalyzation for Direct Formation of Graphene Layers on Oxides. *Nano Lett.* **2012,** *12* (3), 1379-1384.

CHAPTER 7

RESEARCH SUMMARY AND FUTURE DIRECTIONS

This section summarizes the main findings and overarching themes presented in Chapters 3 – 6. Possible directions for continuing the work discussed in this dissertation are proposed.

7.1 Research Summary

Areas like health care, energy storage, gas detection, and catalysis utilize nanomaterials due to their unique surface properties, relatively low production cost, and varied morphology and composition.[1-3] As these materials often rely on surface properties to control their performance in a given application, LTP processing is an attractive modification approach as it can alter the surface of a material while maintaining bulk properties. In addition, the large parameter space allows for tuneable treatments, lending this technique to a variety of uses.[4-5] Although this work presents the studies in the context of improving gas sensor and PPE materials, the potential of plasma processing for other applications is clear. Here, several systems were employed to etch (CO_2, O_2/Ar, and $H_2O_{(v)}$), deposit a film (CO and C_3F_8), and functionalize ($H_2O_{(v)}$ and CO_2 at high *P*) the surface of a material. Also, the process of relating changes in the plasma to changes in the material and the resulting performance can be used to study many convoluted systems. By using complementary techniques, understanding of fundamental processes can be elucidated.

This dissertation explores the applicability of LTP modification of SMO nanomaterials and textiles for use as gas sensor materials and protective clothing, respectively. In Chapter 3,

previous work in the Fisher Group was expanded by examining the effect of CO and CO_2 plasma treatments on SnO_2 NP gas sensors. Using OES, excited-state gas species were monitored and revealed that overall, the two plasmas had very similar spectra. The main difference was that the CO_2 plasma had additional signals from CO_2^+ and O (a product of decomposition of the precursor gas). Relative species densities were calculated for CO and O as these have been shown to be important species in the deposition and etching processes, respectively. Combining these spectroscopy data with XPS analysis of the SnO_2 NP showed that the CO plasma deposited an amorphous carbon film, whereas the CO_2 plasma etched the lattice of the SnO_2. Gas sensing studies demonstrate that the film formation on the CO plasma modified samples blocked analyte-SnO_2 interactions and had a detrimental effect on device performance. After CO_2 plasma treatment, sensors had significantly larger responses to benzene and CO when compared to the UT sensor. In addition, the CO_2 plasma treated sensors also exhibited some response and recovery behavior.

In an effort to improve the cost and flexibility of these traditional sensors (SMO on a ZrO_2 wafer substrate), the fabrication and plasma modification processes were adapted to be compatible with a PGS (Chapter 4). SnO_2 NP were dropcast onto paper substrates with screen-printed carbon paste electrodes. Here, O_2/Ar plasma treatments (P = 15 – 60 W) improved these devices by increasing the response to ethanol and CO, lowering the T_S to ≤50 °C, and showing some response and recovery behavior. These gas sensing results were coupled with OES and material studies to understand how the plasma modified the SMO and why these changes resulted in improved device performance. The use of a paper substrate has the additional benefit of increasing the amount of surface area available to interact with gases during sensing. Therefore, preliminary work using ZnO NP and SMO grown directly on the substrate were also

explored in Chapter 6 as alternative gas sensor materials. This section also includes work toward growing VGN from solid hydrocarbon precursors. This section also contains a brief literature study in attempt to identify vital components to VGN formation in our system.

Chapter 5 explores the attachment and resuspension behavior of Al_2O_3 NP, carbon black, and CNT with four types of lab coats. Fabrics were treated with a C_3F_8 or $H_2O_{(v)}$ plasma to make the surfaces more hydrophobic or hydrophilic when compared to the UT material. Coupled XPS and WCA studies confirm the C_3F_8 samples had a thin FC film deposited on them and a corresponding decrease in wettability and the $H_2O_{(v)}$ samples had increased O-functionality and a corresponding increase in wettability. The WCA of the hydrophilic fabrics were measured after 2 days and 1 month to monitor the effect of aging on this treatment. Although the cotton and Tyvek® samples showed little change at these time points, the PP and blend materials experienced hydrophobic recovery and had measurements within error of the UT fabrics. Contamination and release studies of the UT and plasma treated materials demonstrated that larger nanomaterial agglomerates <600 μm have the highest probability of being resuspended, agreeing with trends reported by other studies.[6-7] In general, the $H_2O_{(v)}$ materials had the lowest carbon black contamination and the FC cotton had the lowest contamination and release amounts overall. These results indicate that the surface chemistry of the material does play some role in the attachment and resuspension of nanomaterials.

Both of these projects emphasize the need for understanding the relationship between surface properties and application-based performance. By relating changes in the plasma, material, and performance, an understanding of how these materials work in a given application can be determined. This knowledge is important as it can aid in efficiently selecting material and plasma system combinations to optimize the material's surface properties for a specific goal.

7.2 Future Directions

As discussed in previous sections, some work is needed to complete characterizing the materials presented in Chapters 3 – 6. Although the adaptation of the sensing chamber to monitor real-time detection during gas sensing allowed for another metric to evaluate device performance, some challenges are still present. In particular, the sensing chamber relies on passive gas flow due to the pressure difference between the gas tank and the atmosphere. This not only sets the mass flow controller's lowest flow rate at 25 sccm (see Chapter 6) but also causes the need for a flushing step during response and recovery studies (discussed in Chapter 4). A much lower flow rate can be used by adding a mechanical pump to the sensing chamber, potentially allowing for gas sensing experiments with the SnO_2 TF PGS.

Expansion of sensor performance studies to include determination of the sensor's limit of detection, concentration studies, and inclusion of reducing gases like CO_2 and N_2 are all needed to assess the applicability of these sensors for use outside of laboratory conditions. Finally, mixed gas sensing and humidity studies are necessary to evaluate the cross sensitivity of these devices. Similar to the work presented in this dissertation, cross sensitivity is often inferred by comparing sensor response values determined by exposing the sensor to each gas individually.[8-10] This approach does not realistically reproduce the complexities of competing gas-SMO interactions that occur when a sensor is in the presence of multiple gases. Mixed gas sensing will also be useful for testing sensor arrays for multigas detection. As discussed in Chapters 3 and 4, different plasma treatments resulted in the gas with the highest response to change. Therefore, by constructing an array of sensors with different gas sensitivities, multiple gases can be detected simultaneously.

From Chapter 6, more work is needed to optimize the growth of VGN and MO/VGN. One possible route to this is the addition of another precursor source by including a hydrocarbon or fluorocarbon to the plasma feedgas.[11-14] Furthermore, OES studies can aid in determining critical species involved with the growth mechanism. The continuation of this project using post-synthetic plasma modification is described in detail in Appendix A.

Continuing the experiments in Chapter 5, alternative plasma treatments are needed to improve the wettability of PP. Previous work in our lab modified polycarbonate membranes with O_2, CO_2, $H_2O_{(g)}$, and formic $acid_{(g)}$.[15] Although all of the treatments resulted in similar increases in O% and the addition of the same functional groups, only the CO_2 plasma treated membranes had no measurable change in hydrophobicity even after aging in ambient conditions for 28 days. Thus, this is a possible alternative system to improve the hydrophilicity of this fabric. Due to the PP being the thinnest material studied, extra care is needed to balance treatment efficacy and minimize sample damage. A common strategy to modify delicate materials is to use a pulsed plasma. A pulsed system allows for higher instantaneous powers, lower substrate temperatures, and potentially improved treatment uniformity.[16]

Expanded studies analyzing the same spot SEM images are also needed for the remaining fabrics and ENP not shown in Figures 5.11 and 5.12. Although these experiments have a much smaller sample size than the agglomerate counts, these images are the most direct method to evaluate the behavior of these materials with the fabrics. In addition to ENP resuspension, another concern is the ability of particles to penetrate through PPE.[17-18] Golanski *et al*. found that in general, the penetration ability increases as the diameter of the graphite nanoaerosol increases.[18] The authors also note that the woven cotton had a penetration value of up to 27%, whereas the synthetic polyethylene had a maximum penetration value of ~2%. Thus, exploring

the impact of these treatments on the penetration of ENP through the fabric is another method to evaluate the success of improving PPE materials through LTP modification. Finally, textile tests such as flammability and abrasion resistance for the reusable lab coat materials are needed to ensure that plasma treatments do not have an adverse effect on other physical properties of the fabric.

REFERENCES

1. Jose Varghese, R.; Sakho, E. h. M.; Parani, S.; Thomas, S.; Oluwafemi, O. S.; Wu, J., Chapter 3 - Introduction to Nanomaterials: Synthesis and Applications. In *Nanomaterials for Solar Cell Applications*, Thomas, S.; Sakho, E. H. M.; Kalarikkal, N.; Oluwafemi, S. O.; Wu, J., Eds. Elsevier: 2019; pp 75-95.
2. Rivero, P. J.; Urrutia, A.; Goicoechea, J.; Arregui, F. J., Nanomaterials for Functional Textiles and Fibers. *Nanoscale Res. Lett.* **2015,** *10* (1), 501-501.
3. Singh, A. K., Chapter 1 - Introduction to Nanoparticles and Nanotoxicology. In *Engineered Nanoparticles*, Singh, A. K., Ed. Academic Press: Boston, 2016; pp 1-18.
4. Grill, A., *Cold Plasma in Materials Fabrication: From Fundamentals to Applications*. IEEE: New York, 1994.
5. Bogaerts, A.; Tu, X.; Whitehead, J. C.; Centi, G.; Lefferts, L.; Guaitella, O.; Azzolina-Jury, F.; Kim, H.-H.; Murphy, A. B.; Schneider, W. F.; Nozaki, T.; Hicks, J. C.; Rousseau, A.; Thevenet, F.; Khacef, A.; Carreon, M., The 2020 Plasma Catalysis Roadmap. *J. Phys. D: Appl. Phys.* **2020,** *53* (44), 443001.
6. McDonagh, A.; Byrne, M. A., A Study of The Size Distribution of Aerosol Particles Resuspended from Clothing Surfaces. *J. Aerosol Sci* **2014,** *75*, 94-103.
7. McDonagh, A.; Byrne, M. A., The Influence of Human Physical Activity and Contaminated Clothing Type on Particle Resuspension. *J. Environ. Radioact.* **2014,** *127*, 119-126.
8. Barsan, N.; Koziej, D.; Weimar, U., Metal Oxide-Based Gas sensor Research: How To? *Sens. Actuators B* **2007,** *121* (1), 18-35.
9. Liu, X.; Cheng, S. T.; Liu, H.; Hu, S.; Zhang, D. Q.; Ning, H. S., A Survey on Gas Sensing Technology. *Sensors* **2012,** *12* (7), 9635-9665.
10. Subbiah, D. K.; Babu, K. J.; Das, A.; Rayappan, J. B. B., NiOx Nanoflower Modified Cotton Fabric for UV Filter and Gas Sensing Applications. *ACS Appl. Mater. Interfaces* **2019,** *11* (22), 20045-20055.
11. Dou, S.; Tao, L.; Wang, R.; El Hankari, S.; Chen, R.; Wang, S., Plasma-Assisted Synthesis and Surface Modification of Electrode Materials for Renewable Energy. *Adv. Mater.* **2018,** *30* (21), 1705850.
12. Santhosh, N. M.; Filipič, G.; Tatarova, E.; Baranov, O.; Kondo, H.; Sekine, M.; Hori, M.; Ostrikov, K. K.; Cvelbar, U., Oriented Carbon Nanostructures by Plasma Processing: Recent Advances and Future Challenges. *Micromachines* **2018,** *9* (11), 565.
13. Shiji, K.; Hiramatsu, M.; Enomoto, A.; Nakamura, M.; Amano, H.; Hori, M., Vertical Growth of Carbon Nanowalls Using rf Plasma-Enhanced Chemical Vapor Deposition. *Diamond Relat. Mater.* **2005,** *14* (3), 831-834.
14. Wu, Y.; Qiao, P.; Chong, T.; Shen, Z., Carbon Nanowalls Grown by Microwave Plasma Enhanced Chemical Vapor Deposition. *Adv. Mater.* **2002,** *14* (1), 64-67.
15. Tompkins, B. D.; Dennison, J. M.; Fisher, E. R., Etching and Post-Treatment Surface Stability of Track-Etched Polycarbonate Membranes by Plasma Processing Using Various Related Oxidizing Plasma Systems. *Plasma Process. Polym.* **2014,** *11* (9), 850-863.
16. Pulsipher, D. J. V.; Fisher, E. R., NH_2 and NH Surface Production in Pulsed NH_3 Plasmas on TiO_2: A Steady-State Probe of Short Pulse Plasmas. *Plasma Process. Polym.* **2013,** *10* (1), 6-18.

17. Gao, P.; Jaques, P. A.; Hsiao, T.-C.; Shepherd, A.; Eimer, B. C.; Yang, M.; Miller, A.; Gupta, B.; Shaffer, R., Evaluation of Nano- and Submicron Particle Penetration through Ten Nonwoven Fabrics Using a Wind-Driven Approach. *J. Occup. Environ. Hyg.* **2011,** *8* (1), 13-22.
18. Golanski, L.; Guiot, A.; Rouillon, F.; Pocachard, J.; Tardif, F., Experimental Evaluation of Personal Protection Devices Against Graphite Nanoaerosols: Fibrous Filter Media, Masks, Protective Clothing, and Gloves. *Hum. Exp. Toxicol.* **2009,** *28* (6-7), 353-359.

APPENDIX A

INDEPENDENT RESEARCH PROPOSAL

This appendix is the independent research proposal entitled *Plasma Synthesized and Modified Composite Vertical Graphene Nanosheets: Fabricating and Understanding Materials for Improved Energy Storage Devices*, written by Kimberly A. M. Hiyoto in fulfillment of the doctoral requirements of Colorado State University's Department of Chemistry. It discusses the potential fabrication and plasma modification of composite semiconducting metal oxides/vertical graphene nanosheets (VGN) to design better energy storage materials and further understanding of the VGN growth process and performance as a supercapacitor. I would like to thank Zoe Mann for providing some of the preliminary data and Dr. Carmen Menoni for helpful feedback during the writing process.

A.1 Overview, Research Summary

With the shift toward renewable energy sources, improved energy storage materials are also needed. Vertical graphene nanosheets (VGN) are a promising material as a result of their electrochemical stability, conductivity, large surface area, and high porosity. This proposal seeks to expand and combine existing materials synthesis and modification strategies with the goal of improving VGN energy storage capabilities. These strategies include adding nanostructured metal oxides (MO) and applying plasma surface modification, to not only make enhanced materials but to also better understand the relationship between material properties and device performance. The goals of the proposed work are to: (1) synthesize VGN and the composite

(MO/VGN) structures; (2) plasma modify these materials; and (3) measure the electrochemical behavior of the as-grown and plasma modified materials. Utilizing plasma diagnostics (during the growth and post-synthetic modification of the VGN and MO/VGN), materials characterization, and device performance studies, insight into optimized properties of these materials for energy storage applications can be determined and used to develop a targeted approach to making these devices.

A.2 Background and Motivation

For the past several years, the United States has steadily increased its energy consumption with ~80% coming from fossil fuels (petroleum, natural gas, and coal).[1] Note, however, that renewable energy consumption has also increased 3% when compared to 2017, with projections to further increase for the foreseeable future.[1] With this, there has also been a congruent need for materials that can be used in energy storage devices. Since first reported in 2002,[2] vertical graphene nanosheets (VGN), also called vertical carbon nanowalls, have gained much attention because of their superior electrochemical and material properties resulting from their abundant edge planes, large surface area, electrical conductivity, and electrochemical stability.[3-4]

Recent work has explored several strategies to enhance the performance of VGN, including the use of composite/hybrid materials or utilizing plasma modification. Composite materials combine either multiple types of carbon-based morphologies[5] or VGN with pseudocapacitive materials [in particular, metals[6-7] or metal oxides (MO)[3, 8]]. These additive materials are thought to improve the performance of VGN because pseudocapacitors are known to have a much larger theoretical capacitance than carbon-based materials. Therefore, by combining them, these hybrid materials have a larger theoretical capacitance while maintaining

desirable properties of bare VGN. Metal oxides (like MnO_2, Fe_2O_3, or TiO_2 nanostructures) are a popular choice because they are inexpensive and can be electroplated or thermally deposited onto already formed VGN. In addition to these composite materials (MO/VGN), post-synthetic plasma modification is another, less explored strategy to improve VGN for energy storage. Sahoo *et al*. describes increased charge storage performance of their VGN after microwave O_2 plasma treatment at 100, 300, and 600 W for 2 min.[9] They attribute the increase in capacitance to the surface oxygen functionalization and etching resulting from the plasma treatment. Both these effects result in transforming the VGN into a wettable material that can better interact with an aqueous electrolyte, demonstrated by the water contact angle (WCA) decreasing from 134° to <10°.

VGN are commonly synthesized by plasma-enhanced chemical vapor deposition (PE-CVD) due to its ability to reliably grow these structures on a variety of substrates and sometimes without a catalyst.[2, 10-11] This technique, however, utilizes high temperatures from large applied plasma powers (*P*) and/or additional substrate heating (≥550 °C). Also, most syntheses utilize high purity gaseous plasma precursors, requiring a secondary step to add MO to fabricate composite structures.[7, 10, 12] Thus, if one were to also plasma modify the MO/VGN, it would take three separate steps, complicating the process and increasing the price to make these materials. To move away from these gaseous hydrocarbon precursors, a limited amount of work has examined growing VGN with essential oil vapor added to a H_2 radio frequency (rf) plasma[13] and using food materials (like butter[8] and coconut oil[14]) applied directly onto a substrate, then transformed to VGN with plasma exposure. These processes using food materials allow for the added benefit of potentially mixing in the MO in the initial step, thus eliminating the need to decorate the VGN in an additional step. Although this process would result in MO throughout

the VGN (and not just attached on the surface), some would be exposed on the surface during the plasma conversion process allowing for a one-step synthesis of these MO/VGN.

In addition to simplifying the process of making these materials, this proposal seeks to improve understanding of the relationship between material surface chemistry and device performance. Although many studies utilize multiple material analysis techniques [e.g. Raman spectroscopy, X-ray photoelectron spectroscopy (XPS), scanning electron microscopy (SEM)] in conjunction with electrochemical studies, not much work has been done to examine the effects of surface functionalization. One example is a study done by Sahoo *et al.* that used an O_2 plasma to modify their materials and observed the impact of plasma treating directly after synthesis versus after a few days (with exposure to ambient conditions). Using XPS, they determined that the immediate modification resulted in hydroxy and carbonyl functionalization that led to increased hydrophilicity and enhanced VGN capacitance. It should be noted that they also observed a ~0.8 μm reduction in VGN height, decreased layers per sheet, and an increase of inter-sheet distance at all plasma treatment parameters explored. Thus, although the surface functionalization is probably the primary source of the increased hydrophilicity, the effect of material etching cannot be dismissed. This study, however, serves as a proof-of-concept that plasma modification can be used to improve VGN performance, but further work is needed to expand and optimize these material properties for applications in energy storage.

By utilizing other functionalizing plasma precursors (like CO_2, H_2O, and NH_3), the effect of different surface chemistries on capacitance can be assessed. In addition, O_2 plasmas are well-known etching and highly oxidizing systems, so by employing these other precursors that are less damaging to the material, the impacts of material etching and functionalization can be deconvoluted. The longevity of these treatments is also important to consider when determining

the applicability of this method to improving VGN for energy storage applications. For example, a subsequent study by Sahoo *et al.* found that the plasma treated VGN regained most of its hydrophobicity within 20 days for almost all parameters studied.[15] This further emphasizes the need to consider other plasma precursors to improve these materials. Finally, investigating and characterizing the plasma during VGN growth and the post-synthetic modification is needed to better understand how the material is interacting with the plasma in addition to how the plasma modifies the material.

A.3 Project Description

A.3.1 Intellectual Merit

The intellectual merit of this proposal lies primarily in three areas. First, although the growth process of VGN have been heavily studied and modeled, this has largely focused on PE-CVD systems utilizing methane and hydrogen as the precursor gases.[4, 11-12] Systems utilizing plasma transformation, larger hydrocarbons or complex precursors are not as well studied and their complexity makes them harder to understand. Thus, few fundamental studies exist that seek to elucidate how these precursors impact VGN growth pathways in the plasma.

Second, analysis of the plasma during post-synthetic modification is also needed as not many studies have utilized techniques to characterize the plasma during this step. Knowing how the plasma is interacting with the material and how the material impacts the plasma is vital to understanding the modification process. Often in plasma systems, multiple processes (etching, deposition, and functionalization) can occur simultaneously and may be in competition with each other. Thus, by identifying key species in the desired process, plasma treatment parameters can be selected and optimized for a desired application. With optical spectroscopy, not only can gas-phase species in the plasma be identified, but plasma characteristics like relative species

densities, formation/decomposition rate constants, and internal molecular temperatures (vibrational and rotational) can be calculated for these systems. Looking at trends in plasma energetics and kinetics will illuminate information like potential reaction pathways.

Third, along with expanding knowledge on growth and modification of MO/VGN, this study will provide an alternative one-step route to synthesizing these composite materials. This simpler fabrication will allow for other post-synthesis modifications while still being feasible to scale up industrially.

A.3.2 Specific Aims

- The overarching purpose of the proposed work is to not only fabricate MO/VGN with improved electrochemical properties, but to also gain a better understanding of the growth and modification processes and the relationship between material properties and performance. This project will work toward the following goals (represented in Fig. A.1): optimize plasma conversion of coconut oil to VGN on a Ni foam substrate;
- develop a one-step synthesis to synthesize MO/VGN and then optimize post-synthetic plasma treatment conditions to further improve capacitance device performance; tactics for this goal include
    - monitoring gas-phase species in the plasma during both MO/VGN growth and plasma modification
    - characterizing the as-grown and plasma-modified materials
- expand understanding of the relationship between material characteristics (bulk and surface) and device performance.

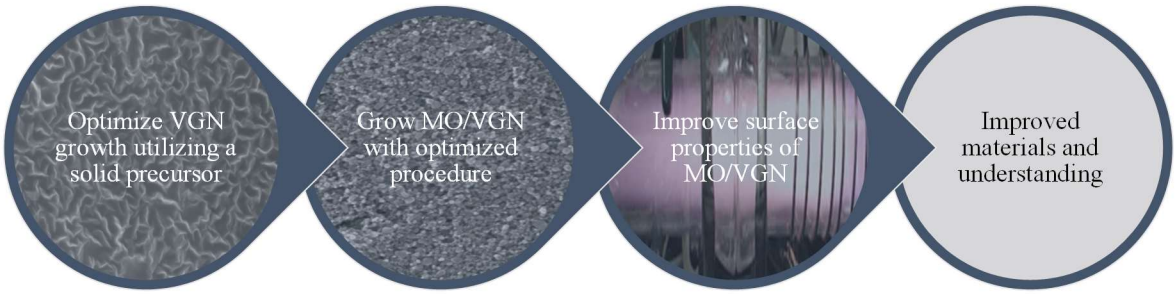

Figure A.1. Conceptual framework of goals of this proposal.

A.4 Proposed Work

This proposal will utilize several techniques to characterize the material, study the resulting electrochemical properties, and examine the growth and modification process to assess the efficacy of this fabrication strategy. Together, these results will further fundamental knowledge of these materials. The process (summarized in Fig. A.2) is broken into three major milestones: (1) synthesis and characterization of VGN and MO/VGN, (2) plasma modification of VGN and MO/VGN and characterization, and (3) performance testing of the as-grown and plasma modified materials.

A.4.1 Synthesis and characterization of VGN and MO/VGN.

VGN will be synthesized in a process adapted from literature.[8, 14] Ni foam (2 cm x 1 cm) is dipped into melted coconut oil and positioned vertically to allow excess oil to drip off and leave the remaining oil to harden. For composite materials, the melted coconut oil will have commercial TiO_2 nanoparticles (NP) added and well dispersed before the dipping step. Utilizing a home-built rf inductively coupled plasma (ICP) reactor, described previously,[16-17] dipped substrates will be placed vertically, parallel to gas flow, in the bright spot of the plasma. Preliminary work[18] indicates that a pulsed Ar (99.999%, Airgas) plasma [50% duty cycle, 300 W peak power, 50 mTorr] results in VGN growth on a Cu tape substrate with the coconut oil, Fig. A.3. Thus, these will be the initial operating conditions when working with the Ni foam. The Ni foam was chosen over the Cu tape because of its larger surface area and electrochemical inertness in the potential range selected for cyclic voltammetry experiments.

During VGN and MO/VGN growth, reactors with quartz windows will be used to collect optical emission spectroscopy (OES) data and quantify excited state gas-phase species present

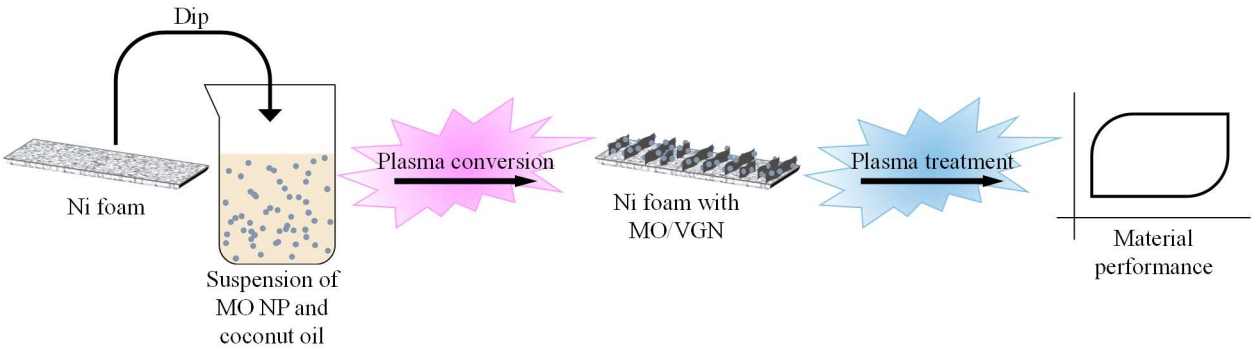

Figure A.2. Schematic of proposed MO/VGN synthetic procedure. Note the process is the same for VGN synthesis, only no MO are included in the coconut oil. The NP and MO/VGN are not to scale but are enlarged for clarity.

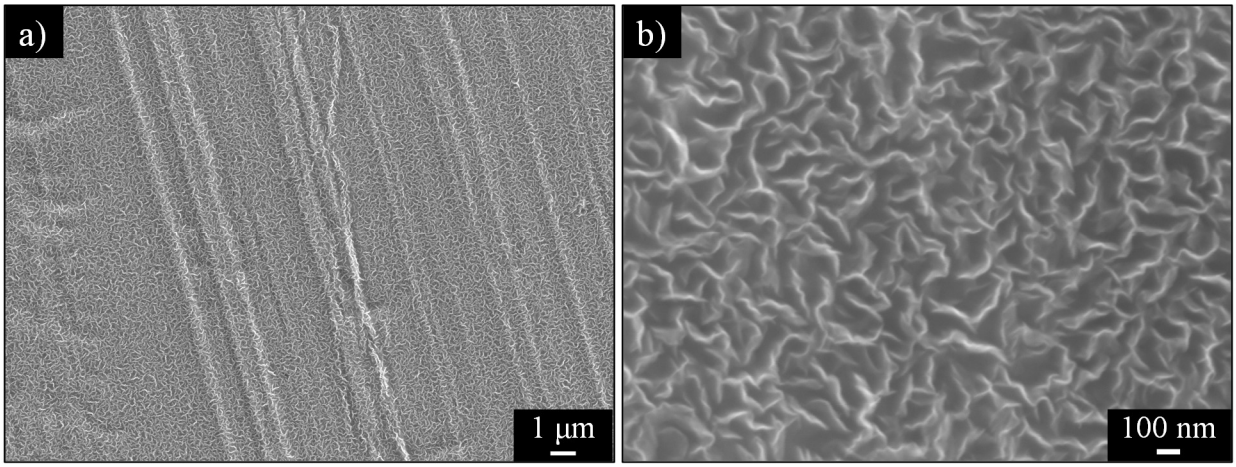

Figure A.3. SEM image of VGN grown on Cu tape from coconut oil at (a) x5000 and (b) x45000.

with and without the substrate. Studies looking at the growth of VGN in PE-CVD systems typically report H and CH_x species playing a significant role in the synthesis and quality of the VGN.[4, 19] Thus, the presence and relative densities of these species will be determined to see if they also play similar role in this system. When possible, the rotational and vibrational temperatures will also be calculated to better understand the energy partitioning during VGN and MO/VGN growth. Additionally, time-resolved OES will be used to illuminate information on species kinetics, providing further insight into key mechanistic processes. These insights gained through understanding the energetics and kinetics during VGN and MO/VGN formation will yield critical knowledge about the effects of a complex solid precursor and addition of MO on the growth mechanism of these structures.

To assess the VGN and MO/VGN materials, several characterization techniques will be employed to analyze surface and bulk properties. Raman spectroscopy and SEM will be used to determine bulk structural properties and material morphology; XPS and WCA analyses will provide information on the surface properties. Preliminary characterization of the Ni foam substrate and coconut oil (Fig. A.4) indicate that both are hydrophobic with WCA of ≥94.6°. Note that the WCA of the coconut oil dipped sample is slightly smaller than that of the bare Ni foam resulting from the slightly more hydrophilic surface due to the carboxylic acid tails of the fatty acids that make up the oil. With the conversion of the coconut oil to VGN or MO/VGN, we expect these as-grown materials will also be hydrophilic.[9]

As the goal of milestone 1 is to fabricate these materials in a one-step process, successful VGN and MO/VGN growth will be indicated by dense coverage of the Ni foam substrate (most of the coconut oil is converted to VGN). For the MO/VGN, some exposure of the MO nanoparticles can be seen on the surface of the VGN and should be dispersed in a fairly

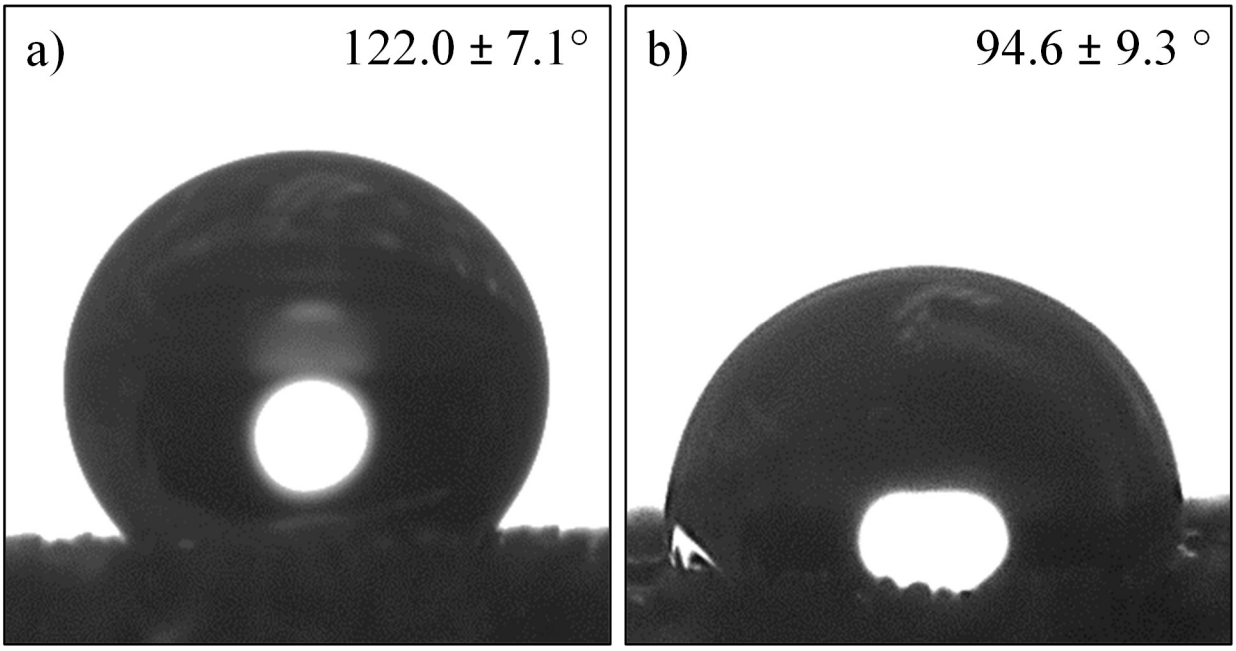

Figure A.4. Representative photograph of a 2 µL drop of water interacting with (a) Ni foam and (b) Ni foam dipped in coconut oil. Insets represent the average WCA and corresponding standard deviation (n≥9).

consistent manner on the VGN over the entire substrate. Materials characterization of the as-grown VGN and MO/VGN obtained in this step will serve as a comparison to the plasma-modified samples described in the next milestone. Finally, OES measured with and without the substrate in the plasma will focus on identifying and quantifying excited state gas-phase species critical to the growth of VGN and composite materials and understanding potential growth mechanisms.

A.4.2 Plasma modification of VGN and MO/VGN and characterization.

Following the fabrication of the VGN and MO/VGN, rf plasma modification will also be used to post-synthetically treat these materials. In the Sahoo *et.al.* study, VGN were modified using a O_2 microwave plasma at P = 100, 300, and 600 W, with pressure (p) = 1.2 x10^{-3} mbar (~ 1 mTorr).[9] These conditions were chosen to allow for "an effective change in VGN surfaces to super-hydrophilic behavior without reduction in height",[9] thus, with the differences in our systems (rf ICP, typically P = 10 – 150 W and p = 15 – 200 mTorr) these treatment parameters will need to be optimized for a similar effect in our system. In addition to O_2 plasma treatments, other plasma precursors (CO_2, H_2O, and NH_3) will also be used to treat the VGN and MO/VGN. These plasma precursors were chosen as they are likely to impart either oxygen or nitrogen functionality, leading to more hydrophilic surfaces. Moreover, as previously mentioned, these plasma systems do not etch/damage the materials as much as O_2 plasmas. As discussed in milestone 1, OES will also be used during post-synthetic plasma treatment to better understand the modification process. This will be combined with material analysis techniques (SEM, Raman spectroscopy, XPS, and WCA analysis) to determine chemical and morphological changes in the materials after plasma exposure. Finally, an aging study measuring the WCA of the treated VGN and MO/VGN will be done to assess the longevity of these plasma treatments as

another measure of the success of a specific plasma treatment. WCA provides a simple measure of changes in surface chemistry over time that could lead to hydrophobic recovery.

Similar to the Sahoo *et al*. paper, the time between fabrication and modification will also be explored. With the O_2 plasma treatment, the authors found that modifying the VGN immediately after fabrication resulted in better electrochemical properties, as opposed to waiting a couple of days between fabrication and treatment. Therefore, some work comparing immediate and delayed (48 hours after growth with exposure to ambient conditions) modification will also be explored with these plasma modified materials to further expand the range of surface chemistries and resulting behaviors that can be created by plasma surface modification.

Successful plasma modification (with the various precursors and the immediate/delayed treatment protocol) in milestone 2 will be marked by the resulting materials still maintaining the VGN and MO/VGN morphology and good adhesion to the underlying Ni substrate. In addition, successful plasma treatments will result in materials that remain hydrophilic during the aging study (indicating stability of the modification). Also, material analysis post modification will be measured such that it is comparable to the as-grown samples described in the first milestone. These studies will be used to quantify how the materials changed after plasma treatment and ultimately be related to the capacitive performance (described in milestone 3). Key plasma species and detailed physical and chemical properties of the modification process will be studied with OES by collecting data within these plasma-modification systems with and without a VGN or VGN/MO substrate.

A.4.3 Performance testing of the as-grown and plasma modified materials.

Finally, the electrochemical performance of all the as-grown and post-synthetically modified materials will be assessed. From the cyclic voltammogram (CV), metrics like ideal

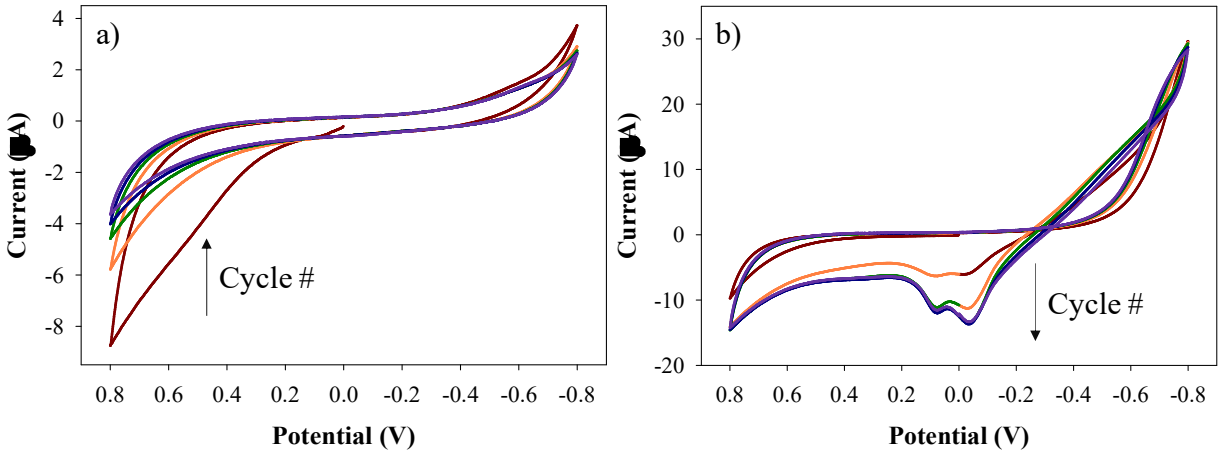

Figure A.5. Representative CV of (a) Ni foam and (b) UT coconut oil on Ni foam. Both were measured in a three-cell system with a Pt wire auxiliary electrode and a Ag/AgCl reference electrode in a 0.1 M Na_2SO_4 electrolyte and a scan rate of 100 mV/s.

capacitor behavior and areal capacitance can be determined. CVs of the bare Ni foam and the coconut oil dipped foam are shown in Fig. A.5(a) and (b), respectively. These data demonstrate that the underlying substrate and coconut oil do not have desirable capacitor behavior. By recording multiple cycles at a single scan rate, the cycling stability of these materials can be assessed.

Although these experiments typically measure the capacitance over thousands of cycles, these preliminary studies done with much smaller cycle numbers will be able to demonstrate the initial performance of these materials. Impedance spectroscopy will also be used to measure the resistance and capacitance properties and if there is ohmic contact between the VGN and the Ni substrate. The last property is especially important when considering device fabrication and a way to identify any disadvantages of this proposed method (i.e. use of the coconut oil or post-synthetic modification).

Achievement of milestone 3 will be demonstrated by assessing the capacitive properties of these materials. Through these electrochemical studies, it will be determined if the use the MO/VGN, post-synthetic plasma modification, or a combination of the two results in improved device performance when compared to the as-grown VGN. In addition, because of the variety of surface chemistries generated with this work (i.e. MO/VGN, CO_2, H_2O, and NH_3 plasma modification, and immediate versus delayed modification) a larger sampling of surface functional groups and resulting device performance can be cataloged. This results in the ability to correlate specific material properties to behavior. Ultimately, this proposed work moves toward better understanding of what material characteristics are desirable for a specific purpose and eventually a targeted approach for making these materials.

A.5 Potential Challenges

When growing the VGN and MO/VGN controlling the morphology (e.g. vertical orientation of nanosheets, even coverage of the substrate, uniform height VGN, etc.) is often challenging even when utilizing well studied methods such as a CH_4/Ar PE-CVD system. Therefore, similar issues are likely to occur when using a coconut oil precursor. Typically, additives such as H_2 are included in the hydrocarbon feedgas as atomic hydrogen is thought to remove amorphous carbon and promote crystallinity.[4, 19-20] Therefore, adding an additional source of hydrogen to the system in varying amounts can be used to further optimize coconut oil conversion. Other considerations for this work are focused around the post-synthetic modification. As stated previously, achieving the balance of modifying the materials without too much etching and structural damage is vital to proper modification. So, utilizing a pulsed plasma in the modification step may also be necessary. In addition, with the plasma modified VGN, relatively quick hydrophobic recovery is a concerning issue. Along with examining other plasma source gases that might result in more permanent modification, altering current modification procedures will also be necessary. From their papers, Sahoo *et al.* did not note if they flowed gas over their VGN after plasma modification,[9, 15] which is an important step as it controls what gases are present to quench any remaining active sites on the material and can heavily influence the surface chemistry of the material after plasma exposure. This phenomenon has been extensively studied in our lab through studies of N-doping of TiO_2 NP.[21] Incorporating this step in the modification process will be essential and easily added to the synthesis strategy. Finally, when performing electrochemical tests and in device fabrication, good ohmic contact between the VGN and substrate is critical. If this is not possible with the Ni foam substrates, VGN can be grown on a variety of alternate materials (Si/SiO, Ti, quartz, carbon paper, MgO, Au, Pt)[22-23] in

PE-CVD systems with little to no impact on the nucleation and growth of VGN, therefore, other substrates can easily be substituted.

REFERENCES

1. In 2018, the United States consumed more energy than ever before. https://www.eia.gov/todayinenergy/detail.php?id=39092 (accessed April 2020).
2. Wu, Y.; Qiao, P.; Chong, T.; Shen, Z., Carbon Nanowalls Grown by Microwave Plasma Enhanced Chemical Vapor Deposition. *Adv. Mater.* **2002,** *14* (1), 64-67.
3. Ghosh, S.; Polaki, S. R.; Sahoo, G.; Jin, E.-M.; Kamruddin, M.; Cho, J. S.; Jeong, S. M., Designing Metal Oxide-Vertical Graphene Nanosheets Structures for 2.6V Aqueous Asymmetric Electrochemical Capacitor. *J. Ind. Eng. Chem.* **2019,** *72*, 107-116.
4. Vesel, A.; Zaplotnik, R.; Primc, G.; Mozetič, M., Synthesis of Vertically Oriented Graphene Sheets or Carbon Nanowalls-Review and Challenges. *Materials* **2019,** *12* (18), 2968.
5. Stoica, S. D.; Vizireanu, S.; Acsente, T.; Dinescu, G., Hybrid Nanomaterial Architectures: Combining Layers of Carbon Nanowalls, Nanotubes, and Particles. *Plasma Chem. Plasma Process.* **2018,** *38* (4), 695-706.
6. Zhang, H.; Ren, W.; Guan, C.; Cheng, C., Pt Decorated 3D Vertical Graphene Nanosheet Arrays for Efficient Methanol Oxidation and Hydrogen Evolution Reactions. *J. Mater. Chem. A* **2017,** *5* (41), 22004-22011.
7. Sahoo, G.; Polaki, S. R.; Anees, P.; Ghosh, S.; Dhara, S.; Kamruddin, M., Insights into the Electrochemical Capacitor Performance of Transition Metal-Vertical Graphene Nanosheet Hybrid Electrodes. *Phys. Chem. Chem. Phys.* **2019,** *21* (45), 25196-25205.
8. Seo, D. H.; Han, Z. J.; Kumar, S.; Ostrikov, K., Structure-Controlled, Vertical Graphene-Based, Binder-Free Electrodes from Plasma-Reformed Butter Enhance Supercapacitor Performance. *Adv. Energy Mater.* **2013,** *3* (10), 1316-1323.
9. Sahoo, G.; Polaki, S. R.; Ghosh, S.; Krishna, N. G.; Kamruddin, M.; Ostrikov, K., Plasma-Tunable Oxygen Functionalization of Vertical Graphenes Enhance Electrochemical Capacitor Performance. *Energy Storage Mater.* **2018,** *14*, 297-305.
10. Bo, Z.; Mao, S.; Jun Han, Z.; Cen, K.; Chen, J.; Ostrikov, K., Emerging Energy and Environmental Applications of Vertically-Oriented Graphenes. *Chem. Soc. Rev.* **2015,** *44* (8), 2108-2121.
11. Ghosh, S.; Polaki, S. R.; Kumar, N.; Amirthapandian, S.; Kamruddin, M.; Ostrikov, K. K., Process-Specific Mechanisms of Vertically Oriented Graphene Growth in Plasmas. *Beilstein J. Nanotechnol.* **2017,** *8*, 1658-1670.
12. Santhosh, N. M.; Filipič, G.; Tatarova, E.; Baranov, O.; Kondo, H.; Sekine, M.; Hori, M.; Ostrikov, K. K.; Cvelbar, U., Oriented Carbon Nanostructures by Plasma Processing: Recent Advances and Future Challenges. *Micromachines* **2018,** *9* (11), 565.
13. Ouyang, B.; Zhang, Y.; Zhang, Z.; Fan, H. J.; Rawat, R. S., Green Synthesis of Vertical Graphene Nanosheets and Their Application in High-Performance Supercapacitors. *RSC Adv.* **2016,** *6* (28), 23968-23973.
14. Kumar, S.; Martin, P.; Bendavid, A.; Bell, J.; Ostrikov, K. K., Oriented Graphenes from Plasma-Reformed Coconut Oil for Supercapacitor Electrodes. *Nanomaterials* **2019,** *9* (12), 1679.
15. Sahoo, G.; Polaki, S. R.; Ghosh, S.; Krishna, N. G.; Kamruddin, M., Temporal-Stability of Plasma Functionalized Vertical Graphene Electrodes for Charge Storage. *J. Power Sources* **2018,** *401*, 37-48.
16. Bogart, K. H. A.; Dalleska, N. F.; Bogart, G. R.; Fisher, E. R., Plasma Enhanced Chemical Vapor Deposition of SiO_2 Using Novel Alkoxysilane Precursors. *J. Vac. Sci. Technol., A* **1995,** *13* (2), 476-480.

17. Stuckert, E. P.; Miller, C. J.; Fisher, E. R., Gas-phase Diagnostics During H_2 and H_2O Plasma Treatment of SnO_2 Nanomaterials: Implications for Surface Modification. *J. Vac. Sci. Technol., B* **2017,** *35* (2), 021802.
18. Mann, Z., M.S. recieved, Colorado State University, 2020.
19. Shiji, K.; Hiramatsu, M.; Enomoto, A.; Nakamura, M.; Amano, H.; Hori, M., Vertical Growth of Carbon Nanowalls Using RF Plasma-Enhanced Chemical Vapor Deposition. *Diamond Relat. Mater.* **2005,** *14* (3), 831-834.
20. Cui, L.; Chen, J.; Yang, B.; Sun, D.; Jiao, T., RF-PECVD Synthesis of Carbon Nanowalls and Their Field Emission Properties. *Appl. Surf. Sci.* **2015,** *357*, 1-7.
21. Pulsipher, D. J. V.; Martin, I. T.; Fisher, E. R., Controlled Nitrogen Doping and Film Colorimetrics in Porous TiO_2 Materials Using Plasma Processing. *ACS Appl. Mater. Interfaces* **2010,** *2* (6), 1743-1753.
22. Vizireanu, S.; Mitu, B.; Luculescu, C. R.; Nistor, L. C.; Dinescu, G., PECVD Synthesis of 2D Nanostructured Carbon Material. *Surf. Coat. Technol.* **2012,** *211*, 2-8.
23. Ghosh, S.; Ganesan, K.; Polaki, S. R.; Mathews, T.; Dhara, S.; Kamruddin, M.; Tyagi, A. K., Influence of Substrate on Nucleation and Growth of Vertical Graphene Nanosheets. *Appl. Surf. Sci.* **2015,** *349*, 576-581.

LIST OF ABBREVIATIONS

3D	3-dimmentional
Al_2O_3	aluminum oxide
Ar	argon
Au	gold
C	atomic carbon
C_2F_6	hexafluoroethane
C_2H_2	acetylene
C_3F_8	octafluoropropane
$C_6H_{12}N_4$	hexamethylene tetramine
Ce	cerium
CF_4	carbon tetrafluoride
CH_4	methane
Cl	atomic chlorine
CNT	carbon nanotubes
CO	carbon monoxide
CO_2	carbon dioxide
Cu	copper
CV	cyclic voltammogram
CVD	chemical vapor deposition
EDS	energy dispersive X-ray spectroscopy
EtOH	ethanol
Fe_2O_3	iron(III) oxide
FT-IR	Fourier-transform infrared spectroscopy
H_2	molecular hydrogen
$H_2O_{(v)}$	water vapor
hr	hour
Hres	High resolution
H_α	H-alpha
In_2O_3	indium(III) oxide
KBr	potassium bromide
LT-ICP	low-temperature inductively coupled plasma
LTP	low temperature plasma
MgO	magnesium oxide
min	minute
mm	millimeter
MnO_2	manganese(IV) oxide

MO	metal oxide
mTorr	millitorr
MΩ	megaohms
NH_3	ammonia
Ni	nickel
NO_2	nitrogen dioxide
NP	nanoparticle
NSF	National Science Foundation
NW	nanowire
O	atomic oxygen
O_2	molecular oxygen
O_3	ozone
O_{ads}	adsorbed oxygen
OES	optical emission spectroscopy
O_{lat}	lattice oxygen
P	power
p	pressure
Pd	palladium
PE-CVD	plasma-enhanced chemical vapor deposition
PGS	paper gas sensor
PPE	personal protective equipment
ppm	parts per million
Pt	platinum
RBS/ERDA	Rutherford backscattering with elastic recoil detection analysis
rf	radio frequency
R_X	resistance in gas "X"
s	seconds
SEM	scanning electron spectroscopy
Si	silicon
SiO	silicon monoxide
SMO	semiconducting metal oxides
Sn	atomic tin
$SnCl_2 \cdot 2\ H_2O$	tin(II) chloride dihydrate
SnO_2	tin oxide
TF	thin film
Ti	titanium
TiO_2	titanium dioxide
T_S	sensor temperature
UT	untreated
UV	ultraviolet

VGN	vertical graphene nanosheets
W	watt
WCA	water contact angle
WO_3	tungsten(VI) oxide
XPS	X-ray photoelectron spectroscopy
Zn	atomic Zn
$Zn(NO_3)_2 \cdot 6\ H_2O$	zinc nitrate hexahydrate
ZnO	zinc oxide
ZrO_2	zirconium oxide
µL	microliter
µm	micrometer